MODELING AND ANALYSIS OF THE DEGRADATION AND EROSION BEHAVIORS OF BIODEGRADABLE POLYMER IMPLANTS

A Thesis

by

MITCHELL FOSTER SHOCKLEY

Submitted to the Office of Graduate and Professional Studies of
Texas A&M University
in partial fulfillment of the requirements for the degree of

MASTER OF SCIENCE

Chair of Committee,	Anastasia Muliana
Committee Members,	Matt Pharr
	Terry Creasy
Head of Department,	Andreas Polycarpou

August 2019

Major Subject: Mechanical Engineering

ABSTRACT

Biodegradable polymers have been used for a variety of biomedical devices since the middle of the 20th century. The researched applications have ranged from dissolvable sutures to, in more recent years, implantable scaffolds. The projected benefits of these devices come from the need for implant removal after the tissue has healed. For example, cardiovascular stents often need to be removed due to the risk of thrombosis or arterial overgrowth from prolonged implantation.

In this study, the degradation and erosion behaviors of biodegradable polymeric implants is modeled and analyzed. For this work, initially dry Poly(lactic-co-glycolic acid) (PLGA) structures of varying complex geometries are examined. Constitutive equations and numerical algorithms are created to model the resulting time-dependent changes in local fluid concentrations, molecular weight loss, and monomer concentrations. This is done by taking advantage of MATLAB, a computational software. Complex geometries of multi-scale morphological features are discretized by combining several polygonal slices that capture key features of the body.

Local changes in fluid concentrations, molecular weights, and monomer concentrations are presented and used to predict the degradation and erosion behaviors of polymeric implants. As the erosion takes place, the mass, volume, and geometry of the body also change. For this study, the simplified geometry of a PLGA cylinder is used to calibrate the model parameters. A realistic stent design, perforated cylinder, and indented cube are among the complex geometries modeled with the calibrated parameters. These

results provide proof-of-concept for the constitutive equations and give insight into both the macroscopic and local behaviors of bulk and surface erosions. This study shows that geometry has a significant effect upon the modes of macroscopic erosion and yields further understanding how localized modes of erosion can differ from the overall body.

ACKNOWLEDGEMENTS

Thank you to Dr. Anastasia Muliana for allowing me the opportunity to pursue my goals, as well as her guidance and patience as I pursued this research. I would also like to thank my committee, supporting professors, classmates, colleagues, and friends for joining and helping me along the way.

I would especially like to thank Texas A&M's Supercomputing Facility for granting me access to the computing power that was very crucial in completing my research. Without their equipment and help desk my work would have turned out very differently. Additionally, I would like to thank the Department of Mechanical Engineering for allowing me access to the facilities and equipment that were much needed.

Finally, I would like to thank my mother and father for all of their support in pursuing my graduate education and for the free food when they came to visit.

CONTRIBUTORS AND FUNDING SOURCES

Contributors

This work was supervised by a thesis committee of Dr. Anastasia Muliana and Dr. Matt Pharr from the Department of Mechanical Engineering and Dr. Terry Creasy of the Department of Material Sciences and Engineering.

The data analyzed for Chapter 3 was first published in a paper by Friederike Von Burkersroda. All other work conducted for the thesis was completed by the student independently.

Funding Sources

There are no outside funding contributions to acknowledge related to the research and compilation of this document.

NOMENCLATURE

1D	One dimensional
2D	Two dimensional
3D	Three dimensional
FDA	Food and Drug Administration
HPRC	High Performance Research Computer
PCL	Poly(ε-caprolactone)
PDO	Poly(dioxanone)
PGA	Poly(glycolic acid)
PLA	Poly(lactic acid)
PLGA	Poly(lactic-co-glycolic acid)
PLLA	Poly(L-Lactide)
TAMU	Texas A&M University
TIPS	Thermally Induced Phase Separation

TABLE OF CONTENTS

Page

LIST OF FIGURES

Page

LIST OF TABLES

Page

CHAPTER I

INTRODUCTION

1.1. Implants as a General Technology

Over the past few centuries the progress of medicine and their respective technological innovations have led to an increase in the quality of healthcare. Equipment ranging from bandages to prosthetics has allowed the healthcare industry to improve their practice [1]. As of today, the United States Food and Drug Administration (FDA) has approved a wide array of implantation materials from tissue grafts, metals, plastics to ceramics. Of the existing technologies, the FDA has identified two primary types of implants: permanent and removable. This is to imply that removable requires another procedure for a proper extraction, and permanent eventually requires replacement, such as hip implants. The FDA has also cited that over time an implant could fail by modes of physical failure, such as a fracture, or by not working as intended [2].

Although there are some disagreements upon the definitive first use of man-made medical implants for the support or replacement of biological tissues in the human body (e.g. the use of magnesium wire as ligature in 1878 [3]), the general consensus for the beginning of modern implants dates back to the 1950s with the cardiac pacemaker [4]. Since then the implant industry has grown to encompass many different devices and applications for human use. In the last 60 years implants, both permanent and removable, have been made for knee and hip replacements, fracture joining, monitoring bodily processes, drug delivery systems, ventricular support, and nuerostimulation for pain

mitigation [4] to name a few. With the aging population of the United States [5] the use of implants for biological support may become more prevalent than previous decades.

1.2. Complications with Long Term Implantation

Approximately 965,000 coronary stents are implanted per year in the United States alone [6]. Bare-metal, or wire mesh, stents are among the most commonly used devices for coronary stent technology. However, while effective, the arterial sites around these implants often heal over the stent and once again block the artery. This is currently combated with stents coated in a polymer that releases a drug that actively promotes healing while simultaneously reducing the risk of future blockage. In newer studies it was found that long term stents are associated with an increased risk of thrombosis [6]– a blood clot formation within a blood vessel.

Orthopedic screws, pins, rods, and plates were ranked the 5th most common type of implanted medical devices as of 2011. There were an estimated 453,000 procedures for fracture repair preformed in 2007 alone with an approximate expenditure of $4.5 billion [7]. Unfavorable effects resulting from the commonly used metal alloy implants are primarily caused by the mechanisms of wear and corrosion. Free metallic ions and wear particles can have an adverse effect on the tissues surrounding the implants. Particulates due to wear, often deemed unavoidable, can induce inflammation and a foreign-body response that results in osteolysis which threatens the stability of the implant [8]. As particulate size decreases due to continued corrosion, ions can begin to enter the rest of

the body where they can be transported to cells, throughout the lymphatic system, and into the liver. This can result in cytotoxic or immunological effects [8].

1.3. Biodegradable Polymer Implants

Synthetic biodegradable polymers prepared from glycolic and lactic acids first made an appearance in the medical device industry after the approval of PGA sutures during the 1960s [9] and commercial availability since 1970 [10]. Since this time, a number of experimental trials have been performed on the biocompatibility of these devices with an overwhelming majority citing biodegradable polymers as adequately biocompatible [9]. Ideally, a biocompatible polymer should allow for cell growth [10], the polymer itself and its byproducts of degradation should not provoke inflammation or an immunotoxic response [9, 10], the polymer must be fully metabolized or absorbed by the body after completing its intended purpose [9, 10], able to be sterilized [9], able to be repeatedly produced into three dimensional structures [10], and the polymer should have tunable properties that match the appropriate tissue regrowth [10].

A number of biodegradable and biocompatible polymers are known [11], with many of these being synthetized and used for a variety of medicinal applications. As previously mentioned, poly(glycolic acid)- , or PGA, was among the first biocompatible polymers used for dissolving sutures. Since then, implants based on poly(lactic acid), the copolymer poly(lactic-co-glycolic acid), poly(ε- caprolactone), poly(L-lactide), and poly(dioxanone) have been created and are used within the medical industry. These polymers yield a wide range of mechanical, chemical, and physical properties as well as

varying degradation behavior. Polymers are appealing for implants since their properties can be tailored to a wide range of physiologically relevant applications and tuned for patient-specific implants. Because of this, polymers can be used for a variety of medicinal implants. For example, poly(ε- caprolactone), or PCL, has been used in both orthopedic implants and medicinal delivery [9, 11]. Studies on the inclusion of biphasic calcium phosphate (BCP) into poly(lactic-co-glycolic acid), or PLGA, structures by Ebrahimian-Hosseinabadi have shown the capabilities of a PLGA scaffolding to act as a stable structure for bone tissue engineering during cell regeneration [12, 13].

Biodegradable and biocompatible polymers provide several benefits over their metallic counterparts. While biodegradable metals, such as magnesium-, zinc-, and iron-based iron offer high strength and stiffness when compared to their polymer counterparts, biodegradable metals degrade at much faster rates than biodegradable polymers. This is not ideal in most applications, and as previously mentioned, the byproducts of metallic corrosion remains a large concern [8]. Biodegradable polymers offer the distinct advantage of being able to be engineered to slowly transfer loads to healing tissues whereas non-degradable metals can cause fracturing of bone or damage to tissue upon removal [9]. This is directly due to the inability of non-degradable metals to allow tissues to carry enough load during the healing process [9].

As of today, there are a variety of methods in which a biodegradable polymeric implant can be fabricated in order to achieve a desired percentage of porosity, overall geometry, and dispersed particulates for drug delivery or property tuning. A commonly used process to create a fibrous scaffold is electrospinning [14, 15]. Electrospinning is

often recognized for its ability to produce fine polymeric fibers for tissue engineering and regrowth applications because of its ability to create small pores within its structure [15]. Electrospinning produces the fibrous scaffolds by using electric fields on a polymer melt to control the deposition of very fine polymeric fibers onto a grounded collector [16]. Another commonly used method is thermally induced phase separation, or TIPS, is performed by dissolving polymer beads or powders into a solvent [12]. During this process the solution is typically stirred for a sufficiently long period of time in an attempt to make a relatively homogenous solution. This solution is then poured into a mold and placed in an oven, vacuum desiccator, or both simultaneously to remove the solvent and create a solid polymer body [12]. In more recent years, a variety of different 3D printing technologies have been applied in the fabrication of more complex geometries. While there are a variety of different methods for 3D printing, the basic approach is the same. Two-dimensional layers of material are deposited and bound according to a desired cross section repeatedly to create three-dimensional shapes. A popular method for medical applications is to deposit polymer powders into a fine layer and then precisely apply a binding solution in the area of the desired cross sectional shape [17]. This process allows for the dispersion of other particulates into the body and creation of reproducible/custom geometries. Another application of this technology is indirect 3D printing where a mold is made by a method of rapid prototyping and then a polymer is poured into the mold and solidified. This can be done by melting down polymer pellets in a vacuum oven either pre-pour or within the mold and subsequently vacuum cooling them to room temperature [18]. The previous method of TIPS can also be used.

1.4. Challenges Facing Biodegradable Polymeric Implants

Conforming to the Anatomy of Tissue

As of today, the persisting challenge facing biodegradable polymeric implants is their ability to conform to the anatomy of the target tissues. Ideally, this means that a polymeric implant must allow for cell adhesion and growth [10], the polymer and the byproducts from the process of erosion should not provoke inflammation of an immunotoxic response [9, 10], and must have tunable properties that match the appropriate tissue regrowth [10].

To achieve these end goals, the polymer implants must be able to be formed into complex geometries so that they can be properly mounted/applied in vivo or in vitro within the body. As previously mentioned, there exist production methods that enable the direct design and fabrication of these shapes; however, the lack of control over the porous microarchitectures of scaffold structures remains a large challenge facing end material characteristics. The existence of porosity is necessary as polymeric implants with higher porosity produce a large surface that is optimal for cell adhesion and growth [18, 19]. While the mean pore diameter and overall structure porosity can be tuned by means of altering production parameters and methods, it is *currently* impossible to control individual pore placement, diameter, and wall thickness between pores [18].

Attempts have been made to accomplish the engineering of multi-scale morphologies in order to tune degradation behavior and material characteristics. From current literature, there exists a tradeoff between shape complexity and multi-scale morphological tailoring. Current methods of combined, or hybrid, electrospinning have

been employed to obtain a random mixture of nano and micro fibers. While this can control the general ratio between nano and micro fibers and allow for 3D scaffolds above the millimeter scale (a limitation of scaffolds composed of purely polymer nano fibers) [14], the ability to create reproducible macro structures with controlled multi-scale morphologies remains to be a challenge in the field.

Fabrication Methods

There exists a variety of methods for the fabrication of polymeric implants. While each method has proven its ability to produce a scaffold structure, their respective shortcomings can substantially limit their ability to be utilized as a general implant. Current methods of nano fiber electrospinning are able to achieve the necessary high levels of porosity for cell adhesion; however, they are often limited in thickness [14]. The method of hybrid electrospinning previously mentioned combats this problem by introducing micro fibers that allow for thicker scaffolding structures [14]; however both methods of electrospinning have not demonstrated three-dimensional scaffold shapes outside of sheets and cylinders, thus limiting the ability for complex geometries [20]. A process variant of 3D printing can be used to create more complex geometries; however, as is typical with 3D printing, tensile strength can be lost due to weak interface bonding between layers. Additionally, the method of powder printing mentioned in the previous section has drawbacks with resolution limits based upon the size of the powder particulates, difficulty in removing unbound powders that remain after fabrication, and necessary use of organic solvent binders [17]. TIPS and gas-foaming share similar shortcomings. The inability to

precisely place individual pores can result in closed pores [20] and thin walled sections that result in stress concentrations that lead to a reduction in loading capabilities of the implant [18]. Gas-foaming also creates a mostly nonporous surface [20] that inhibits the polymeric implant's ability to promote cell adhesion [18].

Time-Dependent Mechanical and Physical Property Changes

As the polymeric implant is exposed to an aqueous environment, a hydrolytic process takes place, leading to polymer degradation. During the degradation process, which is to be discussed in a later section, initial mechanical and physical properties also change over time. More specifically, mechanical properties refers to metrics such as Young's Modulus, bulk modulus, yield stress, and tensile strength. Physical properties refer to molecular weight, fluid concentration, monomer concentration, crystallinity, porosity, and overall shape change. Macroscopic mechanical properties have been studied to understand the overall behavior of these scaffolding structures over the course of degradation [12, 13, 21, 22]; however, the understanding of local microscopic mechanical characteristics remains to be a challenge. The understanding of these mechanical metrics are crucial for the prediction and tuning of engineered polymeric implant degradation. Similarly, physical properties during degradation have been widely studied for a range of polymeric implant materials and compositions that span the analysis of the macroscopic change of molecular weight, fluid concentration, monomer concentration, crystallinity, and porosity [12, 13, 21-26]. As with mechanical properties, it is crucial to understand the measure of these local physical properties in order to predict polymeric implant

degradation. Degradation also induces heterogeneous changes in the mechanical and physical properties of a polymeric body that is initially homogenous with regards to its mechanical and physical properties. This heterogeneity will influence the overall structural integrity of the implant.

Load Transfer

Controllable load transfer of biodegradable polymeric implants remains to be a challenge within the field. Often these implants do not, or rather cannot yet, incorporate the load transfer behavior within their design because this attribute is widely unexplored. A tissue that is mechanically sensitive during the healing process would benefit from a gradual load transfer over time [27]. For example, bone affixed with a non-biodegradable stainless steel implant have an inclination to fracture when the implant is removed. This is directly due to the stainless steel implant carrying too much of the load during healing [9]. Therefore, having a polymer that can slowly degrade with engineered degradation-dependent mechanical characteristics and load transfer capabilities would be beneficial to the health of mechanically sensitive tissues such as bones and tendons [9, 27].

1.5. Hydrolytic Scission Process of Biodegradable Polymeric Implants

Degradation in a biodegradable polymeric implant is due to a hydrolysis process that coincides with physical processes. Degradation can be referred to as the molecular changes resulting from hydrolytic scission whereas erosion denotes changes due to mass loss of the degrading polymer chains [28]. Degradation due to hydrolysis in biodegradable

polymeric implants is necessary in order to have the body erode as it cleaves the bonds within chains and triggers erosion [26, 29]. Particularly, in a hydrolytic scission process water diffuses through the solid polymer matrix and break down macromolecular chains into oligomers and monomers [28, 30]. This reaction results in a reduction in molecular weight and changes in shape by means of erosion when the monomers and byproducts diffuse out of the polymer. As of today, the most commonly used metric for observing degradation and erosion behaviors is molecular weight [29] and mass loss.

Erosion of polymeric implants is typically defined by two different modes: surface and bulk [26]. Surface erosion occurs when a solid polymer loses mass from the surface of the structure and then erodes towards the center of the body. Conversely, bulk erosion occurs when a polymer loses mass such that outward diffusion of monomers occurs in a uniform manner. If water diffusions into the polymer faster than the macromolecular chains can degrade then the polymer will exhibit bulk erosion. If the degradation proceeds at a faster rate than water can diffuse into the body then the polymer will exhibit surface erosion [26]. In polymeric implants the balance of these two processes in combination with the geometric features of the scaffold determine the final shape and material characteristics of the implant.

Crystallinity of polymers may also have an impact upon the degradation behavior. In a situation where a polymer contains both crystalline and amorphous regions, it is possible that the hydrolytic scission process may begin to degrade the amorphous regions first. Although the crystalline region will also experience degradation and erosion, the rate at which occurs may be much slower. As a result, it is likely that smaller regions would

break off before being degraded. This could appear as “flaking”. This study does not account for this possibility directly. The values of coefficients and thresholds within the model are to be tuned across several samples and therefore will attempt to capture the average degradation behavior.

1.6. Research Objectives

There have been previous studies of the modeling and analysis of biodegradable polymeric bodies that focus mainly upon the effect of bulk erosion of these structures. Most of the studies focus on the drug delivery capabilities or the overall molecular weight and mass loss of implants although testing has shown that shape and boundary changes occur over the time of degradation. The objective of this research is to create a proof of concept tool that can predict the interaction of surrounding fluid on an initially dry PLGA structure and its impact on the changes of molecular weight, monomer concentrations, and shape change of the implant over time. By being able to predict this behavior it is possible, in part, to create a design in which one can anticipate the lifespan and changing characteristics of implants that would eventually degrade away. Poly(lactic-co-glycolic acid) PLGA was chosen for this study over other biodegradable polymers for its more readily controlled properties and degradation time. Additionally, by changing the ratio of lactic to glycolic acids, a control of crystalline structure can be achieved. This crystalline structure impacts local material properties and fluid uptake rates. The controllable degradation time is beneficial as it falls within the approximate time frame needed for

tissue to heal. To achieve the goals set out by this research, the following tasks are performed:

i. Develop coupled constitutive models to describe the time-dependent behavior of these implants based on current understanding and preliminary studies on the degradation behavior of biodegradable polymers.

ii. Develop a numerical algorithm assuming initially homogenous and isotropic material. The effect of swelling on degradation will be ignored. A von Neumann neighborhood method is used discretizing the polymeric body as well as the finite difference method for calculating time-dependent behavior of multi-dimensional morphological structures.

iii. Model varying bodies in SolidWorks and discretize them according to a Neumann neighborhood in MATLAB. The developed numerical algorithm in MATLAB is used to model the time-dependent degradation behavior of biodegradable polymers such as changes in the molecular weight, fluid concentrations, monomer concentrations, and shape. These outputs give a geometric representation of the degraded polymeric body.

CHAPTER II

MATERIALS AND METHODS

2.1. Constitutive Model for Degradation

Conceptually, the general description for the phenomena for the diffusion of fluid into and monomers out of the polymer scaffold is analogous to the heat equation, which attempts to describe how heat is distributed of a continuum, or the more general case of Fick's laws of diffusion. Fick's laws attempt to describe the behavior of molecular, and subsequently mass, transport through the mode of diffusion. Fick's laws are based upon the idea that over time molecules move from regions with high concentrations to those with low concentrations where the gradient of the concertation is the driving factor for the diffusion. This concept is graphically depicted in Figure 2.1. In Fick's law, the boundary of the body remains unchanged, which is applicable to the diffusion process that does not cause significant swelling or shape changes in the body and/or lead to chemical reactions.

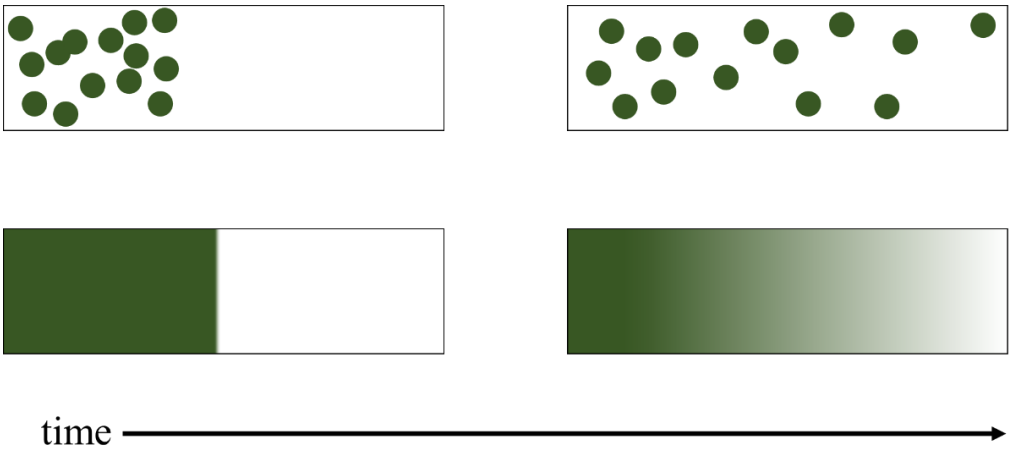

Figure 2.1: Graphical representation of molecular diffusion under Fick's laws of diffusion

Fick's first law describes the relationship between flux during diffusion and the gradient of the molecular concentrations. He denotes this in the following way:

$$\boldsymbol{J = -D\nabla\varphi} \tag{1}$$

where J is the flux from diffusion, D is the diffusivity coefficient, φ is the concentration, and $\boldsymbol{\nabla}$ is the gradient operator. Fick's second law models the change of concentration φ with respect to time. He denotes this in the following way:

$$\boldsymbol{\frac{\partial\varphi}{\partial t} = D\Delta\varphi} \tag{2}$$

where $\Delta = \nabla^2$ and is referred to as the Laplacian operator. Fick's second law is the primary concern of this study as we are attempting to see how diffusion of water and monomers changes their respective concentrations within the polymeric implants.

The time dependent model that includes the diffusion of fluid into the polymer, the fluid used to promote the hydrolytic scission reactions, and deformations due to possible swelling and mechanical loading is:

$$\boldsymbol{\frac{dC_f}{dt} = D_f\nabla^2 C_f - K_f C_f - \delta\nabla^2(tr\underline{E})} \tag{3}$$

where C_f, D_f, K_f are the fluid concentration, fluid diffusivity constant, and reaction rate constant respectively. The constant δ accounts for the effect of the volumetric changes due

to the diffusion process and $\underline{E}$ is the strain tensor. It is also possible for the diffusivity and reaction rate constants to vary spatially due to the existence of fluid concentration and/or as a result of the hydrolytic scission process. However, such situation is not being considered in this study, and the material parameters are assumed constant.

Hydrolytic scission occurs when fluid molecules attack the ester bonds within the polymer solid and consequently causes a reduction in molecular weight. Experimental studies have shown that mechanical loading also accelerates polymer degradation, and the existence of monomers and other byproducts of the scission can influence the hydrolytic process. Neglecting the presence of autocatalysis and effects of the crystalline phases, the model of the scission process is:

$$\frac{dN}{dt} = -\frac{f(\underline{E})C_f}{\tau_s}N; \qquad \text{Where} \quad 0 \leq \frac{N(t)}{N(0)} \leq 1 \tag{4}$$

where N is the molecular weight, τ_s is the characteristic time that drives the rate of molecular weight changes, and $f(\underline{E})$ is a strain function that accounts for accelerated scission due to mechanical strains. In this study, the accelerated scission due to deformations is ignored and $f(\underline{E})$ = 1. This study also assumed that the rate of molecular weight change and the rate of production of the monomers and byproducts are the same. For the rest of this manuscript the monomers and byproducts from the scission process will be referred to as monomers.

Monomers that are created from the scission process and diffused out of the body will be modeled as:

$$\frac{dC_m}{dt} = D_m \nabla^2 C_m - \frac{1}{N(0)} \frac{dN}{dt}; \quad C_m > C_{m,min} \tag{5}$$

where C_m is the concentration of the monomers, D_m is the diffusivity constant of the monomers leaving the solid, and C_{m_min} is the minimum monomer concentration in order to initiate the process of erosion.

2.2. Numerical Algorithm

Constitutive Equations

The coupled governing differential equations that describe the hydrolytic degradation will be computed with a finite difference approach. The generalized time and spatial derivatives under this approach are as follows:

$$\frac{df_i^m}{dt} \cong \frac{f_i^{m+1} - f_i^m}{\triangle t} \tag{6}$$

$$\frac{df_i^m}{dx} \cong \frac{f_{i+1}^m - f_{i-1}^m}{2\triangle x} \tag{7}$$

$$\frac{d^2 f_i^m}{dx^2} \cong \frac{f_{i+1}^m - 2f_i^m + f_{i-1}^m}{(\triangle x)^2} \tag{8}$$

where Δt is the defined time step and $\Delta\underline{x}$ is the defined step along each axis (distance between axial elements). Here $\Delta\underline{x} = (\Delta x, \Delta y, \Delta z)$. For a computationally stable analysis the following condition will be met:

$$\frac{\Delta t}{(\Delta \underline{x})^2} < 0.5 \tag{9}$$

For this model, the effect due to swelling is ignored. In a three-dimensional case, equation (3) will approximated as follows:

$$\frac{C_{f,ijk}^{m+1} - C_{f,ijk}^{m}}{\Delta t} = D_f \nabla^2 C_{f,ijk}^{m} - K_f C_{f,ijk}^{m} \tag{10}$$

Where $\nabla^2 C_{f,ijk}^{m} = \frac{C_{f,(i+1)jk}^{m} - 2C_{f,ijk}^{m} + C_{f,(i-1)jk}^{m}}{\Delta x^2} + \frac{C_{f,i1(j+1)k}^{m} - 2C_{f,ijk}^{m} + C_{f,i(j-1)k}^{m}}{\Delta y^2} \ldots$

$$\ldots + \frac{C_{f,ij(k+1)}^{m} - 2C_{f,ijk}^{m} + C_{f,ij(k-1)}^{m}}{\Delta z^2} \tag{11}$$

where the *ijk* subscripts and m superscript indicate the spatial and time indices respectively.

Equation (4) will be approximated as:

$$N_{ijk}^{m+1} = N_{ijk}^{m}\left(1 - \frac{C_{f,ijk}^{m} \Delta t}{\tau_s}\right) \tag{12}$$

Equation (5) will be approximated as:

$$\frac{C_{m,ijk}^{m+1}-C_{m,ijk}^{m}}{\Delta t} = D_m \nabla^2 C_{m,ijk}^{m} - \frac{1}{N(0)} \frac{N_{ijk}^{m+1}-N_{ijk}^{m}}{\Delta t} \quad \textbf{(13)}$$

Where $\nabla^2 C_{m,ijk}^{m} = \frac{C_{m,(i+1)jk}^{m}-2C_{m,ijk}^{m}+C_{m,(i-1)jk}^{m}}{\Delta x^2} + \frac{C_{m,i1(j+1)k}^{m}-2C_{m,ijk}^{m}+C_{m,i(j-1)k}^{m}}{\Delta y^2} \ldots$

$$\ldots + \frac{C_{m,ij(k+1)}^{m}-2C_{m,ijk}^{m}+C_{m,ij(k-1)}^{m}}{\Delta z^2} \quad \textbf{(14)}$$

Calculation of Constitutive Equations

All initial values of points within the modeled environment are assigned from the placement of the body within the discretized space. Their initial values based upon relative position in the modeled space are listed in Table 2.1. To prevent diffusion of both monomers and fluid out of a specific surface of the body, the .stl file is oriented against the edge of the discretized space. The process of model discretization will be discussed in more detail in the following section

Table 2.1: Initial values for discretized points based upon relative position

	Within Closed Body Surfaces	**Not Within Closed Body Surfaces**
C_f	0	1
$N(0)$	N_0	0
C_m	0	0

To calculate the values of fluid concentration, molecular weight, and monomer concentration, MATLAB's ability to quickly multiply large matrices is used. An important concept to determine the space-time matrix dimensions and keep track of position within these matrices is:

$$\underline{\boldsymbol{x}}_{\boldsymbol{s}} = \left(\frac{\boldsymbol{x}}{\boldsymbol{\Delta x}}, \frac{\boldsymbol{y}}{\boldsymbol{\Delta y}}, \frac{\boldsymbol{z}}{\boldsymbol{\Delta z}}\right) \tag{15}$$

$$\boldsymbol{t}_{\boldsymbol{s}} = \frac{\boldsymbol{t}}{\boldsymbol{\Delta t}} \tag{16}$$

where $\underline{x}_s$ is the number of steps along a specific spatial dimensions and t_s is the number of steps over time. The number of nodes in a single spatial dimension is equal to the number of steps plus one; therefore, it follows that the total number of nodes in all spatial dimensions is:

$$total\ spatial\ nodes = (\boldsymbol{x}_{\boldsymbol{s}} + \mathbf{1})(\boldsymbol{y}_{\boldsymbol{s}} + \mathbf{1})(\boldsymbol{z}_{\boldsymbol{s}} + \mathbf{1}) \tag{17}$$

The total number of spatial nodes is crucial as it determines the size of the square matrices used to calculate C_f and C_m values. Sparse matrices are used to efficiently store information without needlessly incorporating other unused cells that would only serve to increase the computation cost. Consequently, equations (10, 11), are rearranged as follows:

$$\begin{bmatrix} \boldsymbol{\alpha} & \boldsymbol{\beta} & \cdots & \boldsymbol{\gamma} & \dots & \boldsymbol{\zeta} & \dots \\ \boldsymbol{\beta} & \ddots & \ddots & & \ddots & & \boldsymbol{\zeta} \\ \vdots & \ddots & \ddots & \ddots & & \ddots & \vdots \\ \boldsymbol{\gamma} & & \ddots & \ddots & \ddots & & \boldsymbol{\gamma} \\ \vdots & \ddots & & \ddots & \ddots & \ddots & \vdots \\ \boldsymbol{\zeta} & & \ddots & & \ddots & \ddots & \boldsymbol{\beta} \\ \vdots & \boldsymbol{\zeta} & \dots & \boldsymbol{\gamma} & \dots & \boldsymbol{\beta} & \boldsymbol{\alpha} \end{bmatrix} \begin{bmatrix} \boldsymbol{C_{f,111}^{m}} \\ \boldsymbol{C_{f,211}^{m}} \\ \boldsymbol{C_{f,311}^{m}} \\ \\ \vdots \\ \\ \boldsymbol{C_{f,ijk}^{m}} \end{bmatrix} = \begin{bmatrix} \boldsymbol{C_{f,111}^{m+1}} \\ \boldsymbol{C_{f,211}^{m+1}} \\ \boldsymbol{C_{f,311}^{m+1}} \\ \\ \vdots \\ \\ \boldsymbol{C_{f,ijk}^{m+1}} \end{bmatrix} \tag{18}$$

$$\boldsymbol{\alpha} = -\mathbf{2}\boldsymbol{D_f}(\boldsymbol{\Delta t})\left[\frac{\mathbf{1}}{(\boldsymbol{\Delta x})^2} + \frac{\mathbf{1}}{(\boldsymbol{\Delta y})^2} + \frac{\mathbf{1}}{(\boldsymbol{\Delta z})^2}\right] - \boldsymbol{K_f}(\boldsymbol{\Delta t}) + \mathbf{1} \tag{19}$$

$$\boldsymbol{\beta} = \boldsymbol{D_f}(\boldsymbol{\Delta t})\left[\frac{\mathbf{1}}{(\boldsymbol{\Delta x})^2}\right] \tag{20}$$

$$\boldsymbol{\gamma} = \boldsymbol{D_f}(\boldsymbol{\Delta t})\left[\frac{\mathbf{1}}{(\boldsymbol{\Delta y})^2}\right] \tag{21}$$

$$\boldsymbol{\zeta} = \boldsymbol{D_f}(\boldsymbol{\Delta t})\left[\frac{\mathbf{1}}{(\boldsymbol{\Delta z})^2}\right] \tag{22}$$

where β, γ, and ζ were placed with an central offset of 1, $(x_s + 1)$, and $(x_s + 1)(y_s + 1)$ respectively. Similarly, equations (13, 14) are rearranged as follows:

$$\begin{bmatrix} \boldsymbol{\theta} & \boldsymbol{\kappa} & \cdots & \boldsymbol{\lambda} & \ldots & \boldsymbol{\mu} & \ldots \\ \boldsymbol{\kappa} & \ddots & \ddots & & \ddots & & \boldsymbol{\mu} \\ \vdots & \ddots & \ddots & \ddots & & \ddots & \vdots \\ \boldsymbol{\lambda} & & \ddots & \ddots & \ddots & & \boldsymbol{\lambda} \\ \vdots & \ddots & & \ddots & \ddots & \ddots & \vdots \\ \boldsymbol{\mu} & & \ddots & & \ddots & \ddots & \boldsymbol{\kappa} \\ \vdots & \boldsymbol{\mu} & \ldots & \boldsymbol{\lambda} & \ldots & \boldsymbol{\kappa} & \boldsymbol{\theta} \end{bmatrix} \begin{bmatrix} \boldsymbol{C_{m,111}^{m}} \\ \boldsymbol{C_{m,211}^{m}} \\ \boldsymbol{C_{m,311}^{m}} \\ \vdots \\ \boldsymbol{C_{m,121}^{m}} \\ \vdots \\ \boldsymbol{C_{m,ijk}^{m}} \end{bmatrix} + \frac{\mathbf{1}}{\boldsymbol{N(0)}} \begin{bmatrix} \boldsymbol{-N_{111}^{m+1} + N_{111}^{m}} \\ \boldsymbol{-N_{211}^{m+1} + N_{211}^{m}} \\ \boldsymbol{-N_{311}^{m+1} + N_{311}^{m}} \\ \vdots \\ \boldsymbol{-N_{121}^{m+1} + N_{121}^{m}} \\ \vdots \\ \boldsymbol{-N_{ijk}^{m+1} + N_{ijk}^{m}} \end{bmatrix} = \begin{bmatrix} \boldsymbol{C_{m,111}^{m+1}} \\ \boldsymbol{C_{m,211}^{m+1}} \\ \boldsymbol{C_{m,311}^{m+1}} \\ \vdots \\ \boldsymbol{C_{m,121}^{m+1}} \\ \vdots \\ \boldsymbol{C_{m,ijk}^{m+1}} \end{bmatrix} \tag{23}$$

$$\boldsymbol{\theta = -2D_m(\Delta t)\left[\frac{1}{(\Delta x)^2} + \frac{1}{(\Delta y)^2} + \frac{1}{(\Delta z)^2}\right] + 1} \tag{24}$$

$$\boldsymbol{\kappa = D_m(\Delta t)\left[\frac{1}{(\Delta x)^2}\right]} \tag{25}$$

$$\boldsymbol{\lambda = D_m(\Delta t)\left[\frac{1}{(\Delta y)^2}\right]} \tag{26}$$

$$\boldsymbol{\mu = D_m(\Delta t)\left[\frac{1}{(\Delta z)^2}\right]} \tag{27}$$

where κ, λ, and μ were placed with an central offset of 1, $(x_s + 1)$, and $(x_s + 1)(y_s + 1)$ respectively. Lastly, the indicial calculation for molecular weight from equation (12) is rearranged as follows:

$$\begin{bmatrix} \boldsymbol{N_{111}^{m}} & \boldsymbol{N_{211}^{m}} & \boldsymbol{N_{311}^{m}} & \ldots & \boldsymbol{N_{121}^{m}} & \ldots & \boldsymbol{N_{ijk}^{m}} \end{bmatrix} \left(\underline{\mathbf{I}} - \frac{\boldsymbol{\Delta t}}{\boldsymbol{\tau_s}} \begin{bmatrix} \boldsymbol{C_{f,111}^{m}} \\ \boldsymbol{C_{f,211}^{m}} \\ \boldsymbol{C_{f,311}^{m}} \\ \vdots \\ \boldsymbol{C_{f,ijk}^{m}} \end{bmatrix}\right) \tag{28}$$

Model Discretization

All dimensional models are discretized according to a von Neumann neighborhood. This method is highly beneficial because it permits an entire environment to be discretized and then a group of points selected to be considered part of the body under analysis. The placement of the body within this environment determines the boundary conditions. Placing a face against a wall will cause that side to have no diffusion in or out (zero flux boundary condition). A 2D representation of the von Neumann neighborhood is depicted in Figure 2.2.

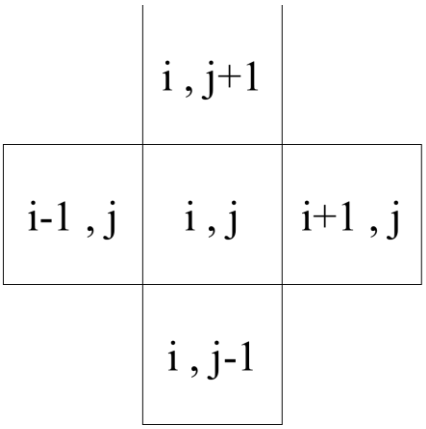

Figure 2.2: Depiction of von Neumann neighborhood

It follows that a three dimensional extrapolation would include the *k* component and subsequently the origin *i,j,k* would be surrounded by a total of six discrete regions.

The process created for discretizing the body can be simplified into 4 major sub processes:

1. Prepare – General parameters of regional dimensions and dimensional step size are defined. The geometric shape from the 3D file are loaded and adjusted to fit within the defined region
2. Build – The geometric shape from the 3D file are plotted to create a visible check of correct placement. The entire region is discretized.
3. Define – The region is sliced along the (001) plane at intervals of Δz. Locations that intersect the walls of the body on the slice plane are collected as points and assigned to a respective z value. These intersection points are used to define polygons at given z heights. Discretized points from the build process along the slice plane are compared with the aforementioned polygons. Points within and on the edge of the polygon are cataloged for future use. These discrete points comprise a 2D representation of the 3D body on the given slice plane.
4. Output – Points not within and on the edge of the polygon are discarded. All remaining points are output and plotted for a final visible check.

These 4 major sub processes are further broken down in Figure 2.3. Blocks within the MATLAB script are condensed and simplified into 1-3 boxes in the figure to create a more concise graphic. A more detailed description of each one of these major sub processes will be covered in the following sub sections.

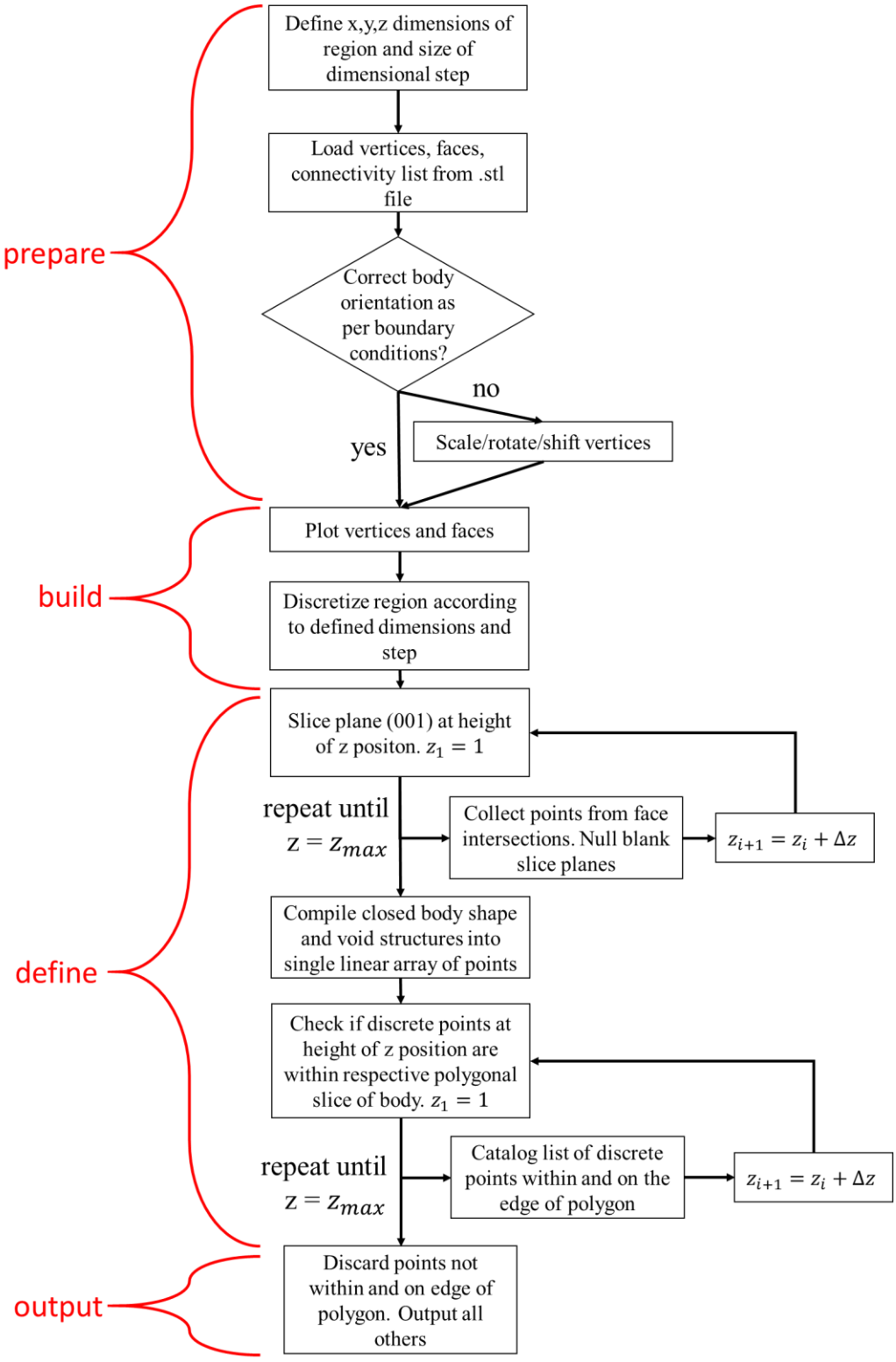

Figure 2.3: General logic and overall organization of model discretization

Prepare

This first sub process is straight forward in its approach. It accepts and stores user defined dimensions and $\Delta\underline{x}$ for the working volume. From equation (17) this gives the maximum number of nodes. This sub process also loads vertices, connectivity list between vertices, and face data from a generated .stl 3D file. At this point, if the 3D object needs to be rotated or scaled to match the desired sizing and relative position, a deformation matrix is used to accomplish this.

Build

The build sub process is where the initial physical relationship between the 3D file and discrete points is established. The deformed vertices of the loaded 3D file are plotted and assigned their respective connecting faces. This is shown in Figure 2.4. Secondly, the discrete points are created and given their location attributes by the following algorithm:

$$\boldsymbol{X_{i+(x_s+1)(j-1)+(y_s+1)(x_s+1)(k-1)} = i(\Delta x) + 1 - \Delta x}\ ;\ldots$$

$$\ldots\boldsymbol{Y_{i+(x_s+1)(j-1)+(y_s+1)(x_s+1)(k-1)} = j(\Delta y) + 1 - \Delta y}\ ;\ldots$$

$$\ldots\boldsymbol{Z_{i+(x_s+1)(j-1)+(y_s+1)(x_s+1)(k-1)} = k(\Delta z) + 1 - \Delta z}\ ;\ \ldots$$

$$\ldots \text{ Where } \boldsymbol{i = 1 \ldots (x_s + 1);\ j = 1 \ldots (y_s + 1);\ k = 1 \ldots (z_s + 1)} \qquad \textbf{(29)}$$

This step is crucially important as it is the predecessor for the column matrix format given in the Calculation of Constitutive Equations section. It prepares the form 111, 211, 311 …121… and so on. A graphical representation of this is shown in Figure 2.5.

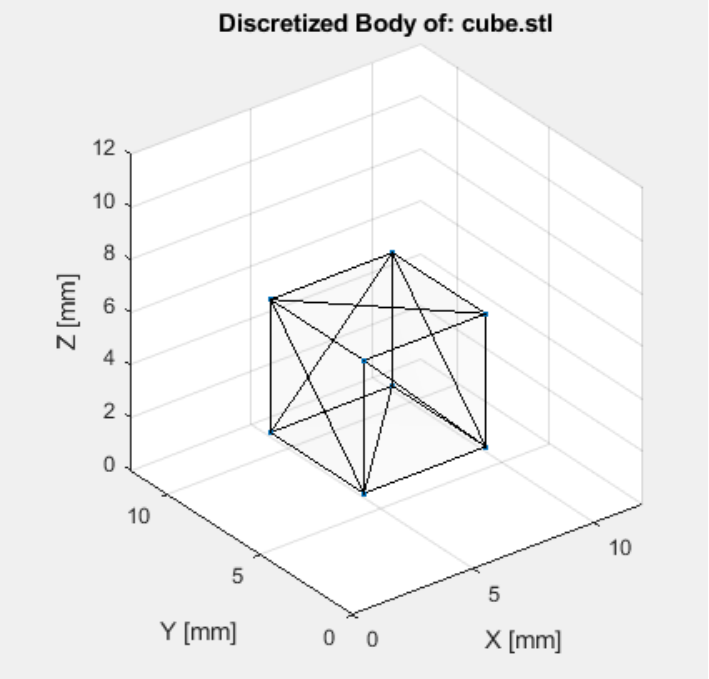

Figure 2.4: Plotting vertices and faces during discretization

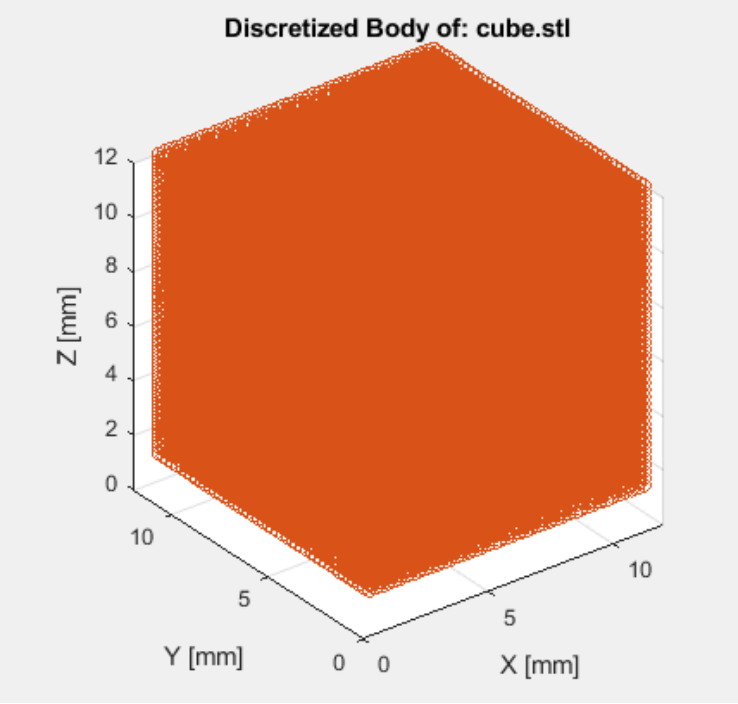

Figure 2.5: Graphical representation of discrete points created

Define

The define stage is the most computationally taxing; therefore, a large effort was made to improve the overall efficiency to prevent unnecessarily long calculation times for finer resolutions. Since the defined dimensions demand that the discretized environment form a cube, a cut along the (001) plane was deemed the most appropriate to reflect XY plane slices. The z distance between each cutting plane corresponds to the step in the z direction. The first cut is placed at the minimum z value and repeated until the maximum z value is reached. On each repetition of this process cross sectional polygons are found by sending out lines from a series of points and determining where they intersect with a face defined by the 3D file. The intersections are assigned a coordinate value and saved. This specific process uses a community generated function called xsecmesh. Xsecmesh is particularly beneficial because as opposed to other common methods of edge-plane intersection, xsecmesh can account and correct for repeat vertices and edges – a common problem in the creation of .stl files [31]. The intersection points and polygons are compiled with other associated points and polygons that correspond to voids and body volume at the same z height. This larger set of linear arrays and points are fed into MATLAB's internal inpolygon function which checks to see if points are within or on the edge of a polygon. The process is looped in the same method as the slice planes were. The first polygon test occurs at the minimum z value and is repeated until the maximum z value is reached. Discretized points and their relative positions to the cross sectional polygon are cataloged and stored for the final step.

Output

This final step takes the least amount of computational time. Particular discrete points not within or on the face of the 3D body are discarded. Their position is still earmarked but are given no significant location value. This is done to minimize the save file size of discretized bodies. Lastly, the points are plotted against the 3D file presented in the build sub process. This is shown in Figure 2.6. A visual inspection is performed to ensure all required features were captured by the stated $\Delta\underline{x}$.

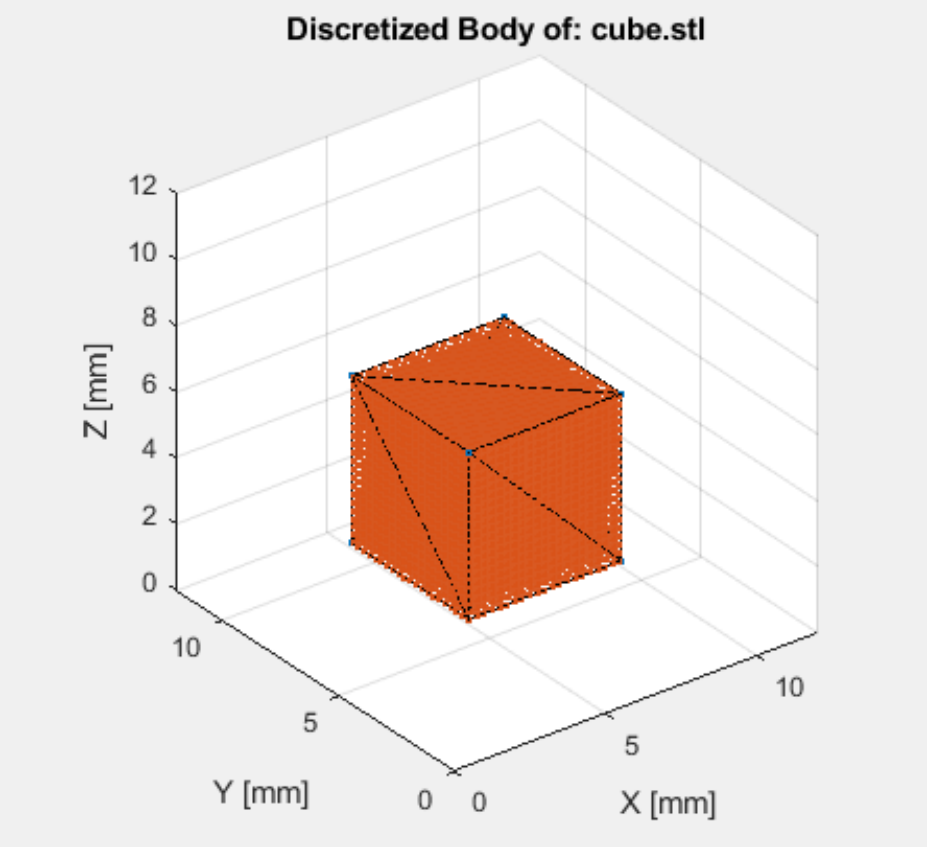

Figure 2.6: Discretized points of geometry

CHAPTER III

RESULTS

3.1. Convergence Study

A discretization step size convergence test was performed in order to determine a suitable number of nodes and step size that would yield reasonably consistent and accurate results for polymeric implants. During this study, the condition for computational stability presented in equation 9 was met at all times. To study convergence, a cylinder of 12.5mm diameter and 1.5mm thickness, based upon the PLGA matrix described in a study by Burkersroda [26], was placed into a 15x15x3mm (XYZ) region and discretized according to varying Δz. These steps sizes caused nodal distances to range from very coarse to very fine. The values of Δx and Δy were kept fixed at 100μm as most of the diffusion occurred through the thickness of the cylinder. Additionally, preliminary runs, where all step sizes were kept equal, exhibited little to no drastic in degradation or erosion behavior and 100μm yielded favorable stability and computational savings. The values used for degradation and diffusion coefficients during the convergence study were based on the magnitude of values found in preliminary modeling of molecular weight erosion for the same cylindrical body. The preliminary coefficients and thresholds were calibrated by first starting with a large dimensional step and time step. The order of magnitude that these coefficients were tuned around were, in part, retrieved from outside studies of degradation behavior. The specific values will be discussed in greater detail upon the statement of further calibrated coefficients and thresholds. These preliminary values can be seen in

Table 3.1. All tests were performed over 3 days with 3 sets of time steps of 15 minutes, 30 minutes, and 60 minutes respectively. The results of this study, which shows the average molecular weight of the body after 3 days, are shown in Figure 3.1 and Table 3.2.

Table 3.1: Convergence study degradation and diffusion values

Coefficient/Threshold	Value
D_f	$684\ \mu m^2 hr^{-1}$
K_f	$1.8 * 10^{-3} hr^{-1}$
τ_s	$150\ hr$
N_0	$8000\ Da$
D_m	$36\ \mu m^2 hr^{-1}$
$diffusion\ threshold$	$0.02 \leq C_{m,i}$
$erosion\ threshold$	$0.8\ \geq N_i N_0^{-1}$

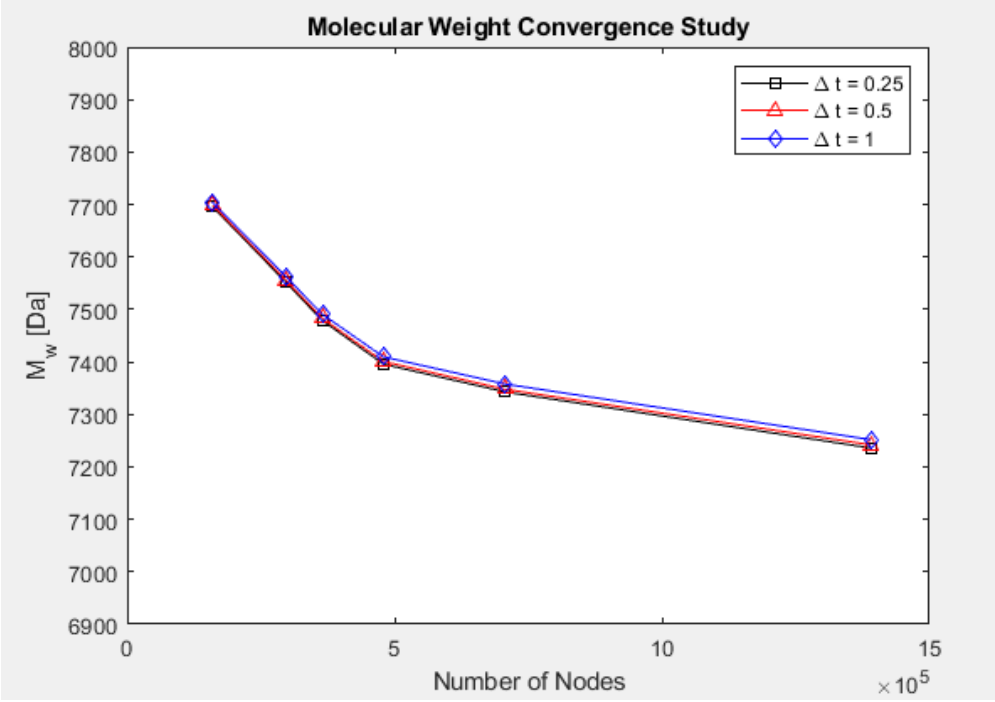

Figure 3.1: Convergence plot based upon Burkersroda study

Table 3.2: Number of elements and the respective average molecular weight at varying time steps

# of Nodes	$M_{w,avg}\ \Delta t = 0.25hr$	$M_{w,avg}\ \Delta t = 0.5hr$	$M_{w,avg}\ \Delta t = 1\text{hr}$
159607	7696	7699	7704
296413	7552	7556	7563
364816	7479	7483	7491
478821	7396	7401	7410
706831	7343	7348	7358
1390861	7236	7242	7252

Based on the convergence study, it was determined that a Δt and Δz of 1 hour and 100μm respectively would act acceptably for discretization. A Δz of 100μm corresponds to 706831 elements for a modeling environment of 15x15x3mm (XYZ). Compared to the finest mesh and time steps, these modeling variables presented a 1.658% deviance. A depiction of this body with the previously mentioned discretization variables is presented in Figures 3.2 and 3.3.

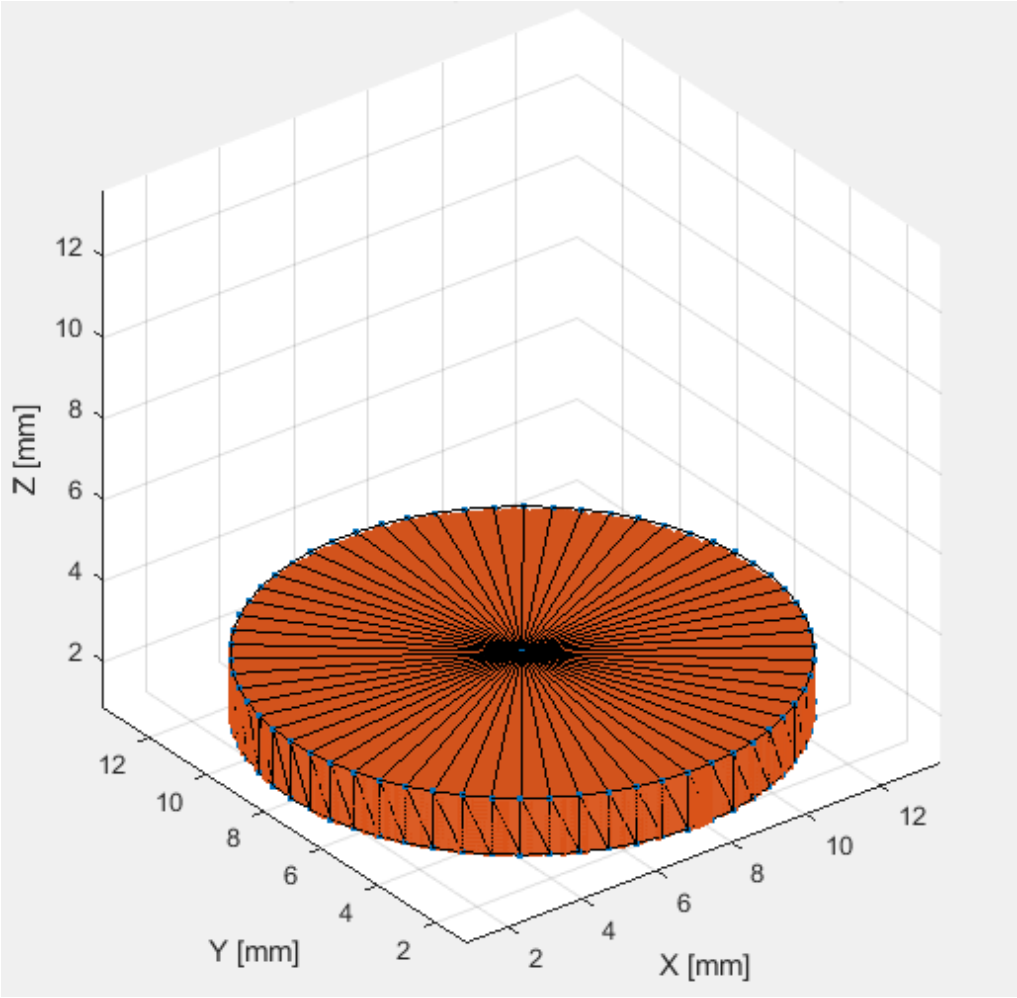

Figure 3.2: Discretized cylinder. $\Delta x=\Delta y=\Delta z=100\mu m$

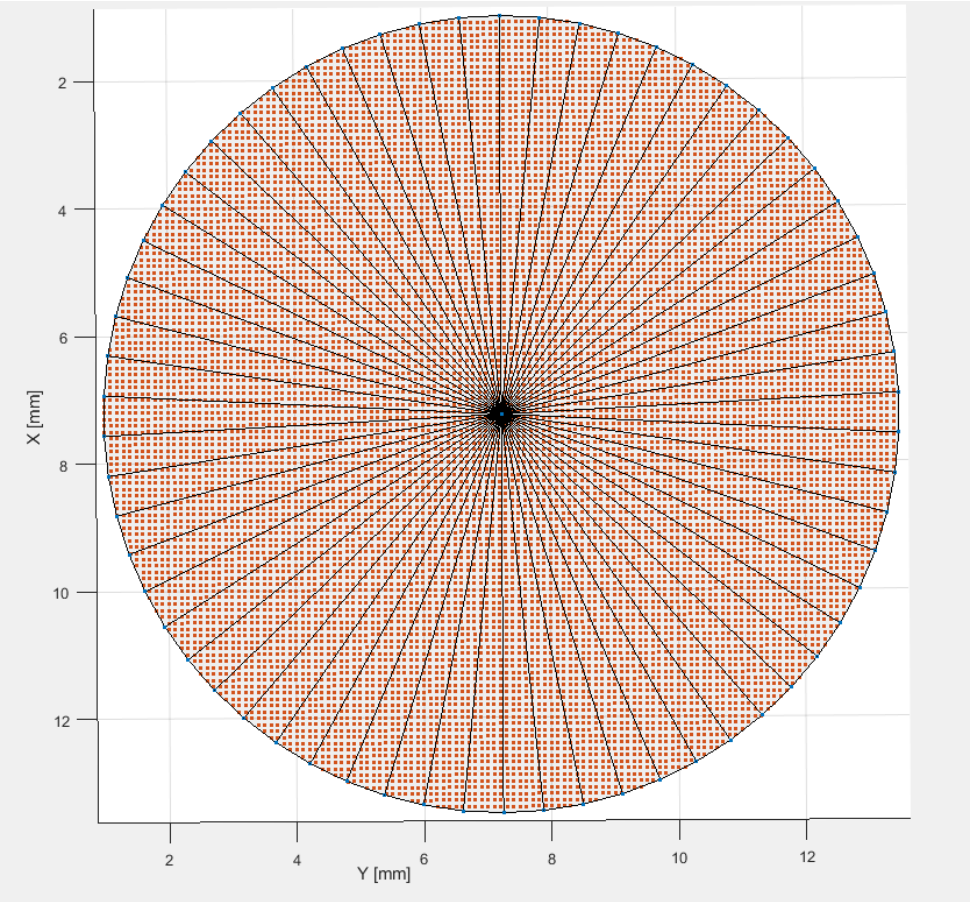

Figure 3.3: Top down view of discretized cylinder. $\Delta x=\Delta y=\Delta z=100\mu m$

3.2. Experimental Modeling

Modeling

Following the study of convergence, the same cylindrical body was used for a comparison to the experimental results presented by Burkersroda in a paper that assessed why degradable polymers, specifically PLA and PLGA, undergo surface or bulk erosion [26]. The process for calibrating the model began with first using the preliminary values for degradation previously presented in Table 3.1. Understanding the rather consistent

direction of deviance between coarser and finer finite difference nodes, the model was first tuned following a uniform Δx,y,z of 250μm. Due to the significant computation cost savings, this allowed for a great speed increase while iterating the MATLAB script during the matching of the general behavior of the data sets. Once a sufficient fit, with a consideration of the deviance due to coarser finite difference nodes, was found, these values were input into the same MATLAB script on the TAMU HPRC. Two biodegradable polymers that differ in their initial molecular weights, namely $PLA_{25}GA_{50}$8h and $PLA_{25}GA_{50}$14h, were studied. $PLA_{25}GA_{50}$ is comprised of 50% D,L-lactic acid and 50% glycolic acid. The numbers following, 8 and 14, represent the expected initial molecular weight in thousands. Both samples were created by polymer powder compression [26]. For $PLA_{25}GA_{50}$8h, the coefficients and variables used to fit the model are shown in Table 3.3 and the degradation response (reduction in the overall molecular weight) from the model is shown in Figure 3.4. The coefficients are fit in an iterative fashion. All initial values are either approximated from the data or set based on coefficients found in outside studies. Qualitative relationships between variables were determined by first adjusting each coefficient by ~$\pm$10% and observing how these impacted the overall curve. Values were continually adjusted until a curve that captured the general behavior of the data (within experimental error) was found. The calibrated coefficients are within an order of magnitude of those found in prior outside studies. In three related studies D_f is on the order of magnitude 10^{-8} cm^2s^{-1} [26, 30, 32], or 10^{-6} mm^2s^{-1} or 10^4 μm^2hr^{-1}. The preliminary value was based around this magnitude and the calibrated result is found to be within that range as well. The approximate value of D_m in experimental studies is stated

to be 10^{-10} cm^2s^{-1} [32], or 10^{-8} mm^2s^{-1} or 36 μm^2hr^{-1}, in other outside studies. N_0 is based upon the data set provided in the Burkersroda study [26]. The magnitude of K_f is a lumped value of fluid consumption in the hydrolytic reactions and could not be directly found in experimental studies and therefore was approximated to be on the order of magnitude $10^{-6}s^{-1}$- similar to D_f. The value for τ_s was initially approximated according to and then calibrated based upon where the eroding molecular weight of the Burkersroda data began to change curvature in addition to where the study began to qualitatively see geometric instability around 5 days [26]. Values for diffusion and erosion thresholds were calibrated in the model and loosely based upon τ_s.

Table 3.3: $PLA_{25}GA_{50}$8h Model Coefficient and Threshold Variables

Coefficient/Threshold	Value
D_f	$1728\ \mu m^2 hr^{-1}$
K_f	$1.8 * 10^{-3} hr^{-1}$
τ_s	$100\ hr$
N_0	$10800\ Da$
D_m	$36\ \mu m^2 hr^{-1}$
$diffusion\ threshold$	$0.02 \leq C_{m,i}$
$erosion\ threshold$	$0.45\ \geq N_i N_0^{-1}$

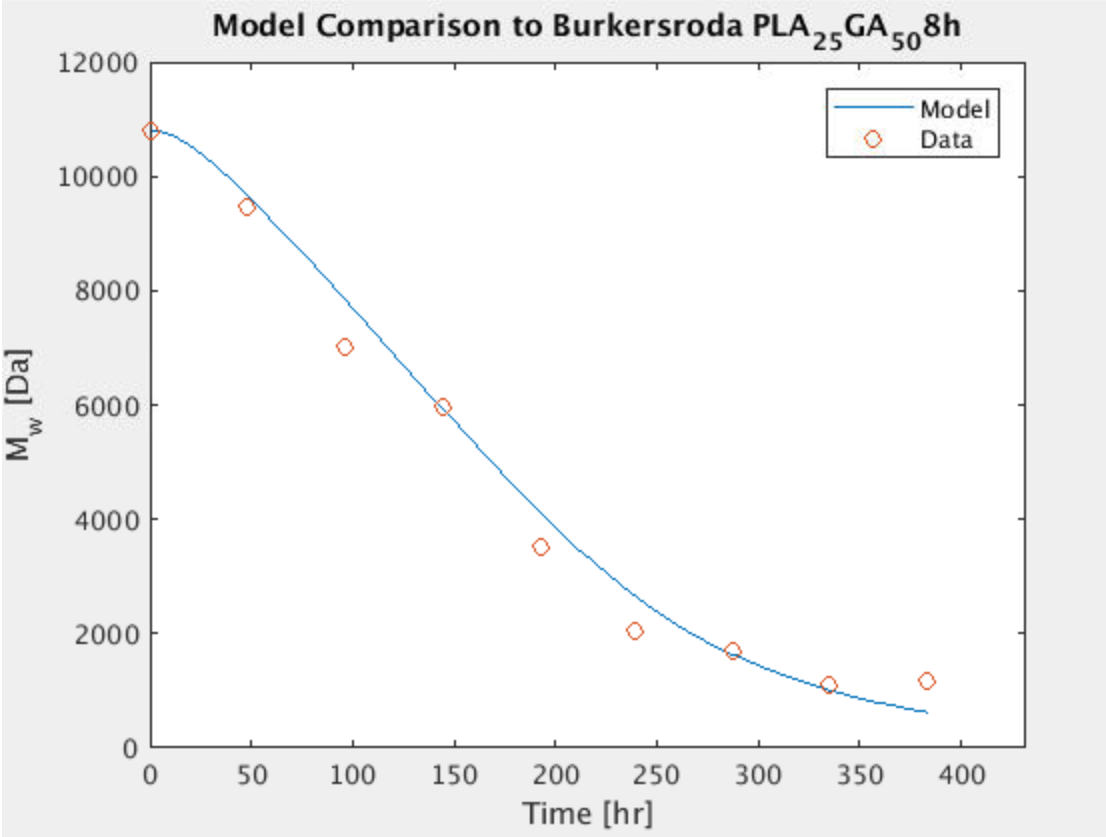

Figure 3.4: Fit model of $PLA_{25}GA_{50}8h$ comparison to Burkersroda data

The molecular weight values used within the plot in Figure 3.4 are calculated by averaging all points considered part of the original body. A side, cross section, and isometric views of molecular weight distribution is shown in Figures 3.5, 3.6, and 3.7-9 respectively . To give an indication what the shape during degradation may look like, all local values for the ratio between current molecular weight and initial molecular weight that fall below 25% (more than 75% of the local polymers have been broken into monomers) are excluded from the graphical portrayal. This value can be easily controlled and further calibrated given an expiremental study over the shape change, but for this

study 25% is used because it allows regions of the body to become saturated but not entirely erode immediately. As expected, the model predicts that a large loss of mass occurs through thickness as the area corresponding to the top and bottom of the body are significantly larger than that of the area due to the edges of the cylinder (approximately 4.17:1). However, erosion from the edges is not negligible, which not only alters the dimensions, but also the shape of the body.

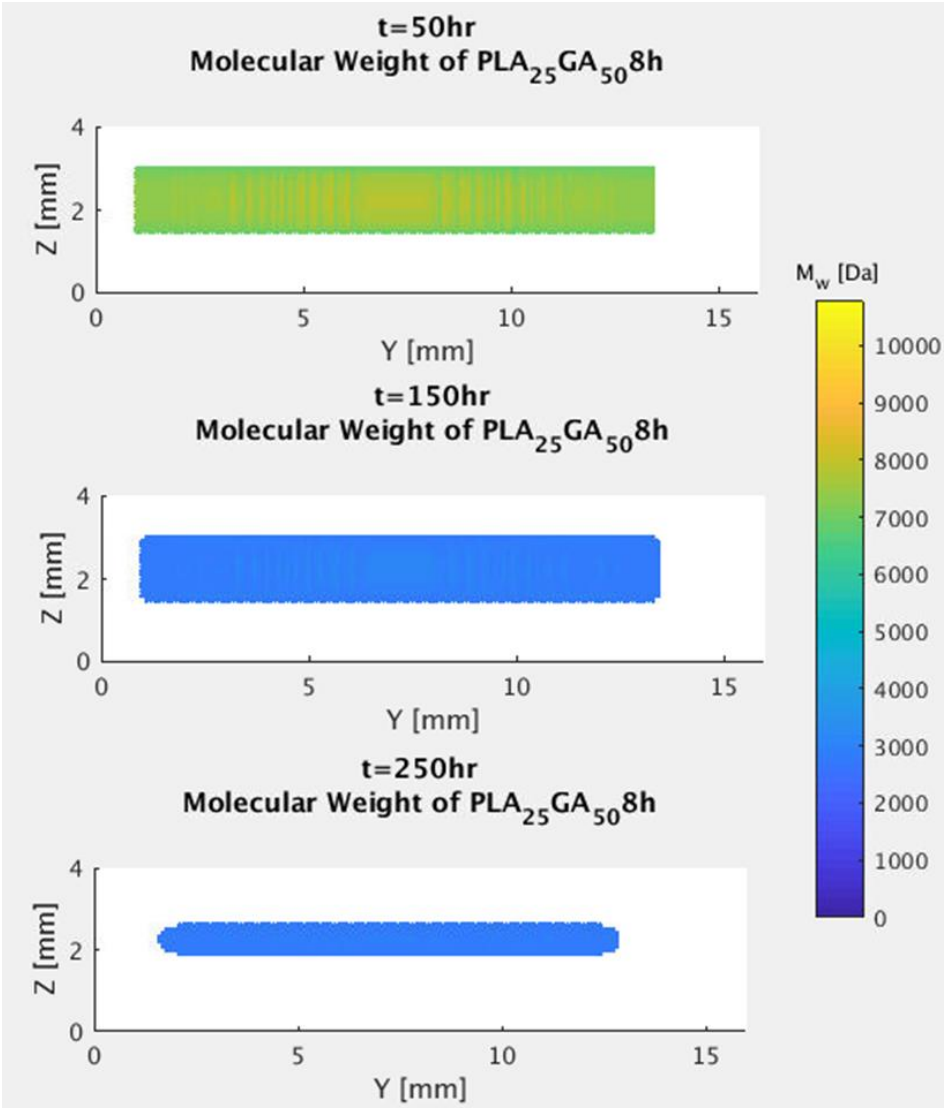

Figure 3.5: Side view of $PLA_{25}GA_{50}8h$ molecular weight distribution and erosion. $N > 0.25\ N_0$

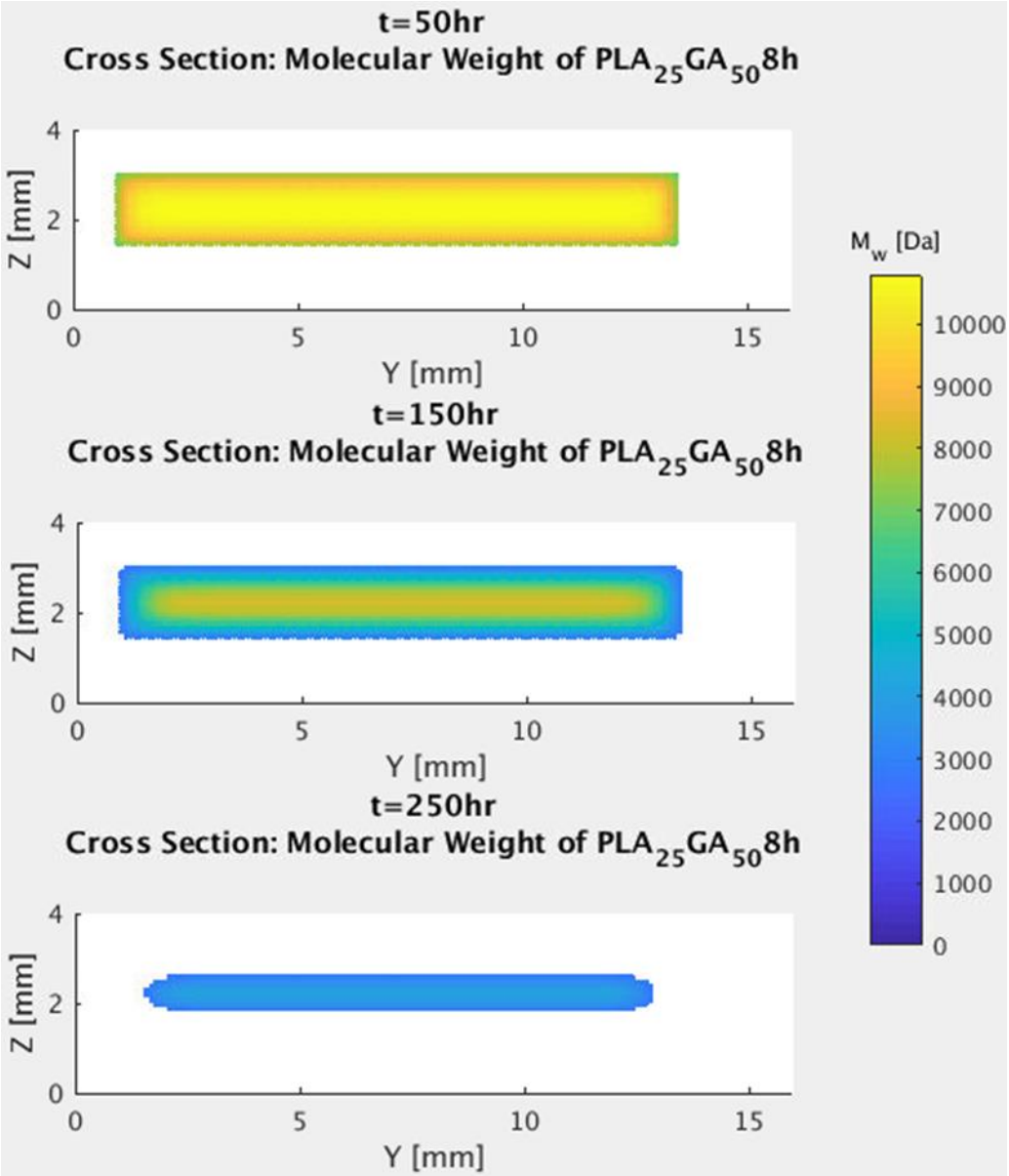

Figure 3.6: Cross section view of $PLA_{25}GA_{50}8h$ M_w distribution and erosion. $N > 0.25\ N_0$

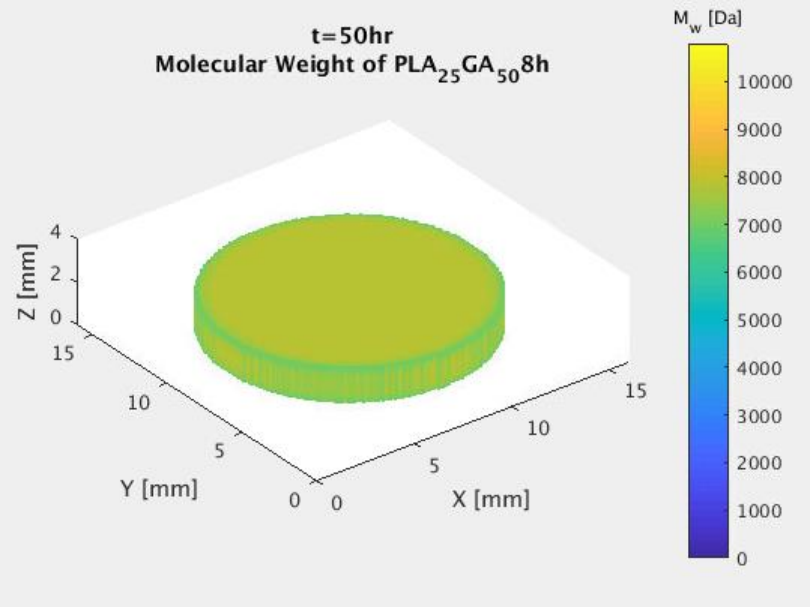

Figure 3.7: Isometric view of $PLA_{25}GA_{50}8h$ M_w distribution and erosion at 50hr. N > 0.25

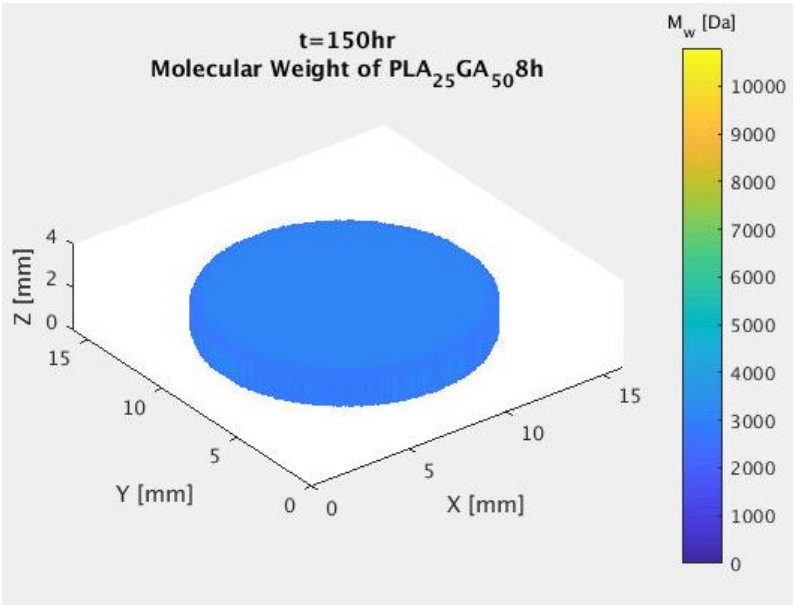

Figure 3.8: Isometric view of $PLA_{25}GA_{50}8h$ M_w distribution and erosion at 150hr. N > 0.25

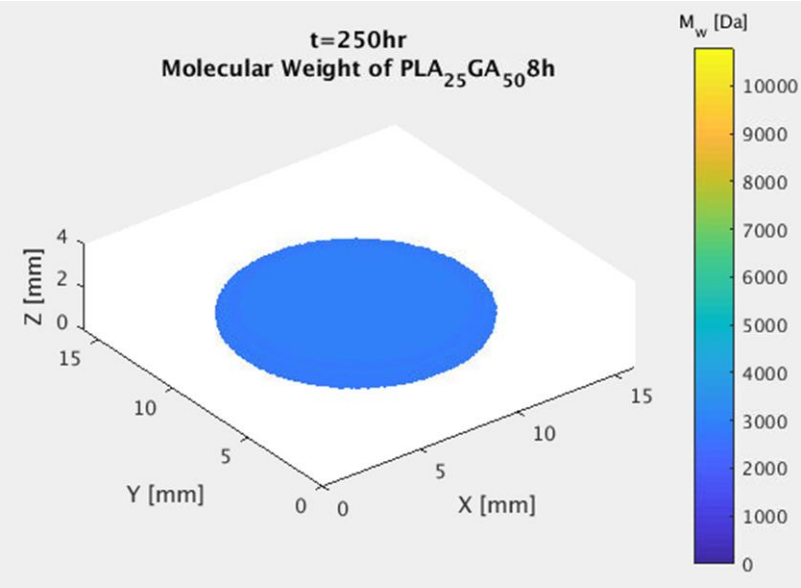

Figure 3.9: Isometric view of $PLA_{25}GA_{50}8h$ M_w distribution and erosion at 250hr. N > 0.25

Figures 3.10-12 show a cross section view of molecular weight, fluid concentration, and monomer concentration distributions, respectively, plotted on the original body. For this simulation all values of monomer concentration outside of the original body are fixed at 0. This was done to simulate a sufficiently large environment in which the polymer cylinder was placed or an experiment where the erosion media is frequently replaced. Given the relatively small size of the modeling region, the 0 monomer concentration assumption seemed to most accurately reflect the experimental process followed in the study [26]. It is possible to remove this limitation to simulate the monomer concentration distribution for a polymeric body submerged within a relatively enclosed area. Some important features to note of the aforementioned Figures 3.10-13 are:

- Molecular weight distribution first experiences comparatively larger losses closer to the original surface in the early portion of the simulation which indicates that

the body demonstrates erosion behavior more similar to surface erosion. However, after a sufficient period of time, e.g. t=350hr, in which the fluid can saturate the polymer body as a whole, the cylinder exhibits erosion behavior similar to bulk erosion as seen by the relatively homogeneous distribution of molecular weight and monomer concentration.

- Fluid concentration does not scale linearly with time. Instead, as the simulated cylinder begins to erode, the fluid concentration reaches an asymptotic value of 1. The curve is shown in Figure 3.13. It must be noted that this plot displays the effects of erosion on fluid concentration. Up until approximately 120 hours, the C_f curve exhibits what would be expected of a non-eroding body where fluid is gradually diffused into the body until full saturation is complete. The effect of erosion causes an increase in C_f. This is due to the eroding surfaces being in direct contact with either a saturated portion of the polymer or the surrounding fluid.
- Given the current low rate at which monomers diffuse out of the region representing the initial geometry, a large portion of the byproducts from hydrolytic scission remain stationary. This cannot be confirmed with the experiment as the cylinders were removed between measurements and the erosion media was frequently changed throughout the study [26].

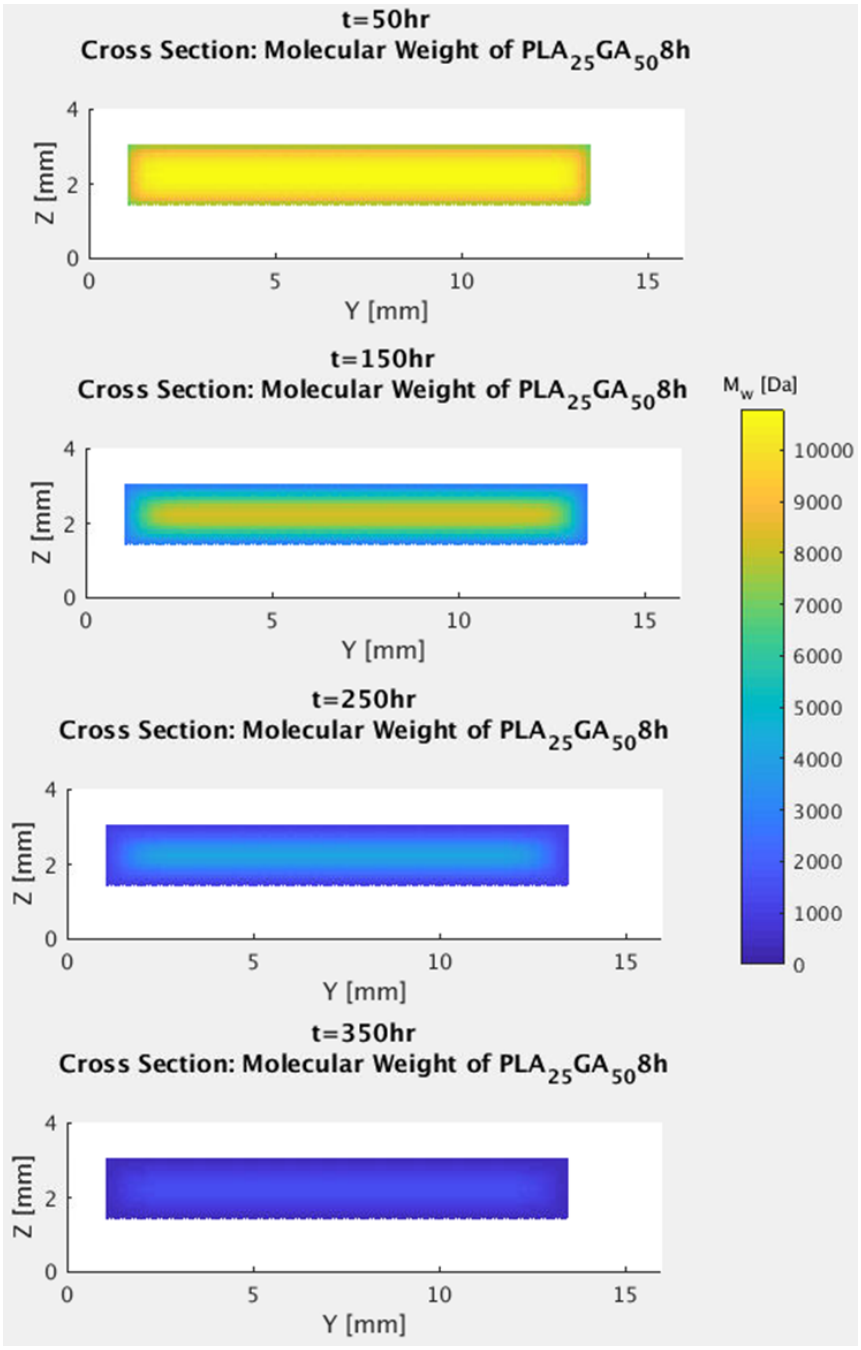

Figure 3.10: Cross section of $PLA_{25}GA_{50}8h$ molecular weight distribution

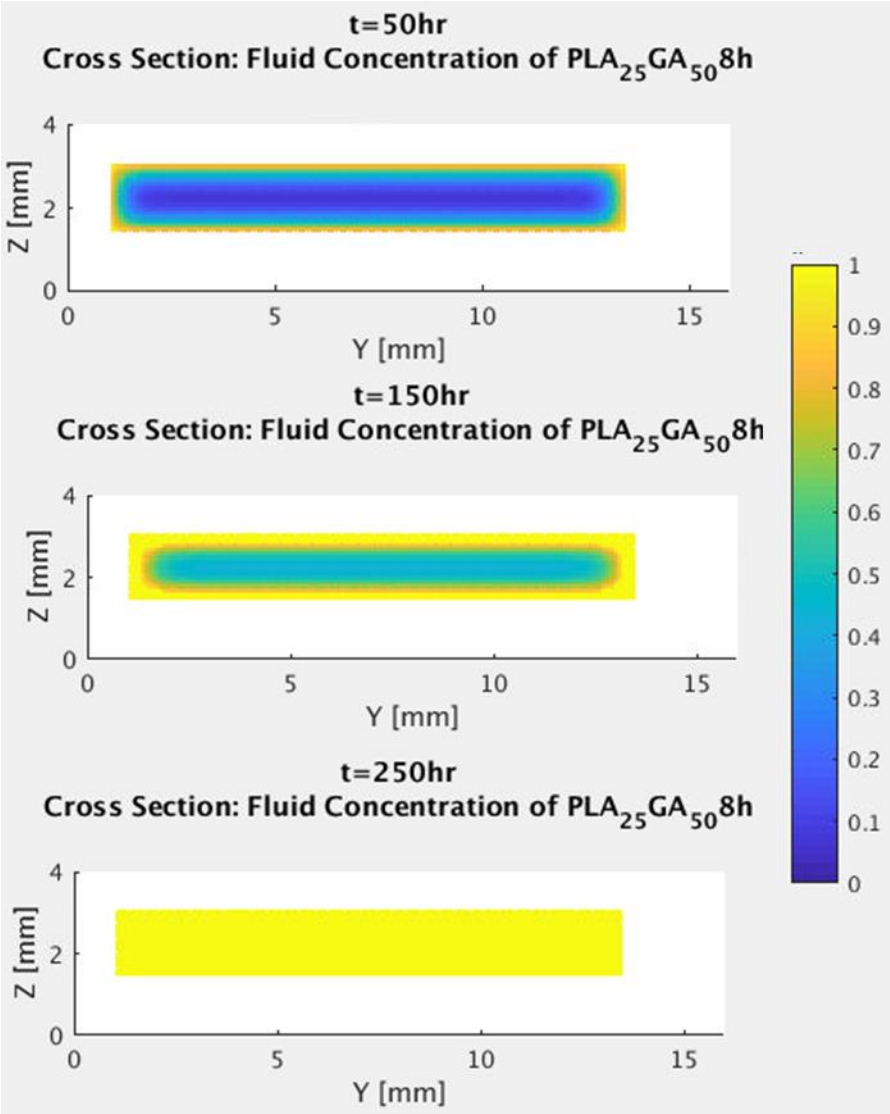

Figure 3.11: Cross section of $PLA_{25}GA_{50}$8h fluid concentration distribution

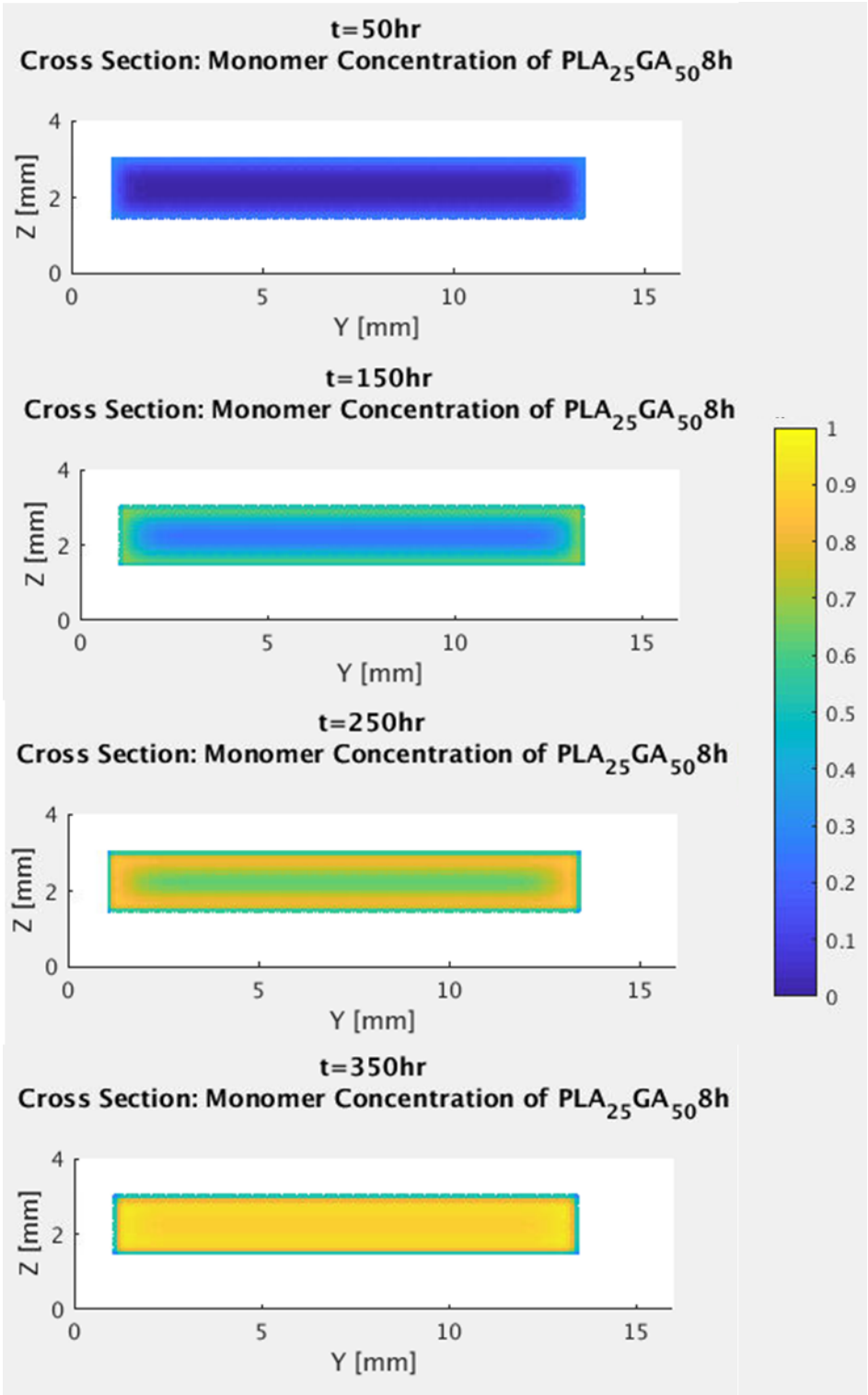

Figure 3.12: Cross section of $PLA_{25}GA_{50}$8h monomer concentration distribution

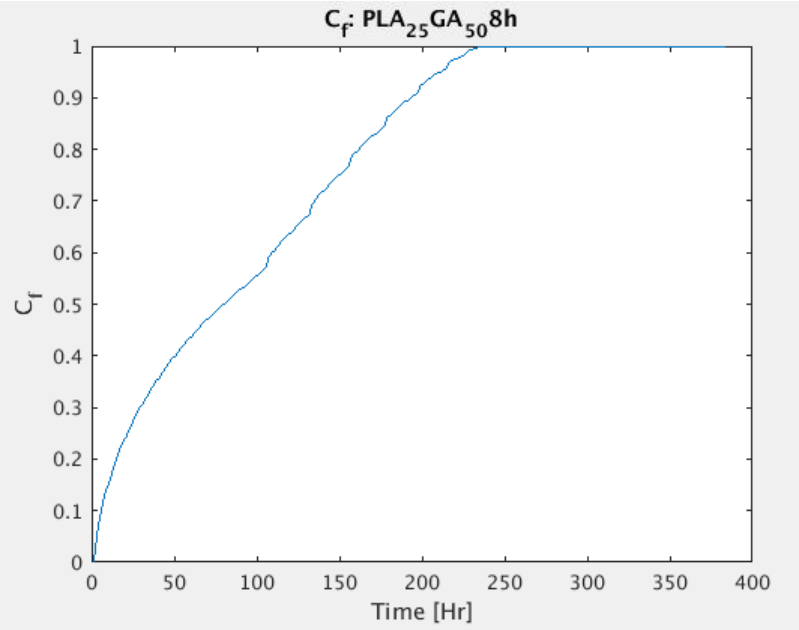

Figure 3.13: Average fluid concentration of $PLA_{25}GA_{50}$8h

The same discretizing values used for $PLA_{25}GA_{50}$8h, which were determined from the convergence study, were used for a higher molecular weight polymer $PLA_{25}GA_{50}$14h. The methods for tuning were identical. The calibrated coefficients and threshold variables that model $PLA_{25}GA_{50}$14h are listed in Table 3.4. The model comparison for molecular weight loss is shown in Figure 3.14. It should be noted that the only calibrated value changed between the two polymers of different molecular weights, besides N_0, was the fluid diffusion constant. As the molecular weight increases, the fluid diffusion into the polymer becomes slower. It should also be noted that the coefficient of monomer diffusion may have physically changed as well; however, as previously mentioned, this could not be confirmed given the experimental data used.

Table 3.4: $PLA_{25}GA_{50}$14h Model Coefficient and Threshold Variables

Coefficient/Threshold	Value
D_f	$1188\ \mu m^2 hr^{-1}$
K_f	$1.8 * 10^{-3} hr^{-1}$
τ_s	$100\ hr$
N_0	$16165\ Da$
D_m	$36\ \mu m^2 hr^{-1}$
$diffusion\ threshold$	$0.02 \leq C_{m,i}$
$erosion\ threshold$	$0.45\ \geq N_i N_0^{-1}$

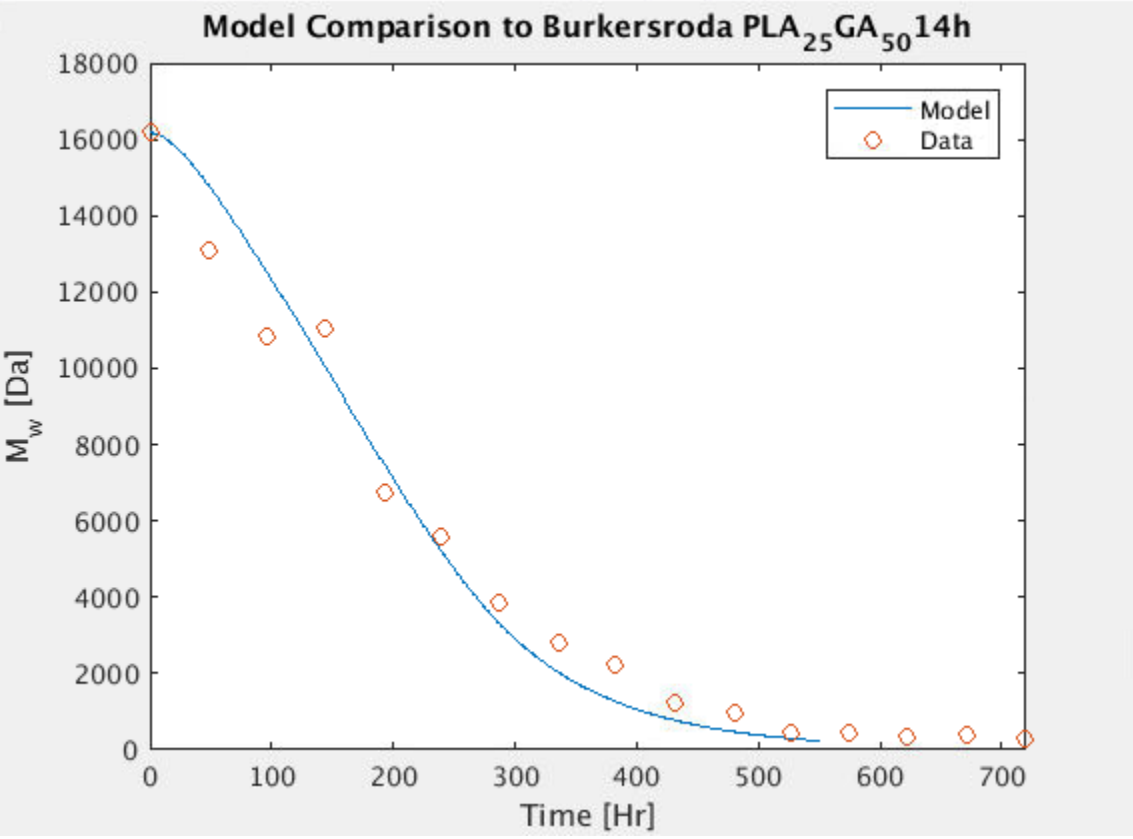

Figure 3.14: Fit model of $PLA_{25}GA_{50}$14h comparison to Burkersroda data

Figures 3.21-23 depict the cross section view of molecular weight, fluid concentration, and monomer concentration distributions respectively. Figures 3.15, 3.16, and 3.17-20 present the side, cross section, and isometric views of molecular weight distribution of the body. Similar to Figures 3.5-9, local molecular weight values falling below 25% of the initial are not included in the figure. Once again, this was done to demonstrate a possible portrayal of shape change.

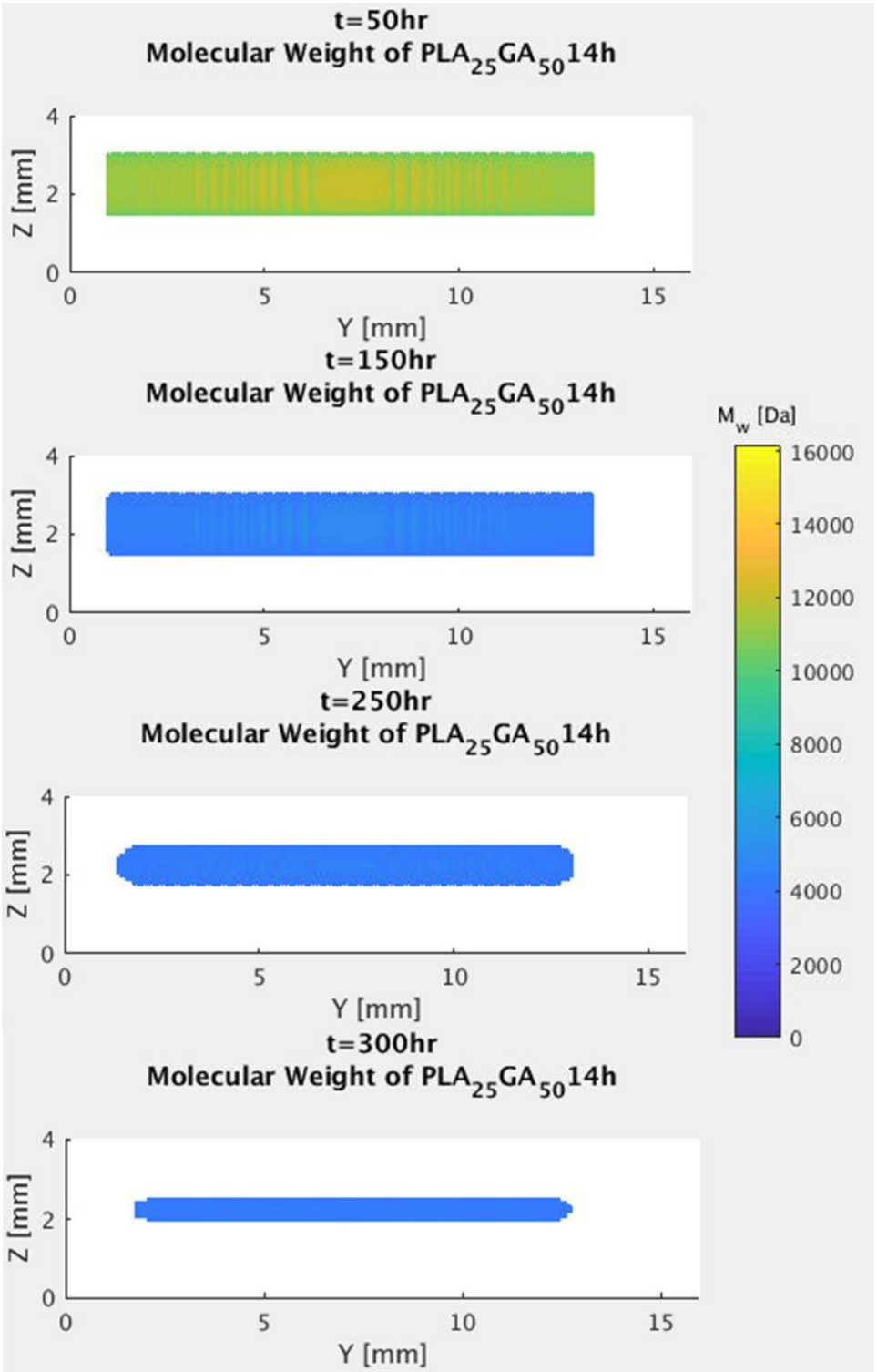

Figure 3.15: Side view of $PLA_{25}GA_{50}$14h molecular weight distribution and erosion. $N > 0.25\ N_0$

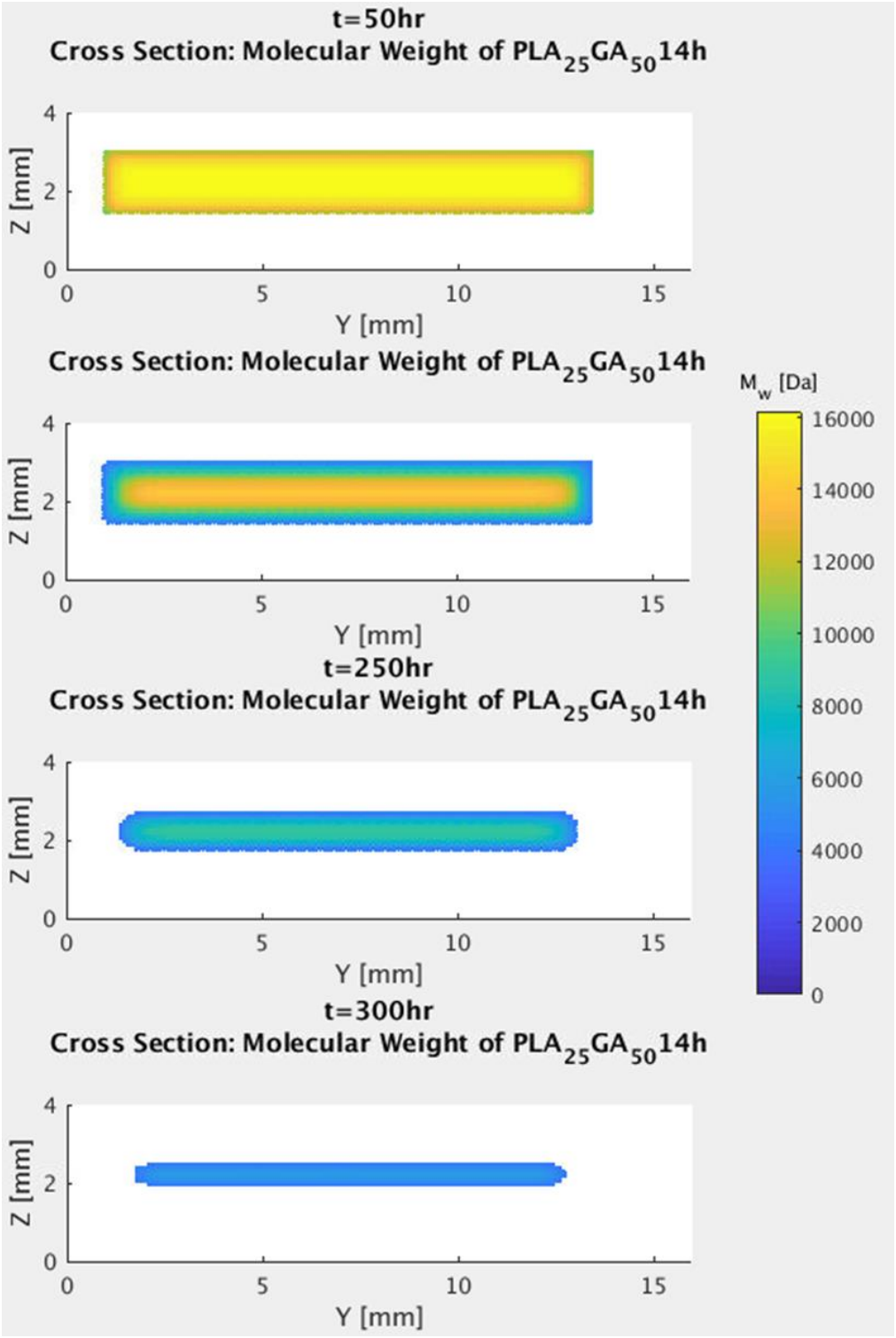

Figure 3.16: Cross section view of $PLA_{25}GA_{50}$14h M_w distribution and erosion. N > 0.25 N_0

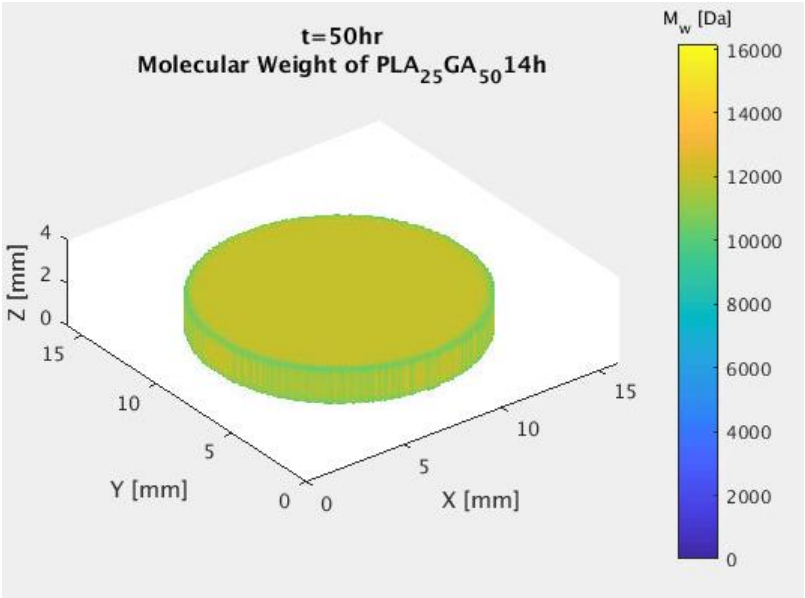

Figure 3.17: Isometric view of $PLA_{25}GA_{50}$14h M_w distribution and erosion at 50hr. N > 0.25

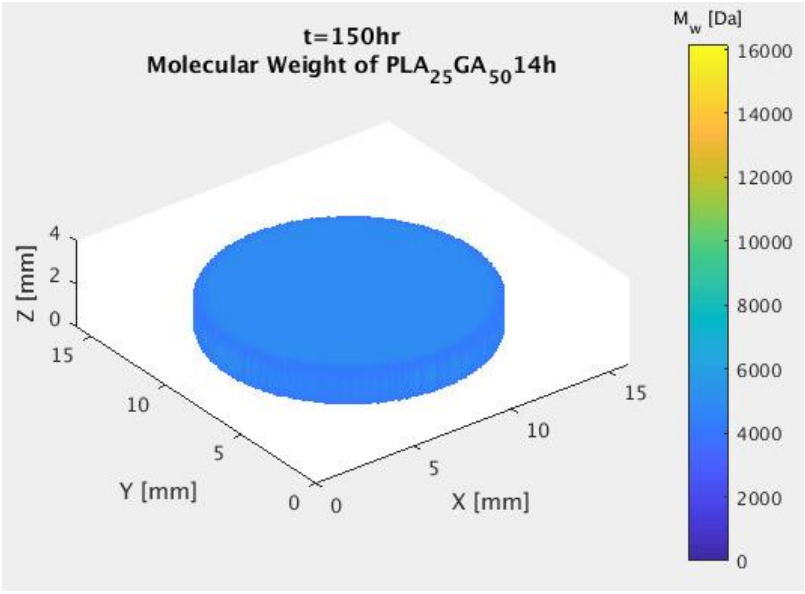

Figure 3.18: Isometric view of $PLA_{25}GA_{50}$14h M_w distribution and erosion at 150hr. N > 0.25

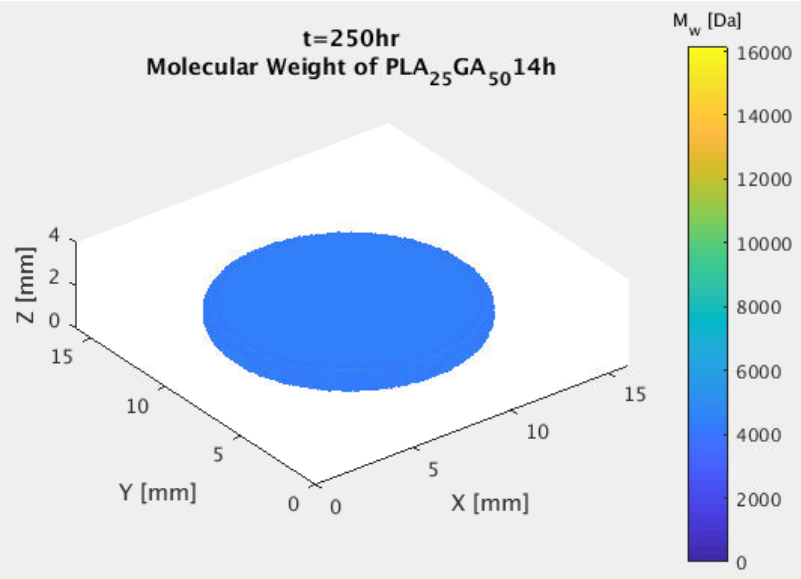

Figure 3.19: Isometric view of $PLA_{25}GA_{50}$14h M_w distribution and erosion at 250hr. N > 0.25

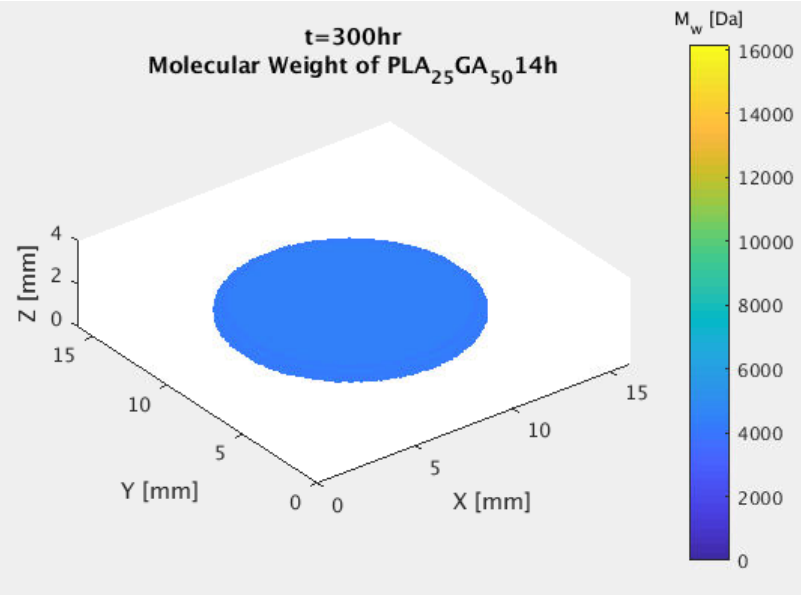

Figure 3.20: Isometric view of $PLA_{25}GA_{50}$14h M_w distribution and erosion at 300hr. N > 0.25

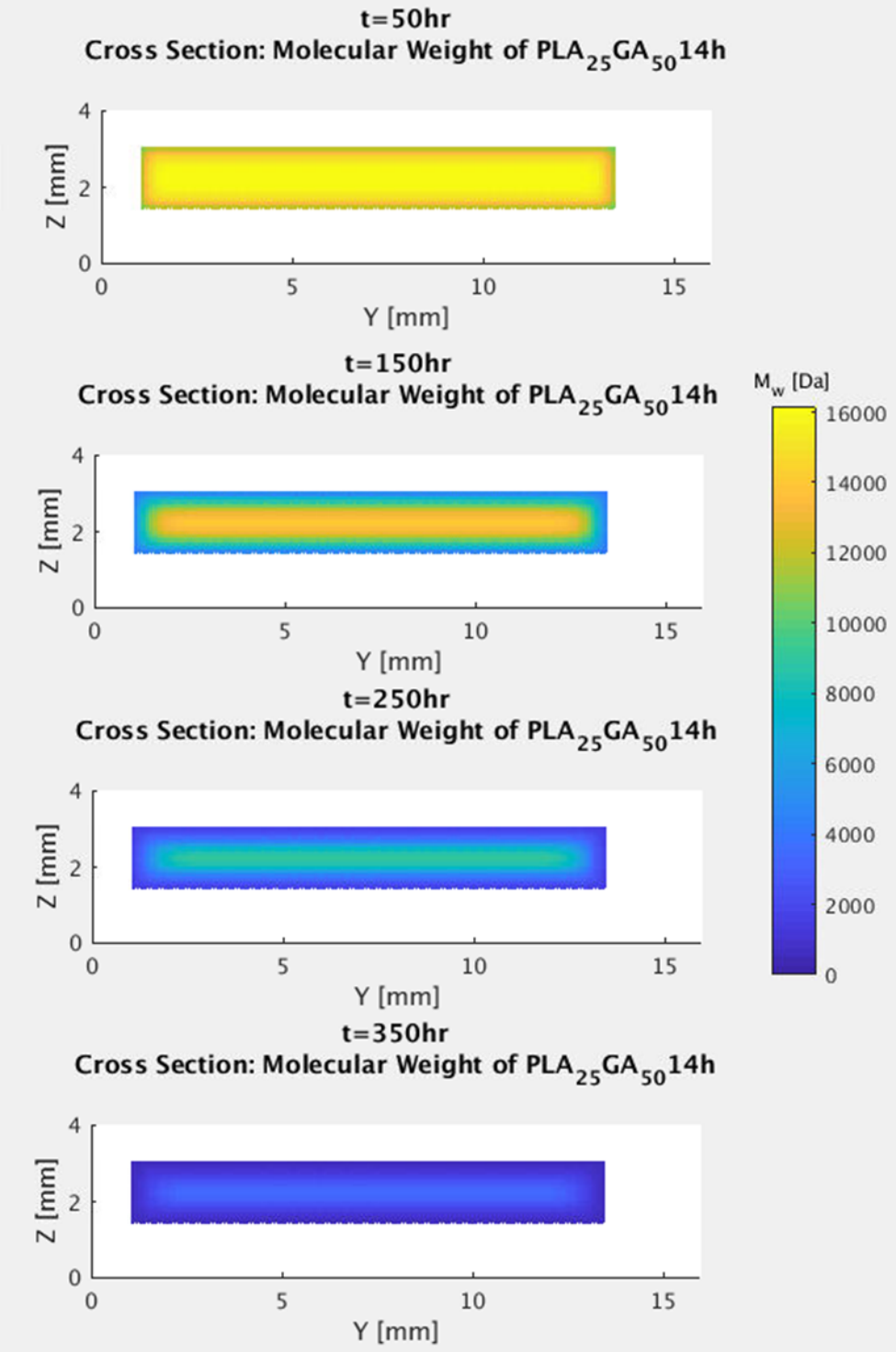

Figure 3.21: Cross section of $PLA_{25}GA_{50}$ 14h molecular weight distribution

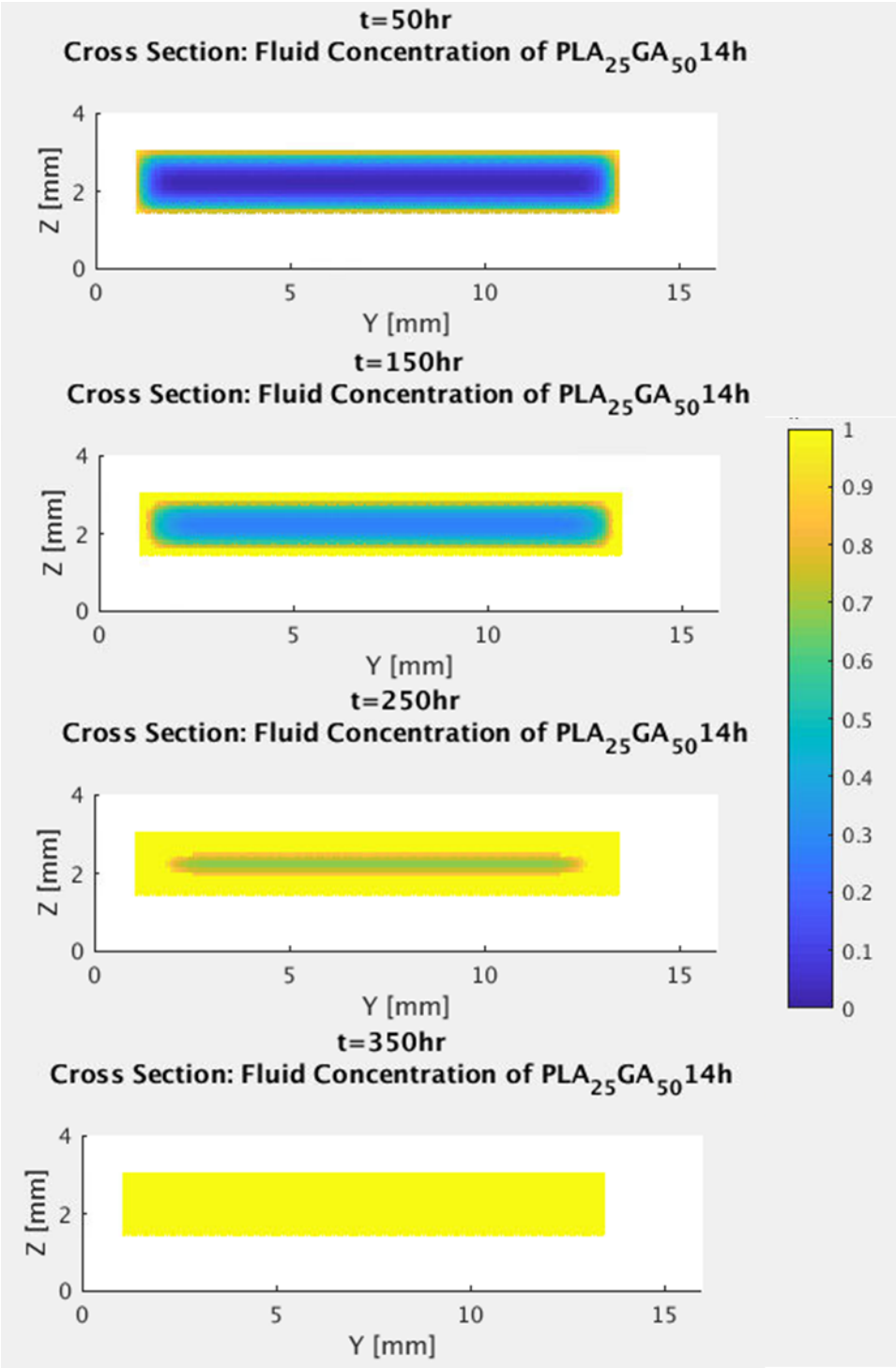

Figure 3.22: Cross section of $PLA_{25}GA_{50}$14h fluid concentration distribution

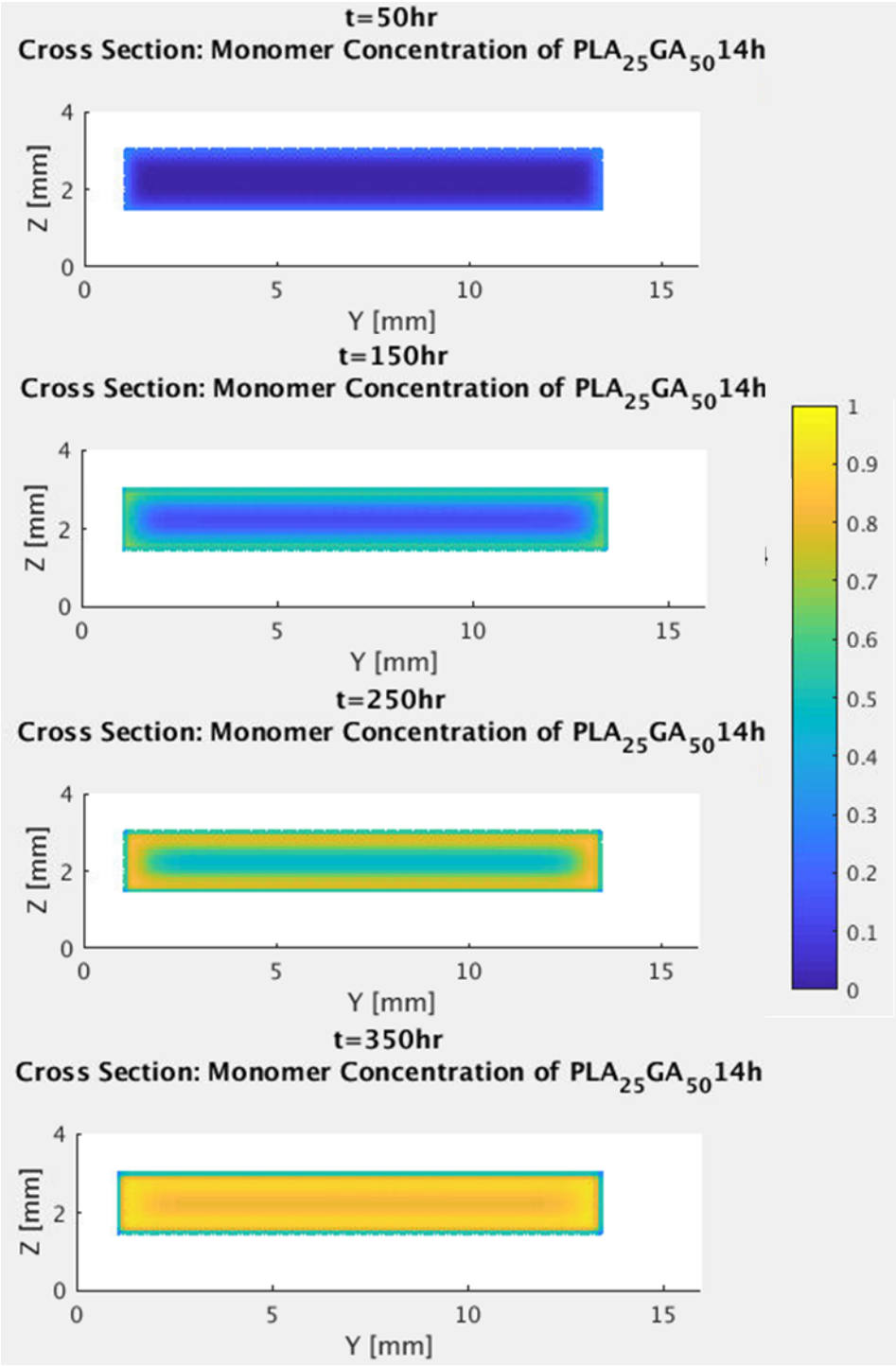

Figure 3.23: Cross section of $PLA_{25}GA_{50}$14h monomer concentration distribution

Sensitivity of Tuned Coefficients

In an attempt to understand the sensitivity of the calibrated coefficients, each of the values were changed from 80% to 120% of their calibrated amounts. Figure 3.24 shows the sensitivity analysis of D_f. With 20% decrease, there is a minor shift in the degradation of molecular weight over 16 days. The initial and final values are comparable; however, the curve during the majority of degradation is where there lies some deviation. With a 20% increase there is, what appears to be, a dramatic change in the degradation behavior. It must be noted that the maximum value of C_f is larger than 1. This does physically not make sense and is simply an artifact of the mathematics used to calculate the curve. The cause of this is likely due to the increased speed of diffusion paired with dimensional and time step sizes to coarse to capture the behavior accurately. While it may be presumed that this increased value is possible, it likely does not work physically because it is not coupled with a corresponding change in other variables due to different polymer properties.

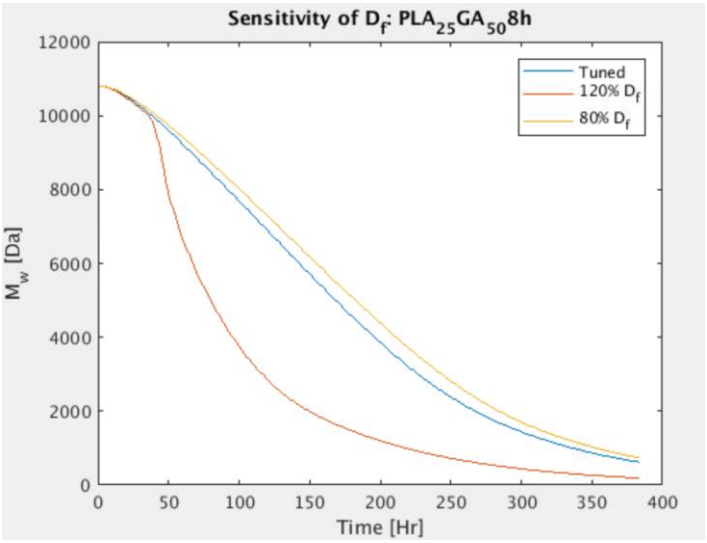

Figure 3.24: Sensitivity of D_f ±20%

Figures 3.25,27-28 show the sensitivity analyses of ±20% for K_f, τ_s, and D_m respectively. The reaction constant changes produce negligible changes in molecular weight degradation. As expected, a smaller value of K_f causes a steeper slope of the degradation curve since more of the water is being used for the process of hydrolytic scission. However, within 20% changes, its effect is negligible. When this value is altered by 400% and 25%, some deviations are seen in Figure 3.26. An increase of 20% of the characteristic degradation time τ_s causes the overall curve to shift up by ~25% at its largest difference. This logically follows as a larger characteristic would necessarily cause an increase in the time needed for degradation. Conversely, a smaller characteristic time causes the model to show a faster degradation. Lastly, changes in D_m have negligible effects upon the molecular weight degradation curve. This is expected. Changes in D_m should influence the erosion rate and hence the mass loss.

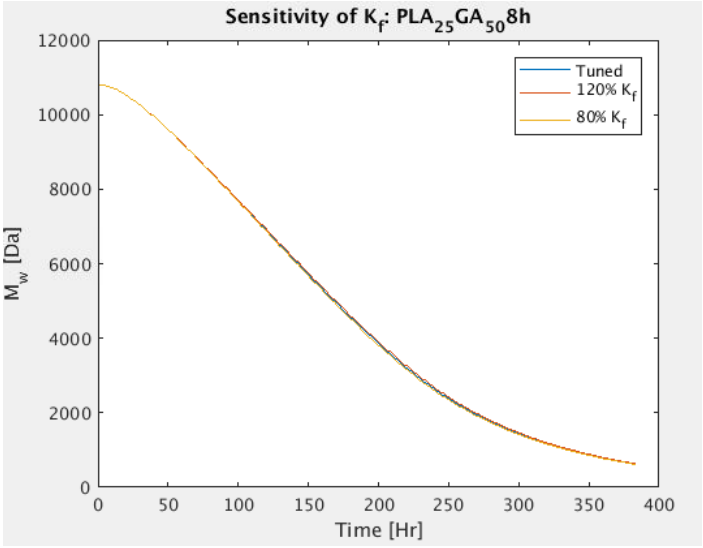

Figure 3.25: Sensitivity of K_f $\pm$20%

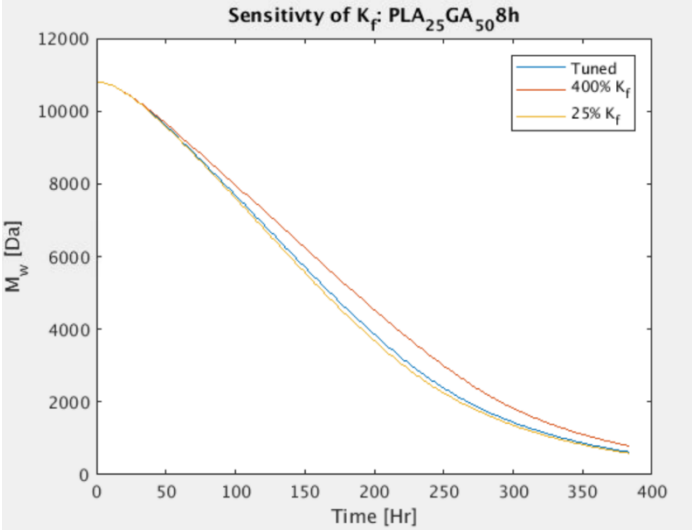

Figure 3.26: Sensitivity of K_f 400% & 25%

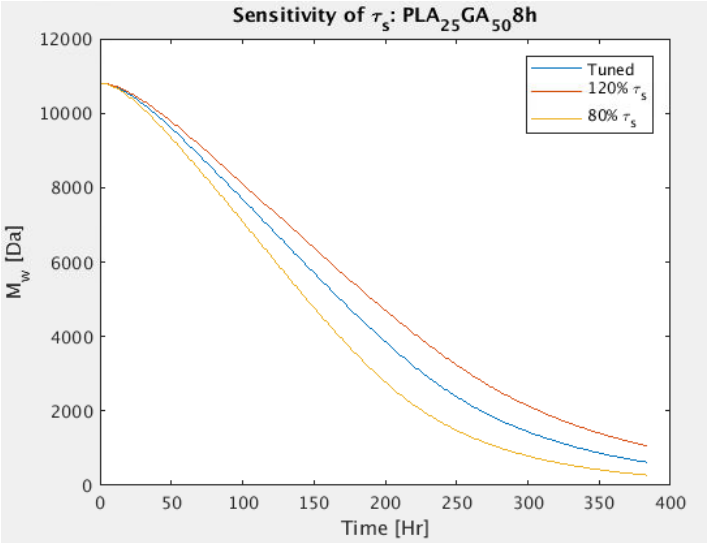

Figure 3.27: Sensitivity of τ_f ±20%

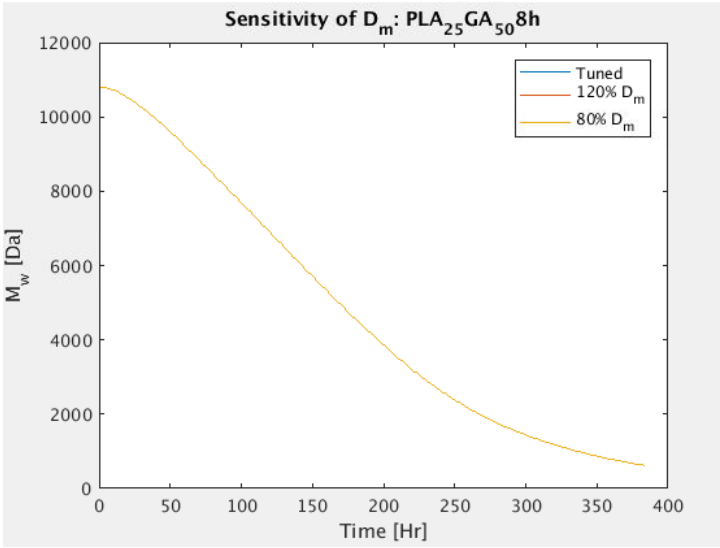

Figure 3.28: Sensitivity of D_m ±20%

Qualitative Discussion of Molecular Weight Erosion Curves

When comparing the graphical cross sections of the cylinders with the average molecular weight degradation and erosion curve, some initial observations can be made

regarding a rough prediction of whether a body is currently undergoing primarily surface or bulk erosion. Many other studies define the erosion process as a binary system, either the body undergoes purely bulk or purely surface erosion. This is often times a simplification done for mathematical and predictive reasons; however, intuitively the system should not behave as such. An erosion process may dominate the overall behavior at a given time, but with changing boundaries, levels of monomers, and fluid concentrations, it is more likely that there is a combination of the two occurring simultaneously. This means that while a body may be losing mass in bulk, it may also exhibit an eroding boundary. From qualitative observations during the experimental modeling portion of this study, it appears that inflection point of the average molecular weight erosion is a good metric for determining when one erosion behavior begins to increase in proportion. The approximate locations of these inflections are seen in Figures 3.29 and 3.30 for $PLA_{25}GA_{50}$8h and $PLA_{25}GA_{50}$14h respectively. When a curvature is negative, the body demonstrates a growing level of surface erosion, and when a curvature is positive, the body demonstrates primarily bulk erosion. For example, both $PLA_{25}GA_{50}$8h and $PLA_{25}GA_{50}$14h appear to undergo surface erosion closer to $t=t_0$, but, at t ~180hr and ~270hr respectively, eventually demonstrate a growingly stronger bulk erosion. This is not to say that the switch is immediate. At the point of inflection the body is still losing a non-negligible amount mass at the surface, this is instead implying that bulk erosion is becoming the dominant mechanism. The presumption is that this is true for multi-axially symmetric bodies, or at least simple shapes. This feature is to be further discussed in section 3.3.

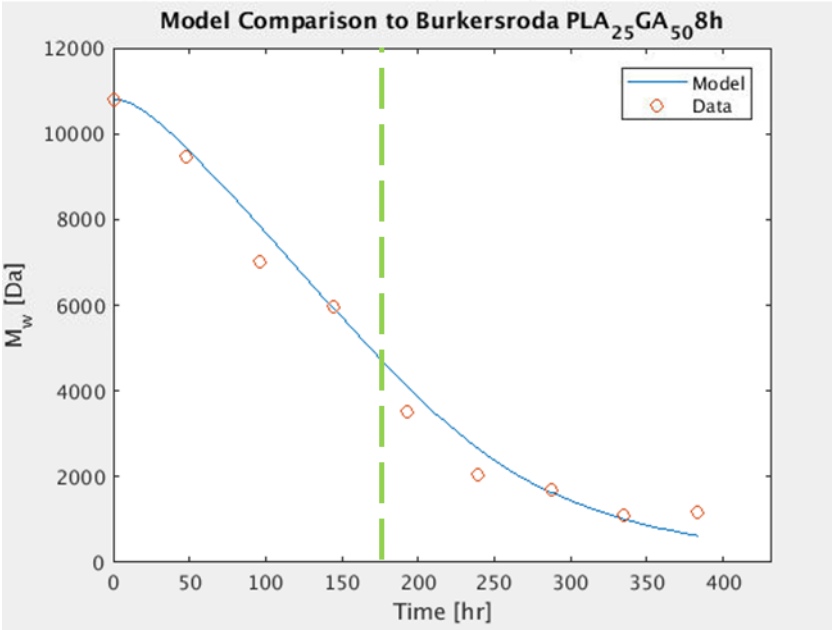

Figure 3.29: Approximate inflection of $PLA_{25}GA_{50}$8h molecular weight

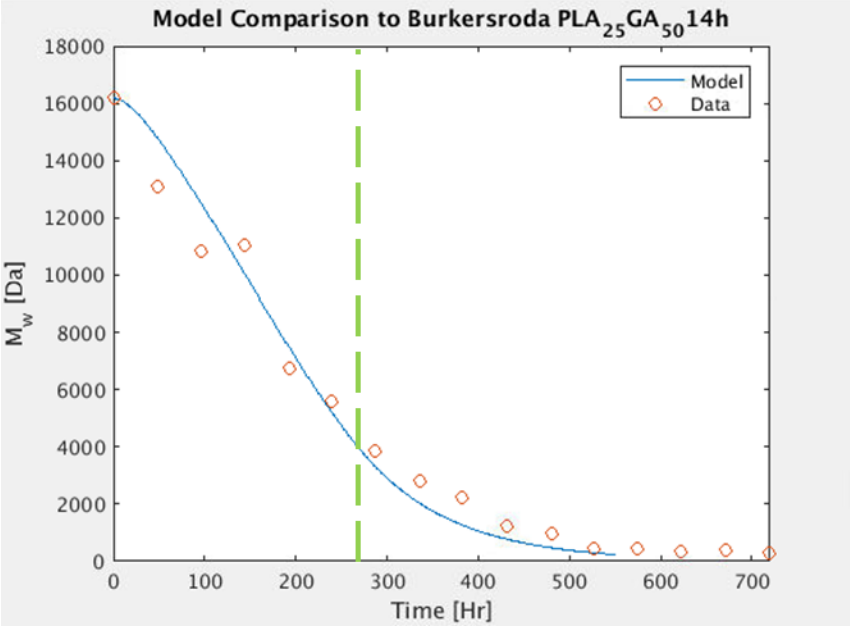

Figure 3.30: Approximate inflection of $PLA_{25}GA_{50}$14h molecular weight

3.3. Realistic Scaffold Erosion Analysis

To demonstrate the capabilities of this model, a realistic single cell of a cross-hatched patterned stent was simulated. The 3D file created for this study was made using SolidWorks, a CAD software offered to students of the Department of Mechanical Engineering at Texas A&M University. This model is based upon the stent design detailed in a thesis by Murphy [33]. The geometry represents cardiovascular stents currently used in the market. As stated by Murphy, this stent has an inner diameter of 2.4mm, a thickness of 100µm, and a total length of 20mm [33]. A single cell of this stent model has a length of approximately 1.8mm. The file created for this study is seen in Figure 3.31 and the general wireframe mesh structure used for discretization is seen in Figure 3.32.

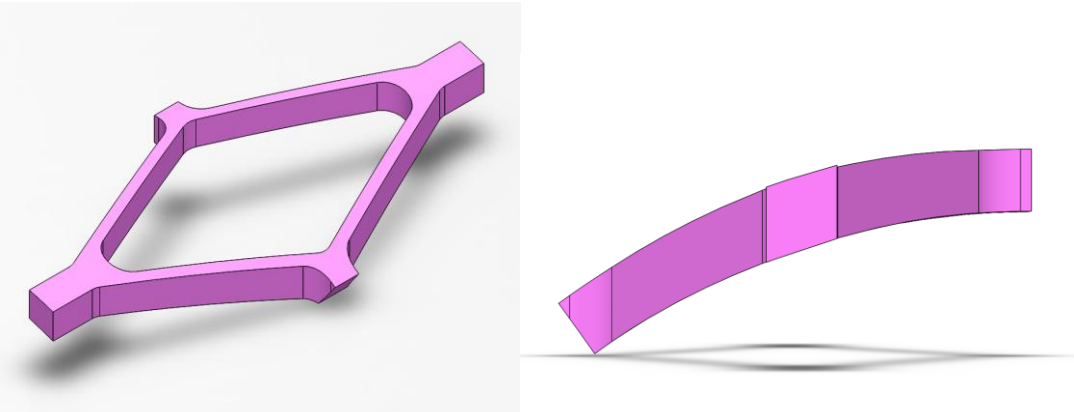

Figure 3.31: Single cell of cross-hatched pattern stent. Left: Isometric view. Right: Side view

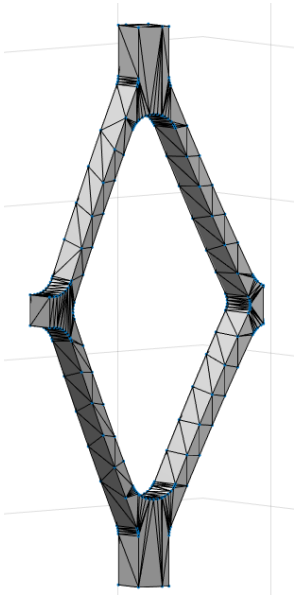

Figure 3.32: Wireframe stent in MATLAB for discretization

To simulate the erosion behavior of this stent, a convergence study was performed in order to minimize deviation due to coarsely defined nodes and time steps. A time step of 3 minutes, or 0.05 hours, was implemented due to the thin walled features of a single cell of the stent. The step size sufficiently met the computational stability requirement previously mentioned in Equation (9). Dimensional step sizes were kept uniform among $\Delta x,y,z$. The step sizes studied were 100µm, 50µm, 40µm, and 25µm. The results of this study are graphically shown in Figure 3.33 and tabulated in Table 3.5. A step size of 25µm was determined to produce the best results. Although 40µm would have produced a deviation of only 0.1% and significant computational savings, 25µm subjectively performed better than 40µm on the capture of the complex geometry of this body. Given the model's thin features, this metric was of great importance in the analysis of stent degradation. The discretized body is shown in Figure 3.34

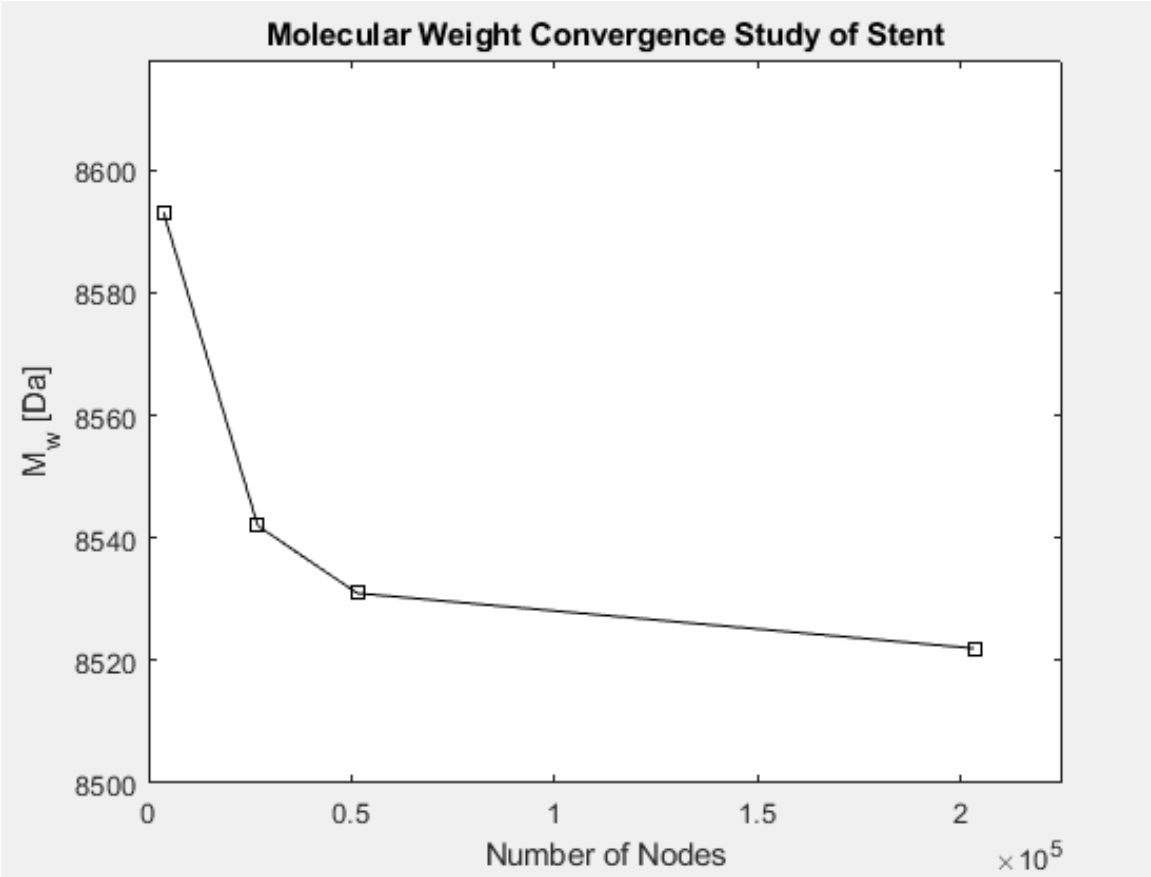

Figure 3.33: Convergence plot of single stent cell

Table 3.5: Number of nodes and the respective average molecular weight of stent

Number of Nodes	$\boldsymbol{M_{w,avg}\ \Delta t = 0.05hr}$
3751	8593
26901	8542
51376	8531
203401	8522

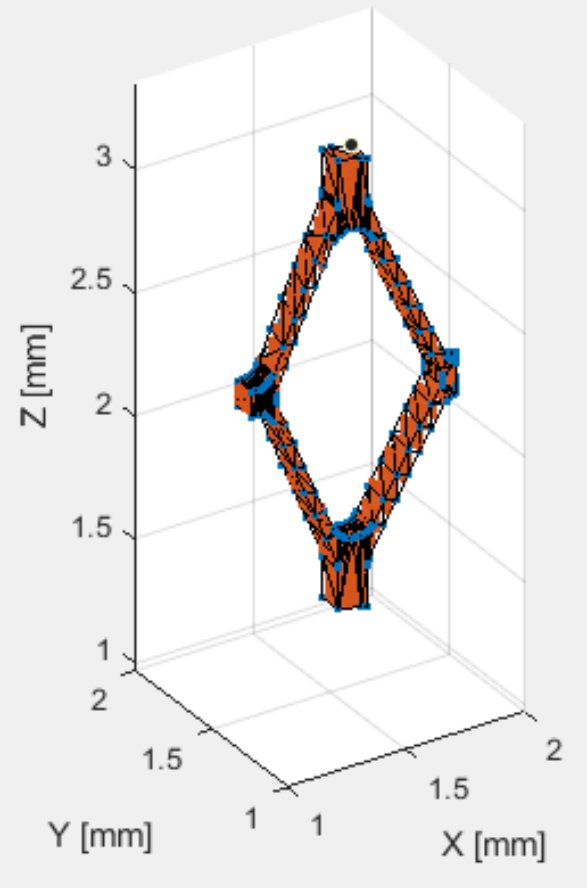

Figure 3.34: Discretized stent cell - 25µm

The simulation for this cross-hatched stent cell modeled the degradation and erosion over 6 days - 144 hours. This time frame allows for the molecular weight of the body to reach about 20% of the initial value. The coefficients and threshold values used within this model were based upon the analysis of the Burkersroda study over $PLA_{25}GA_{50}$8h and were previously seen in Table 3.3. The overall molecular weight loss is shown in Figure 3.35 and was calculated in the same manner as the molecular weight loss in section 3.2. It is noted that stents are typically intended for longer durations (6-18 months) and different biodegradable polymers with slower degradation processes, such as

PLLA, are typically considered instead of PLGA with a relatively short degradation time. The present study is intended to discuss the qualitative study of the degradation in more complex geometries without calibrating different material parameters for different polymers.

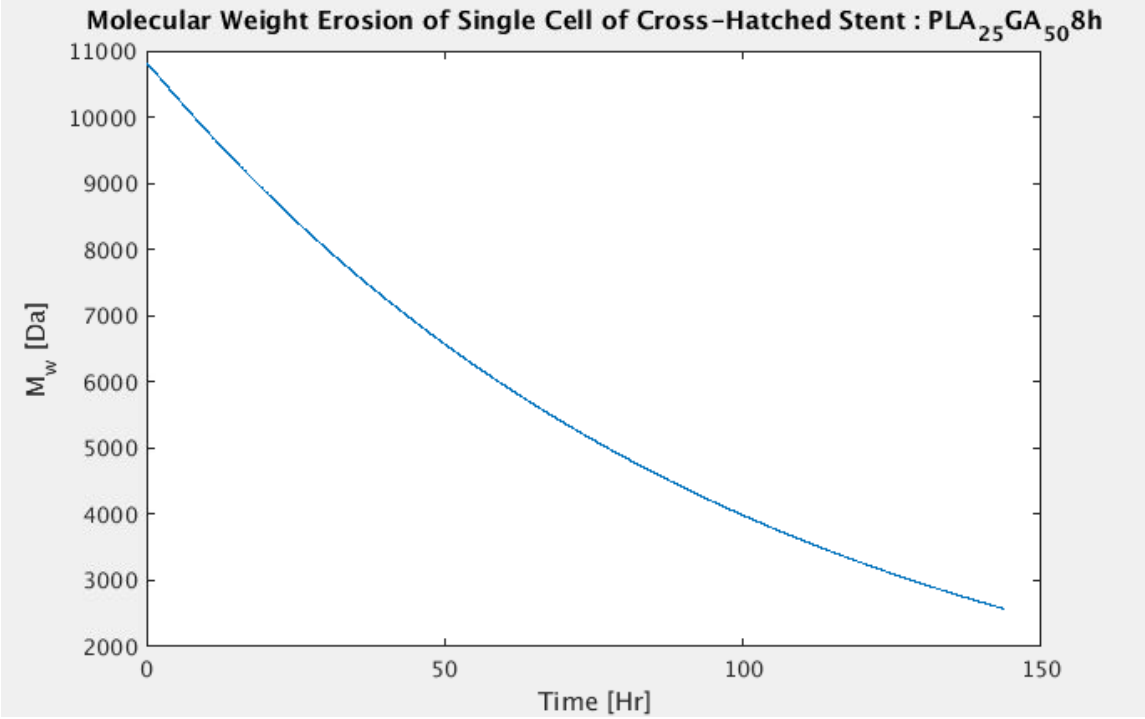

Figure 3.35: Molecular weight erosion of single cell of cross-hatched stent

Figures 3.36-38 depict the changes of molecular weight, fluid concentration, and monomer concentration distributions respectively. Figure 3.39 shows the monomer concentration distribution at 144hr, but with a change in the color scale. This is done to more easily see the monomer concentration gradient. Key features of this degradation model are:

- Molecular weight loss is relatively uniform among the body. This indicates that the body exhibits bulk erosion.
- Total fluid saturation occurs almost entirely within the first hour. This is directly due to the thin features of the stent and comparatively fast fluid diffusion.
- Because of thin body features, monomer concentration distribution remains below 0.2. This is directly due to the relatively fast diffusion of monomers out of the body in comparison to the thin model.

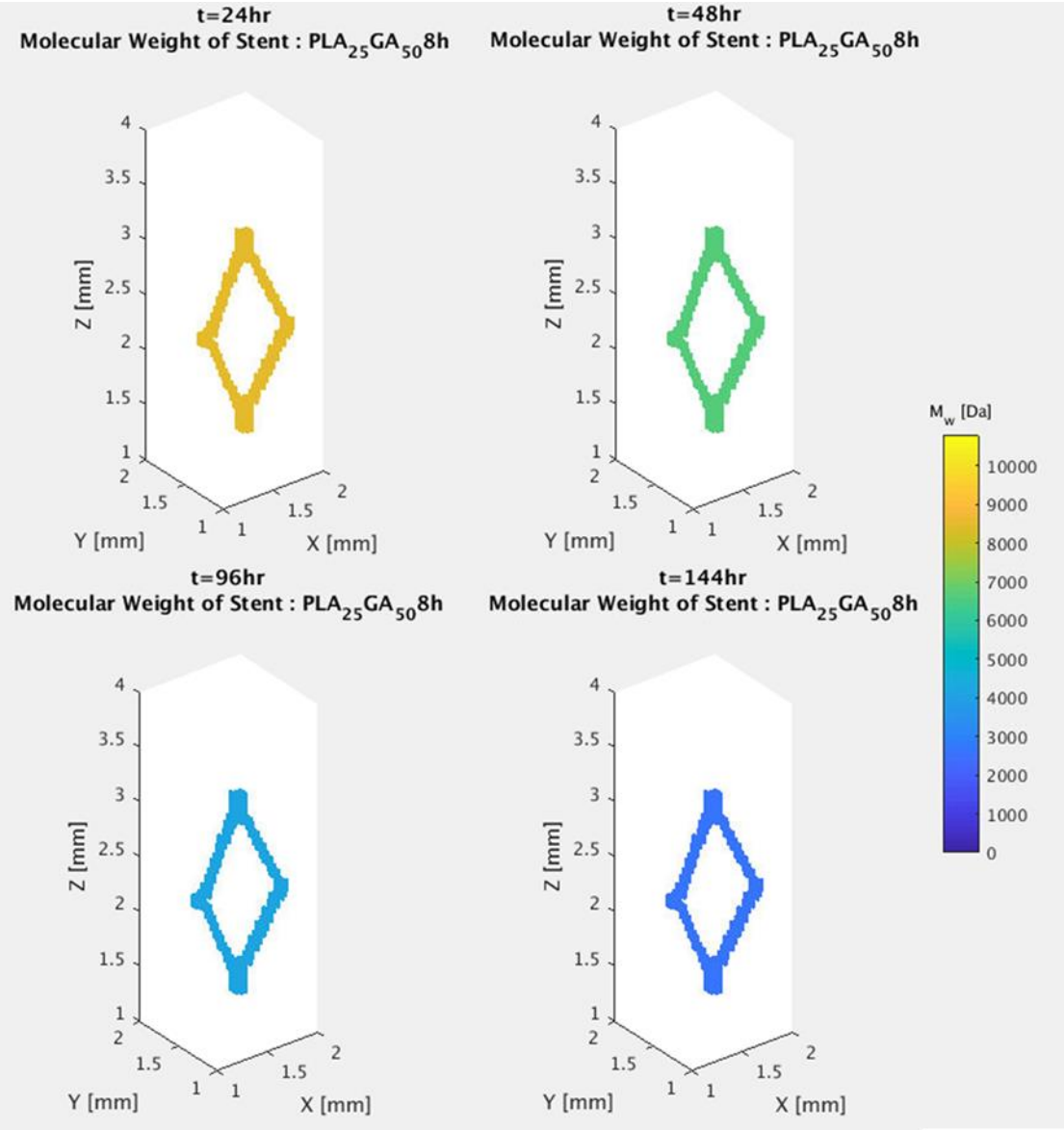

Figure 3.36: Molecular weight distribution of stent model

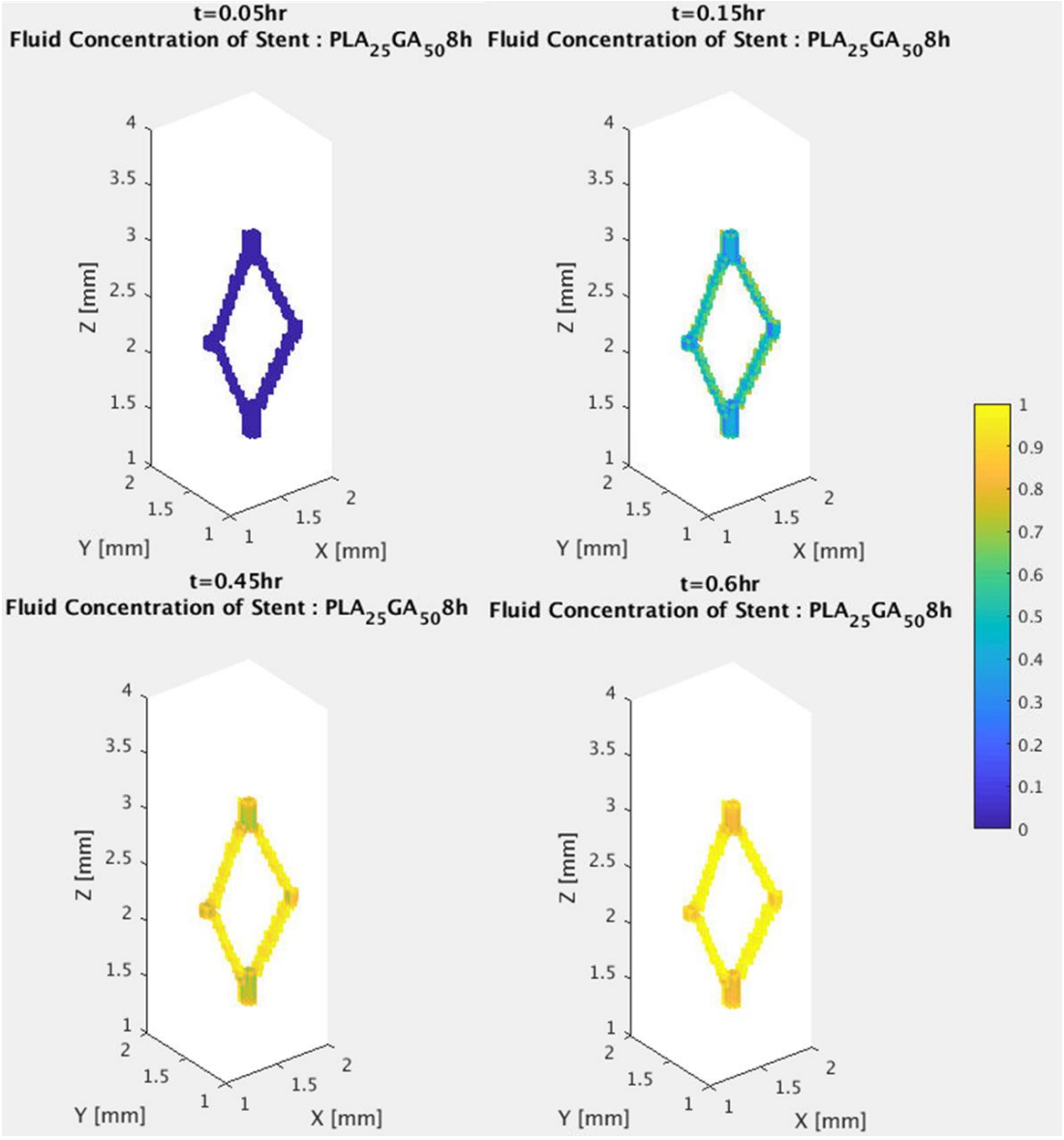

Figure 3.37: Fluid concentration distribution of stent model

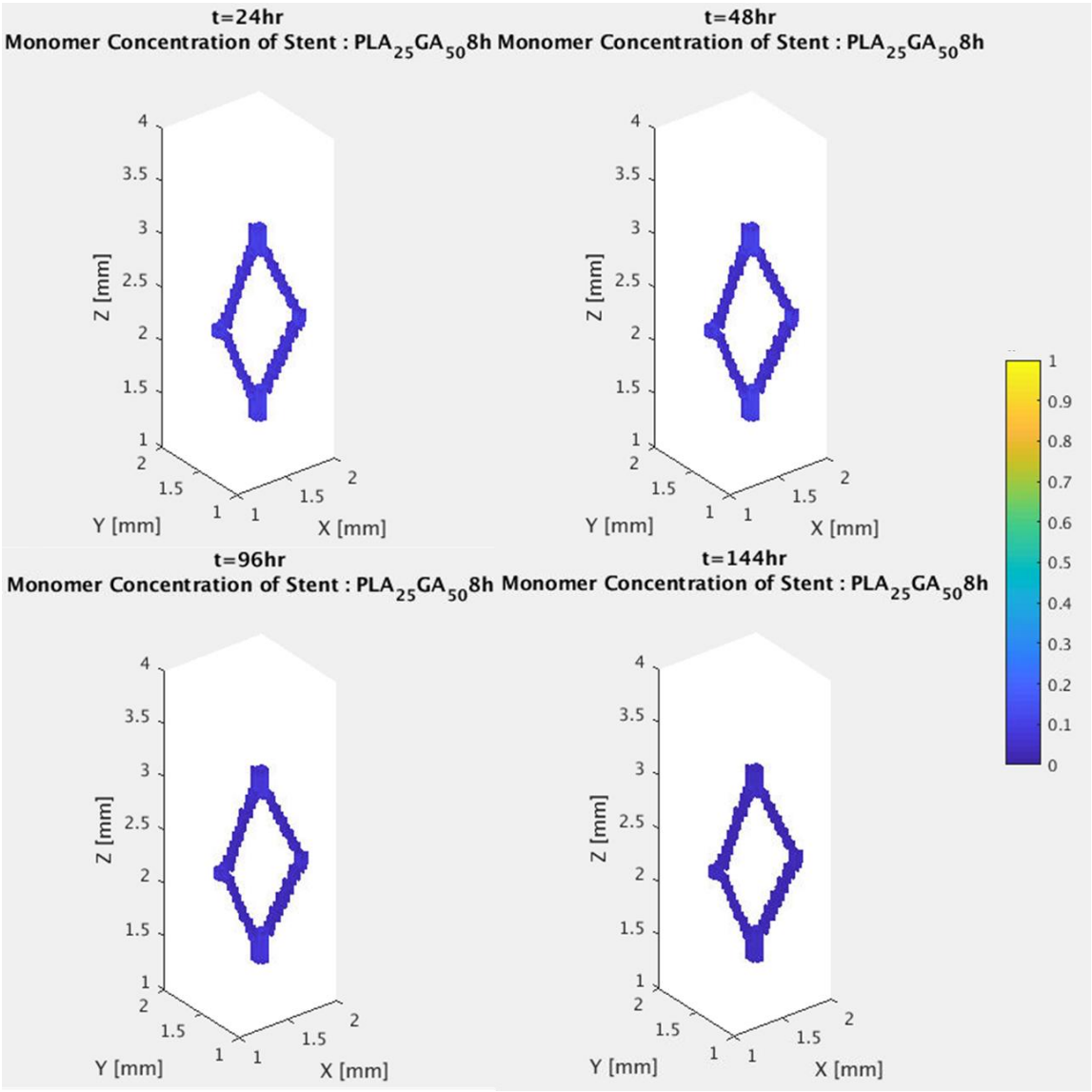

Figure 3.38: Monomer concentration distribution of stent model

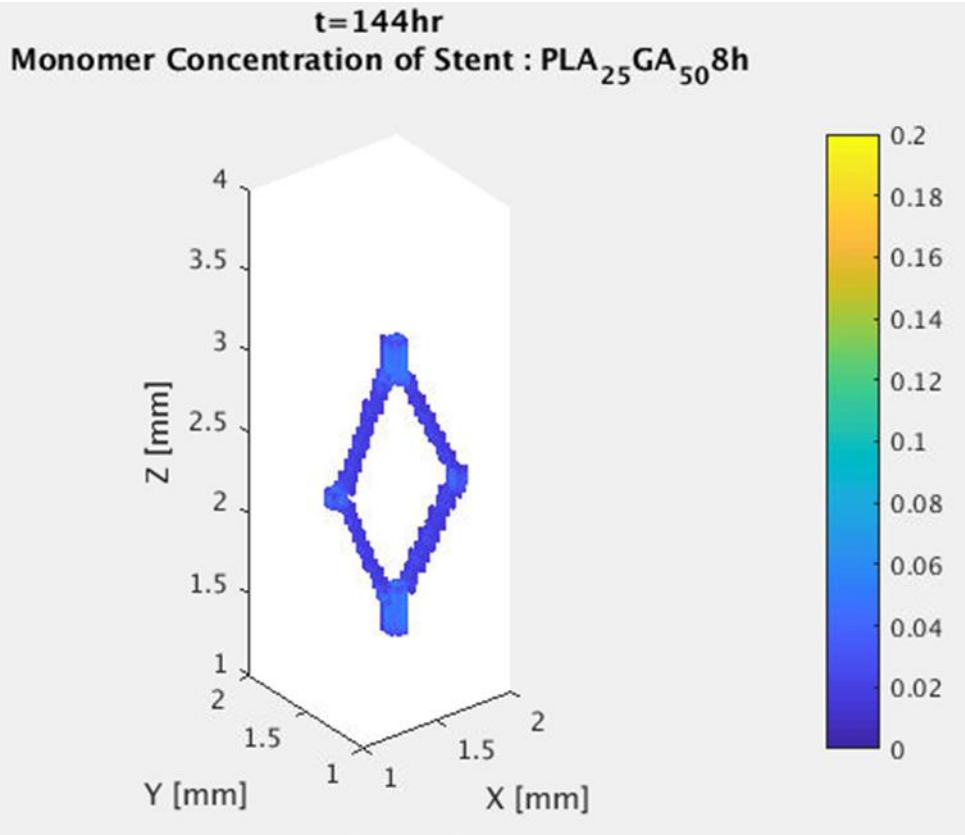

Figure 3.39: Monomer concentration distribution of stent with modified scale

3.4. Complex Geometry Modeling

As seen from the previous section on the model's use to analyze the degradation and erosion behaviors of a cardiovascular stent, this model can capture complex geometries with multi-scale features such as fillets, curvature, and thin walls. To further demonstrate this model's ability to capture complex geometries changes due to erosion, two new bodies are presented: a perforated cylinder based upon the Burkersroda cylinder used in sections 3.1-2 and an indented cube.

Perforated Cylinder

The perforated cylinder is based upon the cylindrical body used in sections 3.1-2 for the experimental modeling of Burkersroda's data. This body, seen in Figure 3.40, was created to demonstrate that a biaxially symmetric body is not required as an input for the created simulation. The modified cylinder contains holes, or perforations, of varying diameters and placement. Some of these holes are intentionally connected and placed on the edge as a means to create sharp features and larger surface areas for diffusion.

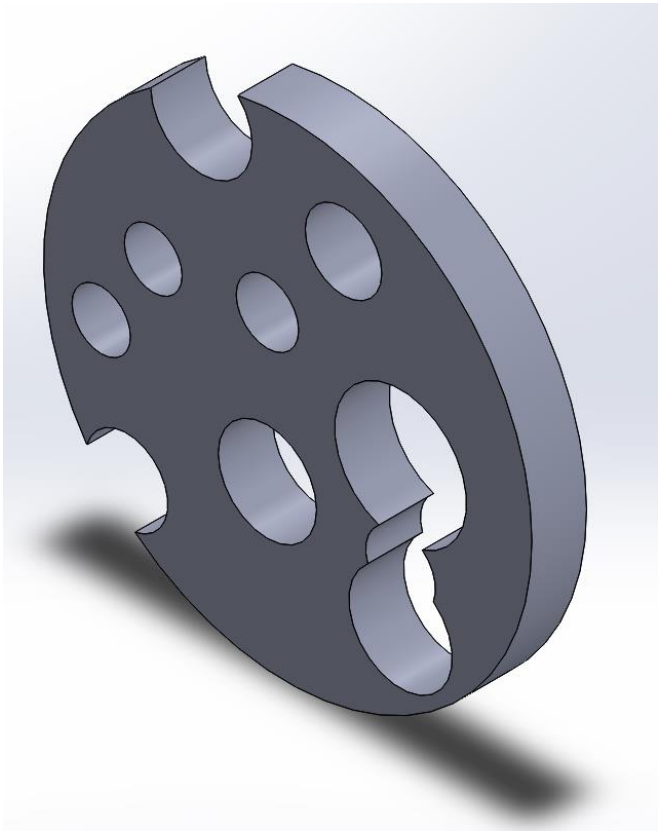

Figure 3.40: Isometric view of mock cylinder with perforations of varying diameters and placement

Because the body is based upon the cylinder used in a previous section, the dimensional discretization step size of 100μm is used; however, the time step is reduced to 30 minutes, or 0.5hr, due to the larger surface areas created by the perforations that induce faster diffusion and degradation. The isometric and top down views of the discretized perforated cylinder are seen in Figures 3.41 and 3.42 respectively.

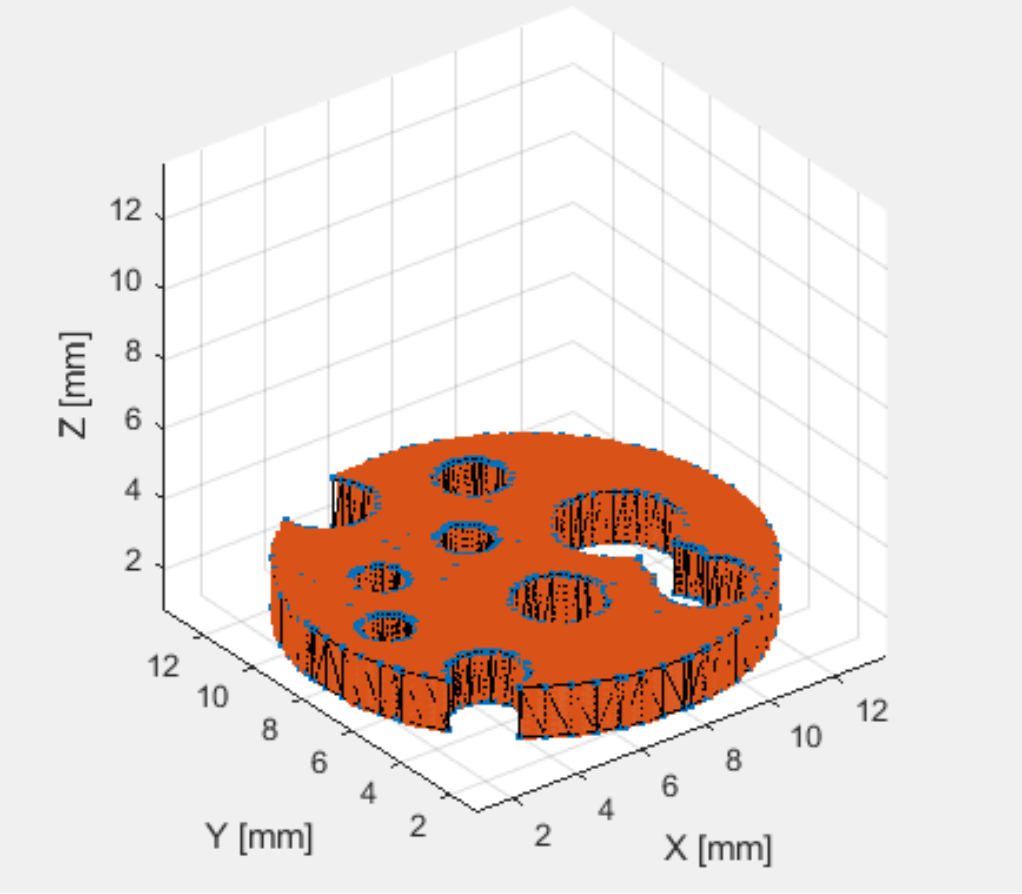

Figure 3.41: Discretized perforated cylinder

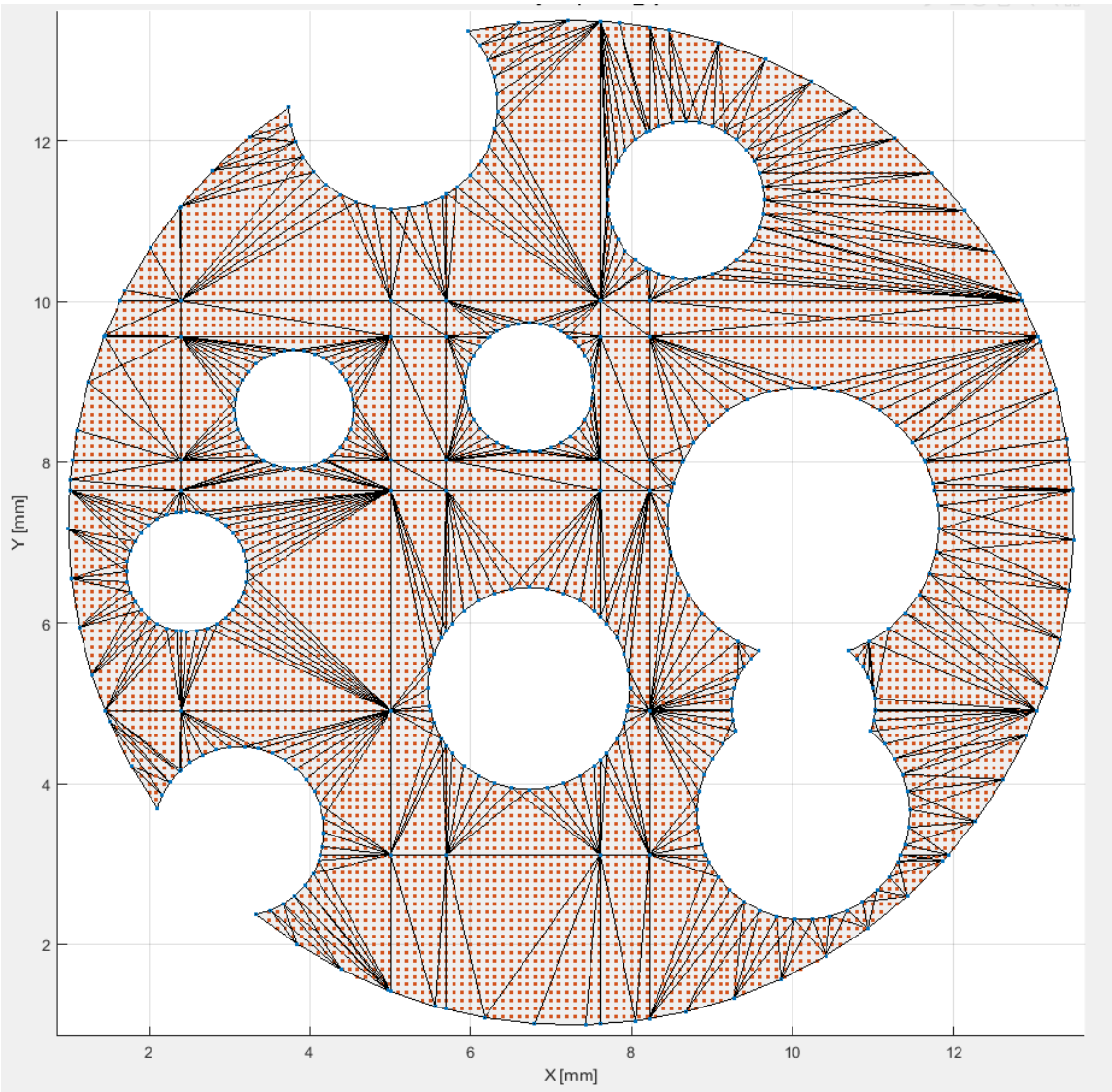

Figure 3.42: Top down view of discretized perforated cylinder

The molecular weight loss of this body over 288 hours, or 12 days, is seen in Figure 3.43. As is indicated by the curvature of the average molecular weight across the body from t=0 to t~120, the perforated cylinder first undergoes surface erosion. After fluid had a sufficient time to evenly diffuse into the body, the cylinder then exhibits a significant bulk erosion.

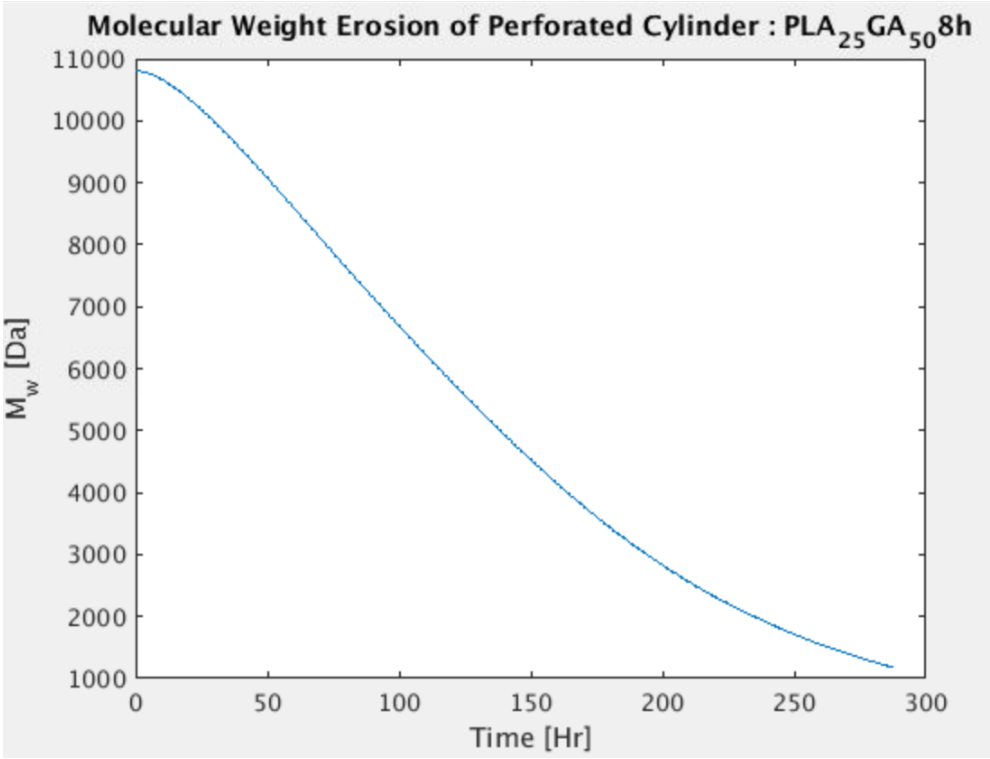

Figure 3.43: Molecular weight erosion of perforated cylinder

Figures 3.44-48 present the erosion and subsequent geometric changes due to the loss of molecular weight over 250 hours, or approximately 10.4 days. As was predicted, erosion caused perforations to become larger and eventually intersect with each other. Locations with larger perforations eroded at a much greater rate when compared to those with smaller perforations. It should be noted Figure 3.48 was unable to take advantage of surface meshing. Surface meshing has been used on all single body models. It does not change the data or the geometry. The intent is to create an easier to see graphical portrayal of the boundary. The algorithm in MATLAB that is employed to create surfaces is unable

to accurately capture the multiple bodies created from erosion in the aforementioned figure.

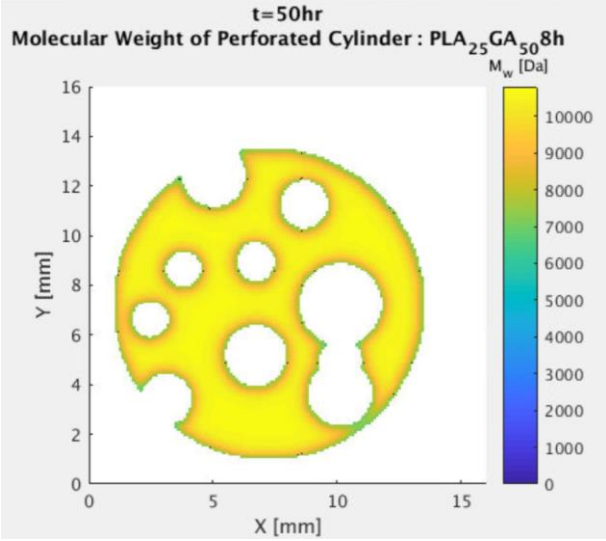

Figure 3.44: Cross section of perforated cylinder molecular weight distribution at 50hr. N > 0.25 N_0

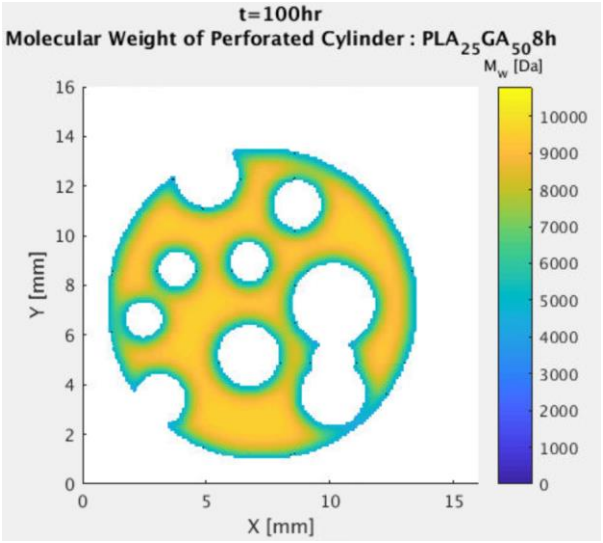

Figure 3.45: Cross section of perforated cylinder molecular weight distribution at 100hr. N > 0.25 N_0

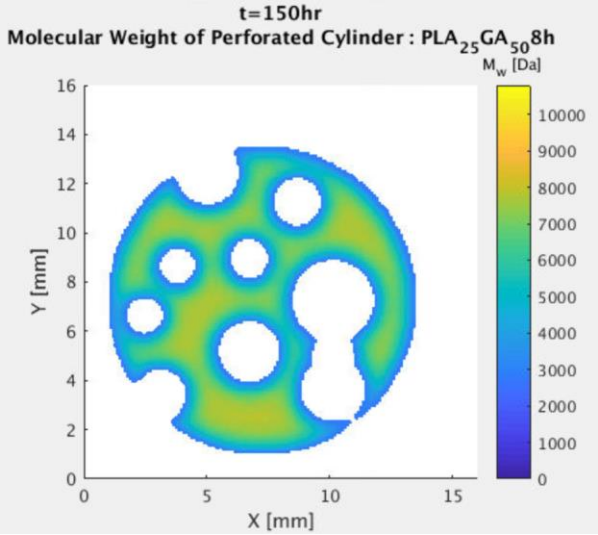

Figure 3.46: Cross section of perforated cylinder molecular weight distribution at 150hr. N > 0.25 N_0

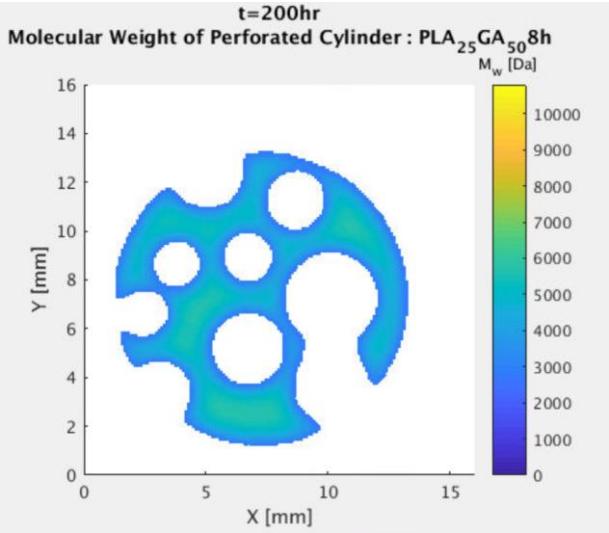

Figure 3.47: Cross section of perforated cylinder molecular weight distribution at 200hr. N > 0.25 N_0

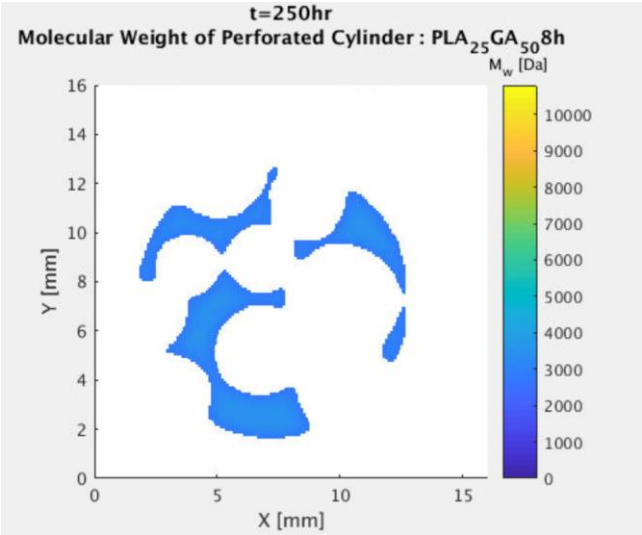

Figure 3.48: Cross section of perforated cylinder molecular weight distribution at 250hr. N > 0.25 N_0

An interesting artefact of erosion due to the varying diameters and placement of perforations are the varying heights of the eroded body. Figure 3.49 shows this phenomena graphically. In the uniform thin cylinder used in sections 3.1 and 3.2, the height, less the edges, remains relatively uniform over the course of erosion; however, during this perforated cylinder simulation that was note the case. Regions of the body that still remain, but experienced a larger degree of erosion due to their proximity to either the edge or other pores, end up having a thinner section after the hydrolytic process occurs.

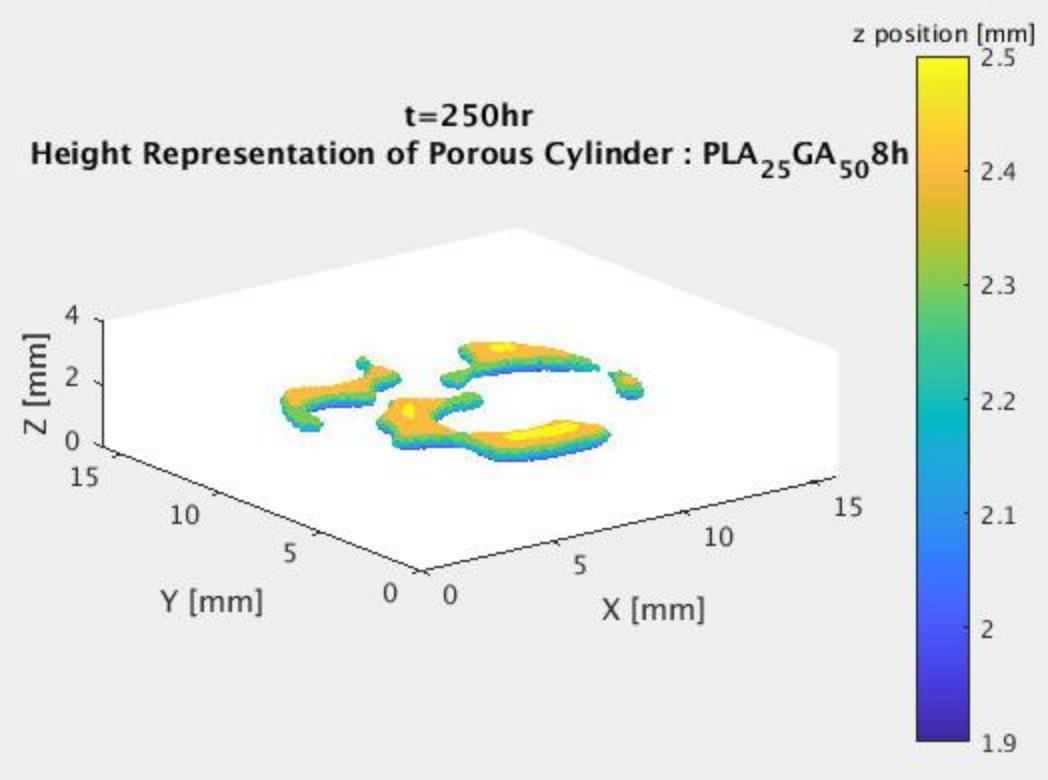

Figure 3.49: Height representation of perforated cylinder at 250hr

Figures 3.50-53 present the cross section of the body and the fluid concentration diffusion over 200 hours, or approximately 8.3 days. As was indicated from the erosion plots, larger volumes of polymeric body were saturated around larger perforations. Locations where perforations were close to one another showed that fluid was eventually able to diffuse into the body and reach other regions of full saturation caused by other perforations. Between 150 and 200 hours, or 6.25 to ~8.3 days, the perforated cylinder reached near full saturation.

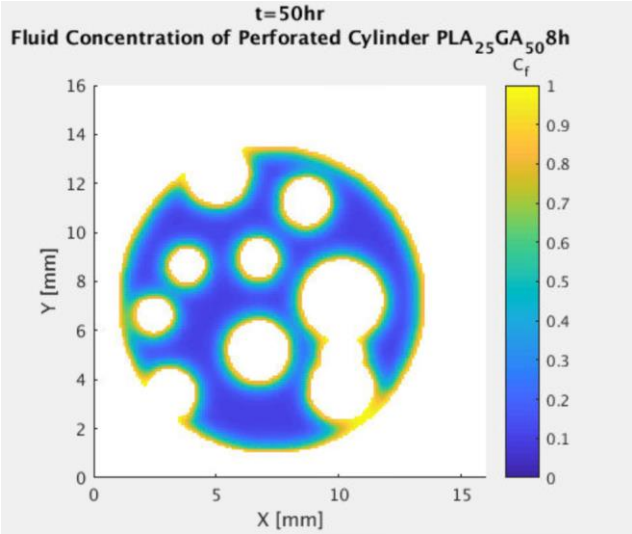

Figure 3.50: Cross section of perforated cylinder fluid concentration distribution at 50hr

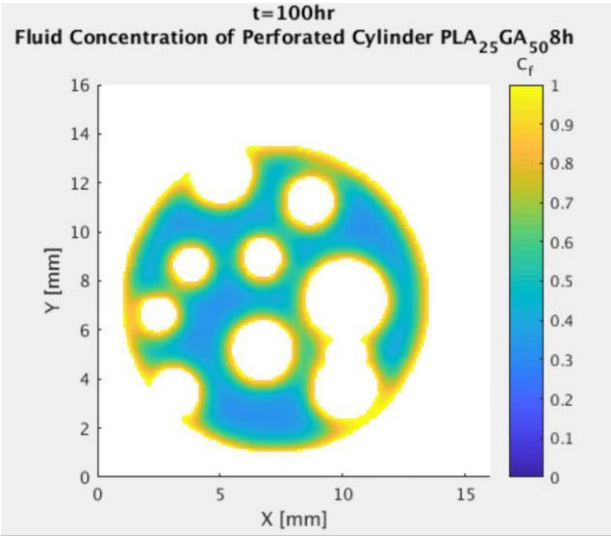

Figure 3.51: Cross section of perforated cylinder fluid concentration distribution at 100hr

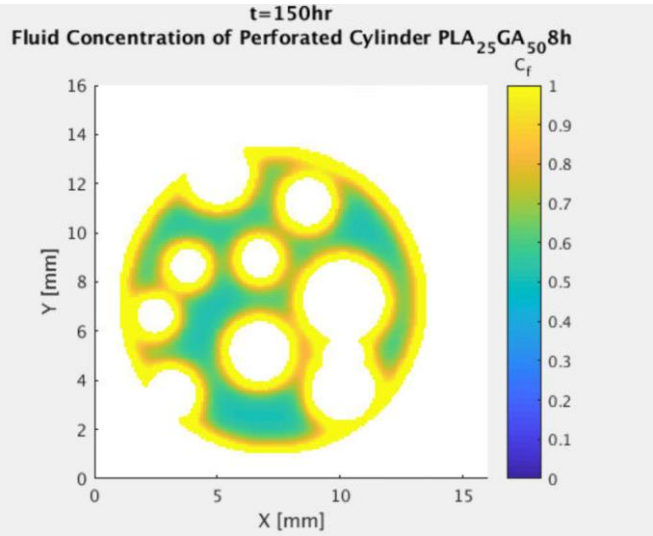

Figure 3.52: Cross section of perforated cylinder fluid concentration distribution at 150hr

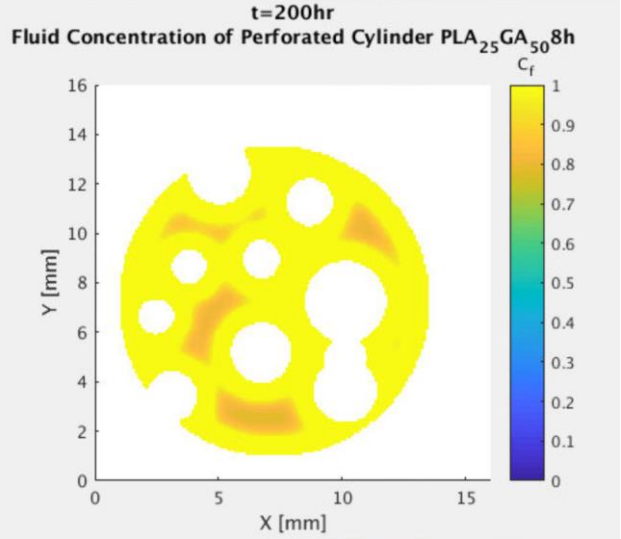

Figure 3.53: Cross section of perforated cylinder fluid concentration distribution at 50hr

Indented Cube

The indented cube model was created to demonstrate how the simulation can capture depressions and the resulting degradation and erosion behavior within the body. An isometric view of the indented cube is seen in Figure 3.54.

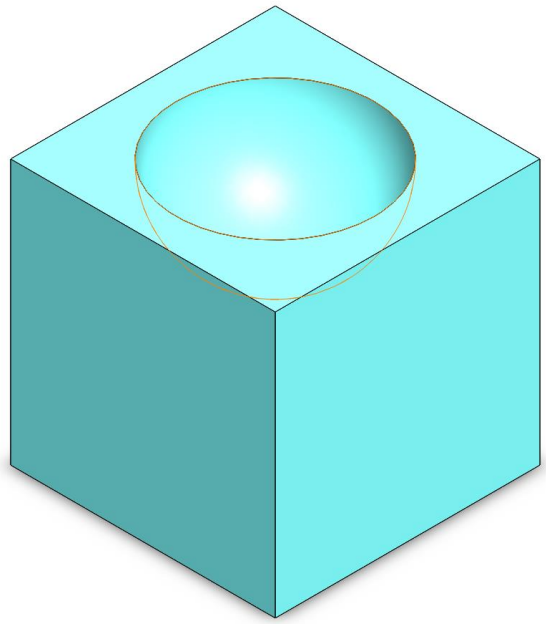

Figure 3.54: Isometric view of indented cylinder SolidWorks file

To ensure a stable computation, the condition presented in Equation (9) is met for all simulations of the indented cube. A convergence study was also performed. The results of this study are seen in Figure 3.55 and Table 3.6. A uniform dimensional step size of 100μm and time step of 15 minutes, or 0.25 hours, was selected for this simulation. The difference between a dimensional step size of 50μm and the one selected is 1.3% for average molecular weight after 24 hours. The larger step size was chosen because 50μm presents

a significantly larger computational cost because it contains 677% more nodes. The discretized body is seen in Figure 3.56.

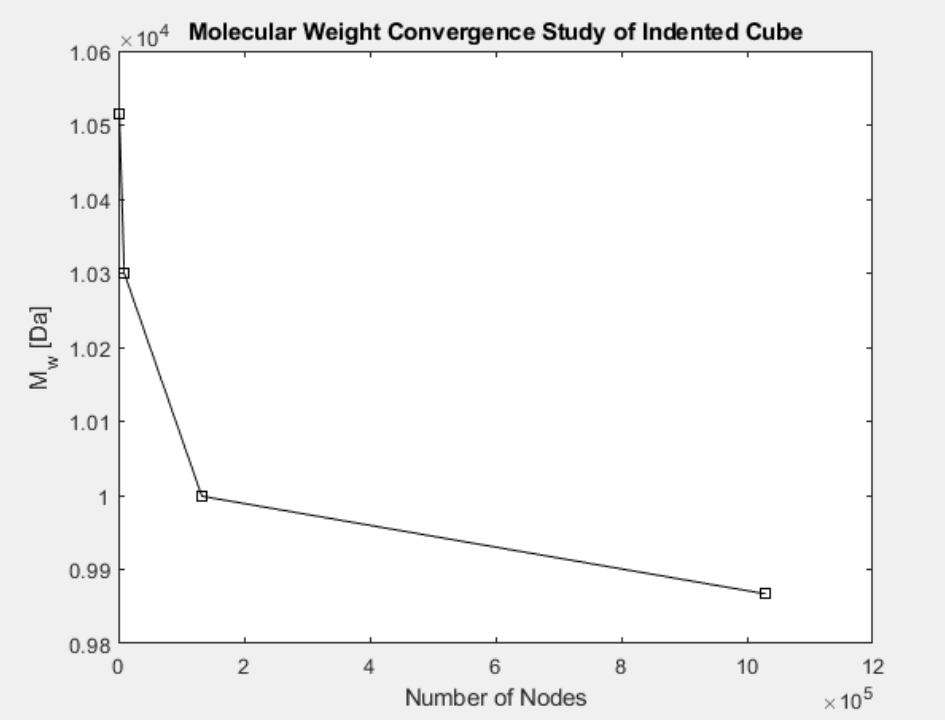

Figure 3.55: Convergence plot of indented cube

Table 3.6: Number of nodes and the respective average molecular weight of indented cube

Number of Nodes	$\boldsymbol{M_{w,avg}\ \Delta t = 0.25hr}$
1331	10516
9261	10300
132651	9999
1030301	9867

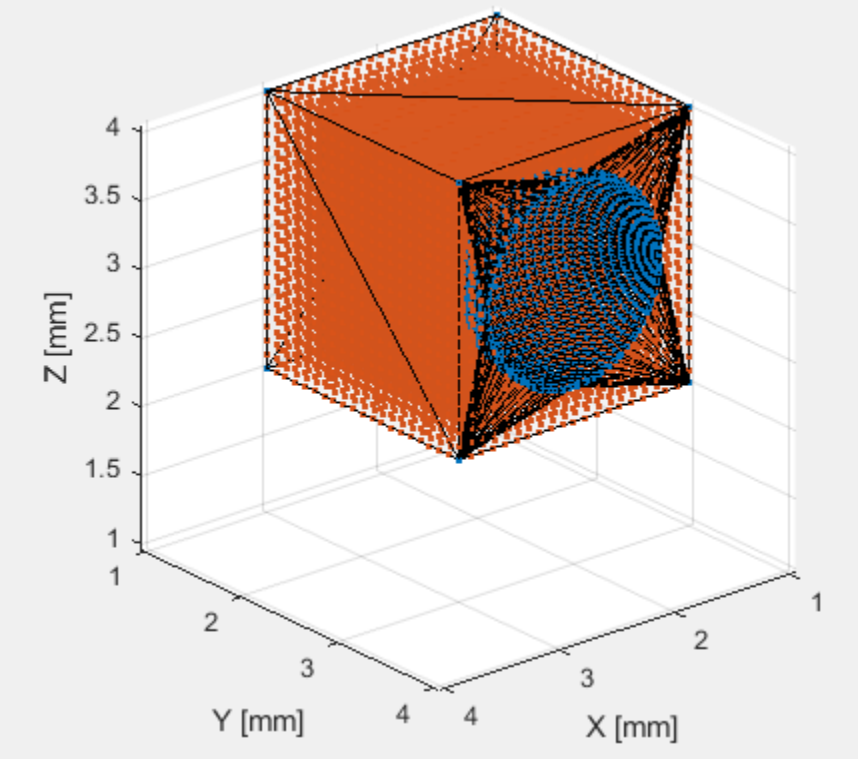

Figure 3.56: Discretized indented cube

The molecular weight loss of this body over 288 hours, or 12 days, is seen in Figure 3.57. As opposed to the perforated cylinder, the curvature of the average molecular weight is initially misleading. As expected, because this is a relatively large body with comparatively slow erosion coefficients, the body initially undergoes primarily surface erosion. The plot then, at first, indicates that the indented cube begins to undergo bulk erosion around 150 hours, or approximately 6.25 days. This is only partly true. As seen in Figures 3.58-61, the regions nearest the indent begin to undergo bulk erosion much sooner than the rest of the body, which quickly leads to that portion of the cube eroding away. The remainder of the body follows sometime after.

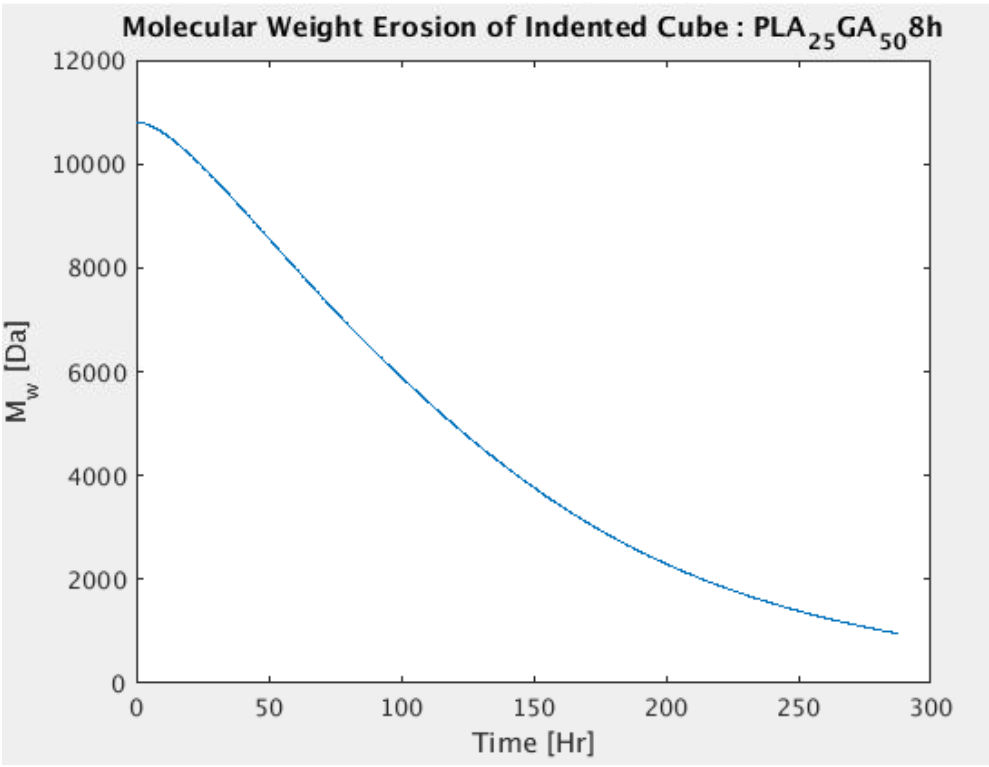

Figure 3.57: Molecular weight erosion of indented cube

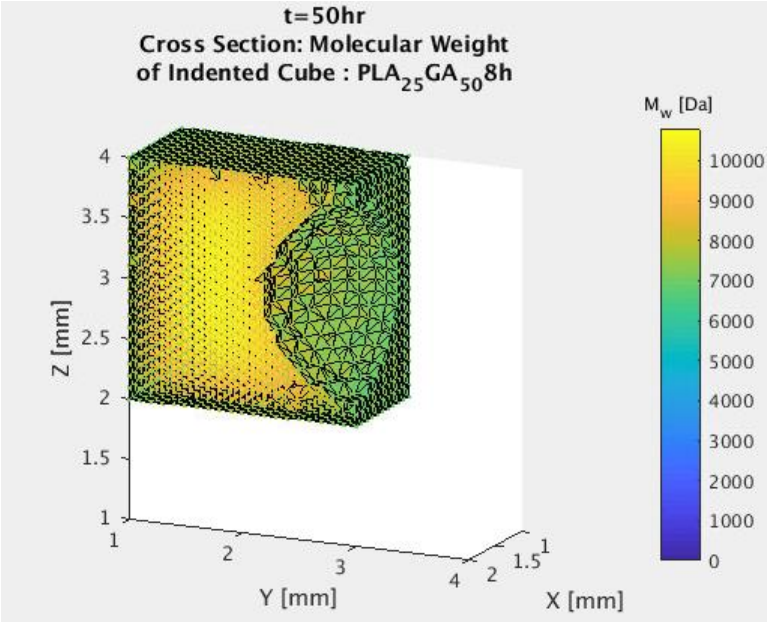

Figure 3.58: Cross section of indented cube molecular weight distribution at 50hr. N > 0.25 N_0

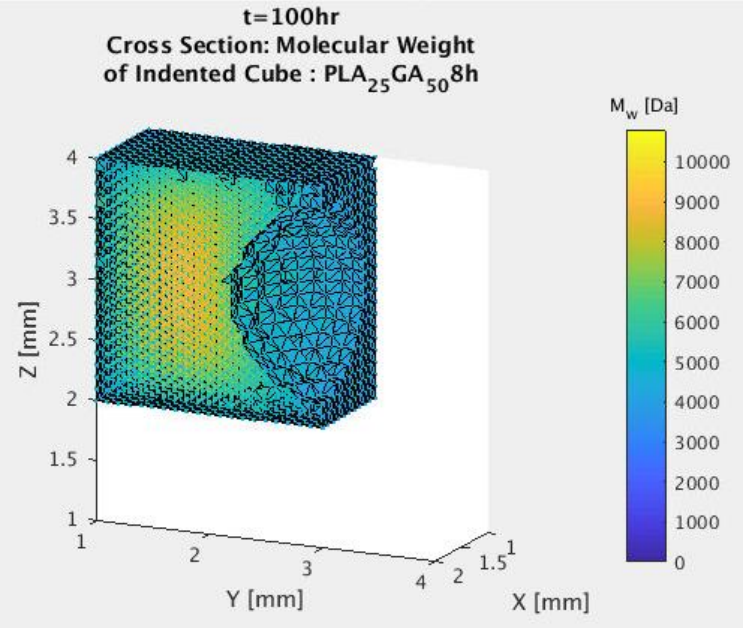

Figure 3.59: Cross section of indented cube molecular weight distribution at 100hr. N > 0.25 N_0

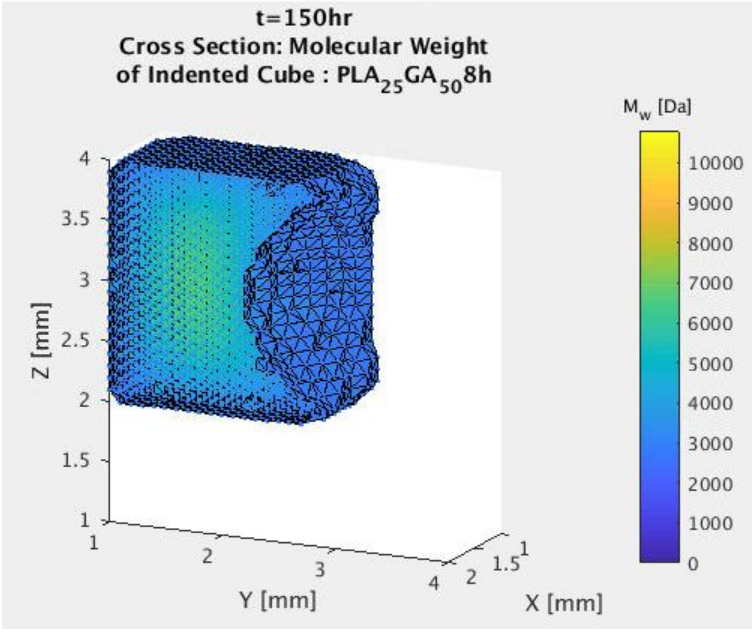

Figure 3.60: Cross section of indented cube molecular weight distribution at 150hr. N > 0.25 N_0

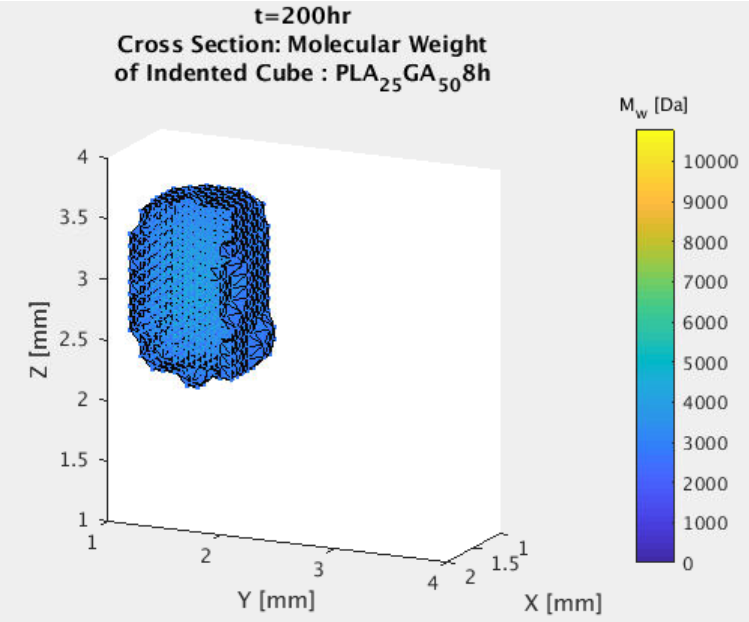

Figure 3.61: Cross section of indented cube molecular weight distribution at 200hr. N > 0.25 N_0

Figures 3.62-65 show the cross section of the body and the fluid concentration distribution throughout it. As predicted from the previous discussion over erosion and molecular weight loss of the indented cube, regions nearest to the depression saturate at a much earlier time than the rest of the body. This logically follows because of the large surface area for fluid diffusion directly due to the ident.

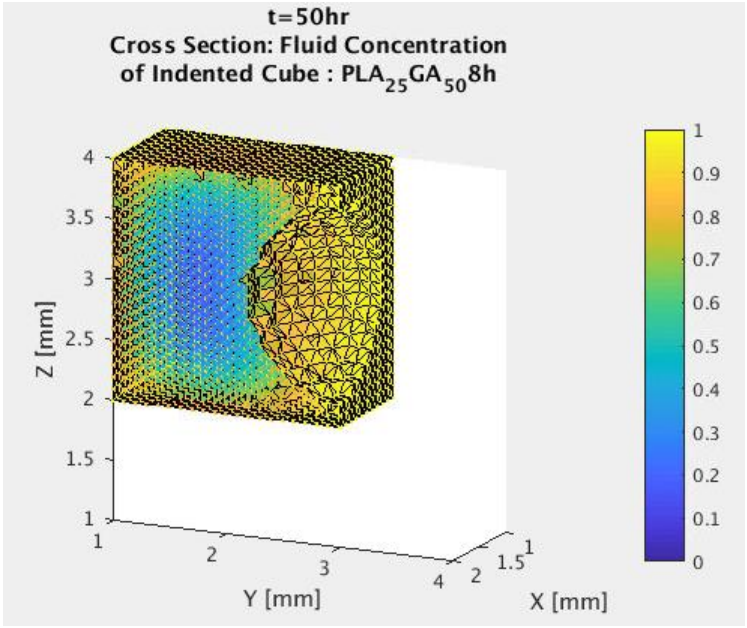

Figure 3.62: Cross section of indented cube fluid concentration distribution at 50hr

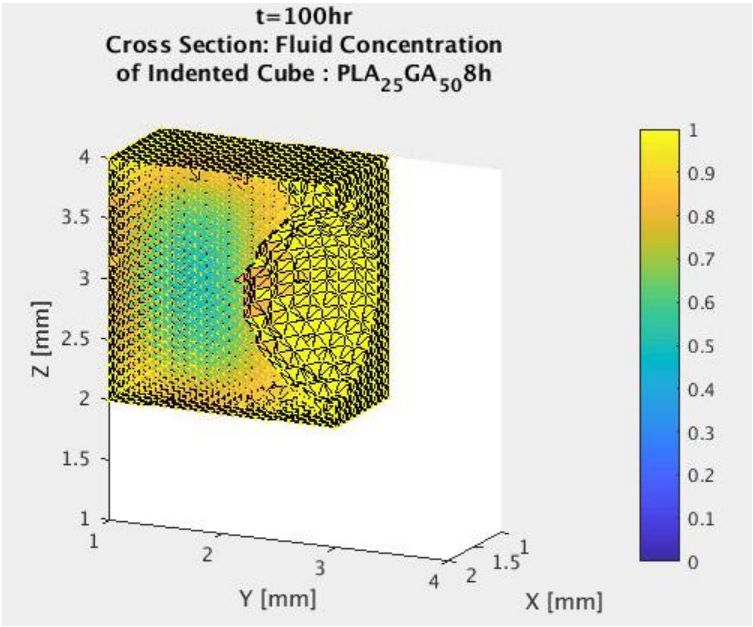

Figure 3.63: Cross section of indented cube fluid concentration distribution at 100hr

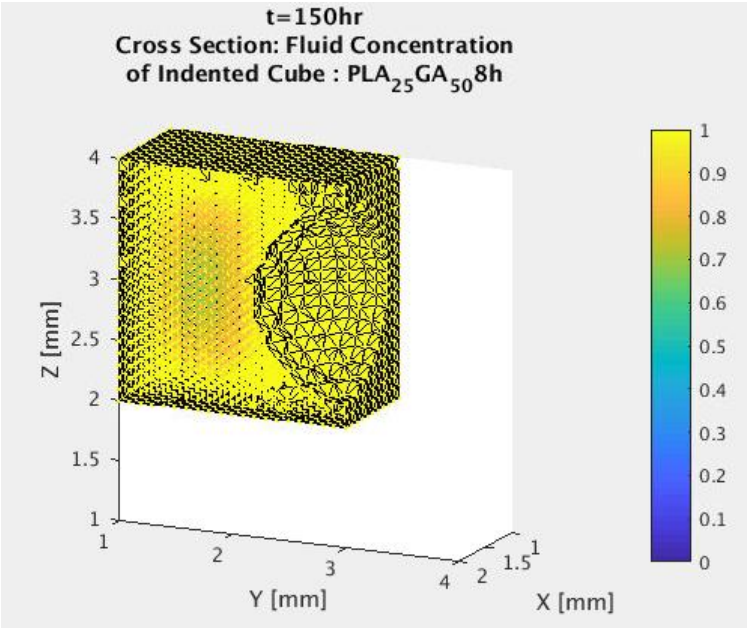

Figure 3.64: Cross section of indented cube fluid concentration distribution at 150hr

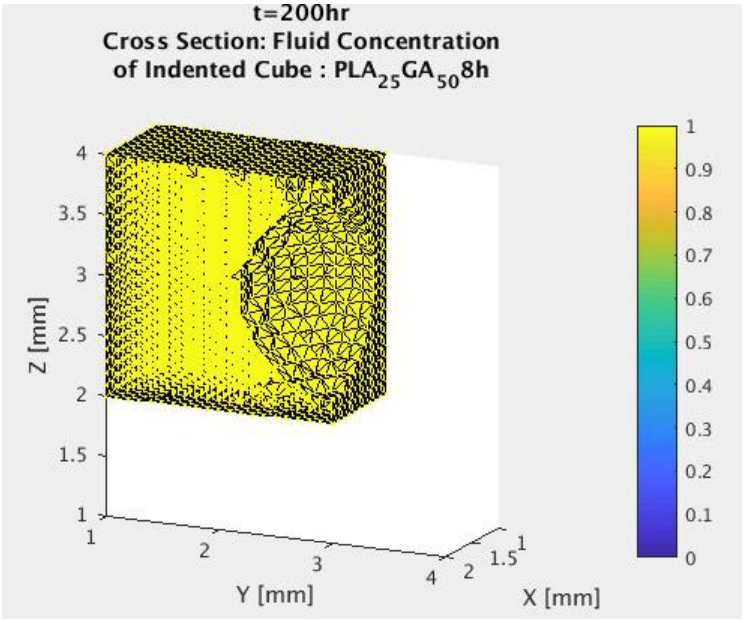

Figure 3.65: Cross section of indented cube fluid concentration distribution at 200hr

CHAPTER IV

SUMMARY

4.1. Discussion of Study

From the current study, the constitutive equations were presented to describe the behavior of polymer degradation and erosion. The model was used to capture the degradation in a biodegradable polymer, specifically Poly(lactic-co-glycolic acid), and provide evidence of its proof of concept. Additionally, the simulation enables the ability to control diffusion of monomers until a threshold value is reached within the polymer. The capability to predict shape change of polymeric bodies intended for implantation can be controlled by a threshold of fluid concentration, monomer concentration, molecular weight, or any combination of the three. In this study the shape change was predicted using only localized molecular weight. Factors due to swelling induced strain were ignored for simplification of the analysis and development of the numerical algorithm. Furthermore, the effects of mechanical stresses on the degradation behavior were not included within the model; however, the created scripts are set up in such a way that nodes and faces can be output and saved to a file that is compatible with an FEA program such as ABAQUS.

The constitutive equations, and subsequently created models, were used to simulate the degradation and erosion behaviors of fluid concentration, molecular weight loss, and prediction of monomer concentration for both $PLA_{25}GA_{50}$8h and $PLA_{25}GA_{50}$14h. From these studies and simulations, it was observed that the monomers of similar composition but differing initial molecular weights exhibited similar

mechanisms of degradation and erosion, only differing by the rate at which fluid diffuses into the cylindrical bodies. This in turn changed the time scale of molecular weight loss and monomer creation.

The values for the process of degradation and erosion found from tuning the model to simulate experimental data was used to predict the degradation and erosion behavior of a realistic cardiovascular stent with a geometry similar to those currently used in industry. These calibrated values were also used to present the model's ability to show the degradation and erosion of other complex geometries and the succeeding shape change. Simulations were able to demonstrate both the behaviors of bulk and surface erosion; therefore, the requirement of a defined critical length for the change between the two mechanisms is not necessarily required for polymeric body analysis.

It is important to note that all prior simulations were run with the assumption that the bodies existed within an environment that was significantly larger than the polymer itself such that monomer concentration outside of the body was assumed to be 0. However, this can be easily changed so an analysis of the monomer concentration within an enclosed environment can be studied. For example, the discretized body a small cube and the monomer diffusion outside of the body can be seen in Figures 4.1 and 4.2 respectively.

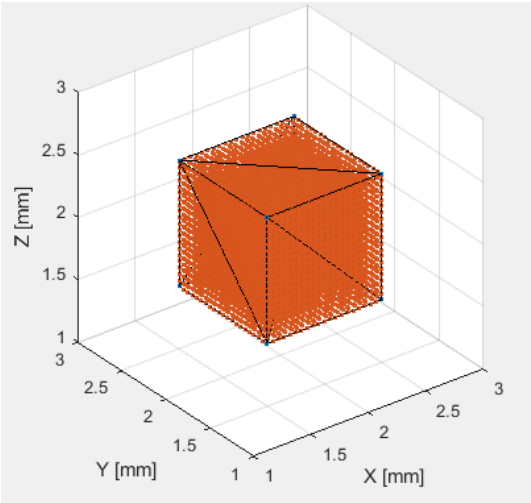

Figure 4.1: Discretized small cube

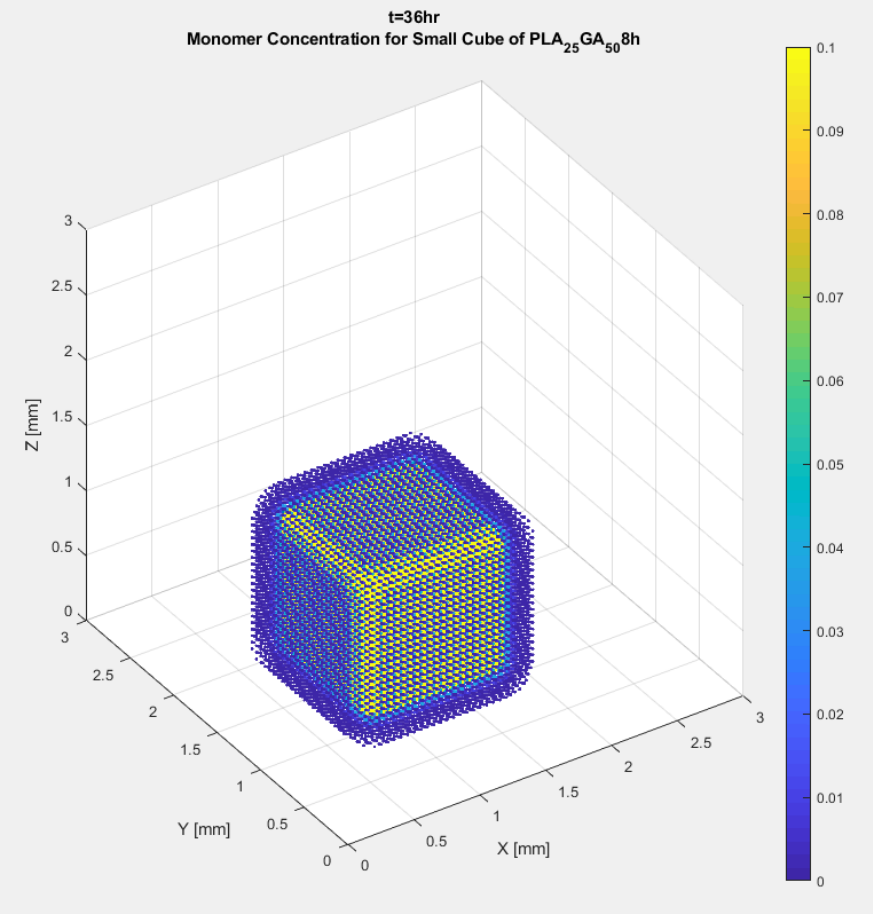

Figure 4.2: Monomer concentration surrounding small cube in enclosed environment

4.2 Future Work

As mentioned in the prior section, factors due to swelling and the resulting induced strain were not incorporated within the model for the purpose of simplification. While this effect may have a small impact upon the rate of diffusion of fluid into and monomers out of the body, the threshold for monomer diffusion may be altered. Additionally, the subsequent shape change due erosion may be impacted in a non-trivial way. Because of this, a long-term study of the effects of swelling are required to further improve the model.

The incorporation of external stresses, such arterial pressure or flexion due to movement, are needed to further mimic a more realistic environment. With the relatively low Young's Moduli of PLGA, external stresses will cause a change in shape of the polymeric body. This will inevitably change the amount of exposed surface area and possibly the boundary conditions. By changing these factors, the location of diffusion and speed at which regions of the polymeric implant become saturated are affected. On the notion of mimicking a realistic environment where these implants will be used, temperature effects will need to be included as these are likely to change diffusion coefficients.

During this study, a framework for predicting the change in local Young's Moduli due to degradation and erosion was created. The framework allowed for the outputs of molecular weight, fluid concentration, and monomer concentration to be loaded and analyzed to output a predicted value for the local Young's Modulus; however, long-term understanding and data of how these properties change is required for this framework to more accurately reflect this behavior. Additionally, the current model does not account for

an initially non-homogenous body; however, with the current set up, it would be possible to modify it to incorporate this feature. Local data would be required and a new material property assignment system would need to be built. While it is currently possible to manually input initial material properties at every node, this can become immensely time consuming and is prone to procedural error. Prospective outlines for an automated system consist of creating a fixed reference point and assigning material values based upon nodal distance from the reference as well as distance relative to surrounding nodes.

Lastly, the basis for the ability to input multiple complex bodies has been planned and partially included. This basis needs expansion to allow for multiple material types and non-degradable bodies, such as bone. The benefit of this feature cannot be understated. If correctly included, it will allow for the inclusion of extremely complex boundary conditions. For example, a polymeric implant bridging between two different organs with unique material properties.

REFERENCES

[1] E. Demarco, J. White, and M. Berry. (2016). *Medical Technology* [Online]. Available: http://www.healthcarebusinesstech.com/medical-technology/.

[2] (2018). *Implants and Prosthetics* [Online]. Available: https://www.fda.gov/medicaldevices/productsandmedicalprocedures/implantsandprosthetics.

[3] F. Witte, "The history of biodegradable magnesium implants: a review," *Acta Biomaterialia*, vol. 6, no. 5, pp. 1680-1692, 2010.

[4] W. Greatbatch and C. F. Holmes, "History of implantable devices," *IEEE Engineering in Medicine and Biology Magazine*, vol. 10, no. 3, pp. 38-41, 1991.

[5] J. M. Ortman, V. A. Velkoff, and H. Hogan, *An aging nation: the older population in the United States*. United States Census Bureau, Economics and Statistics Administration, US …, 2014.

[6] (2018). *Over 1.8 Million Stents Implanted per Year in the U.S.* [Online]. Available: https://idataresearch.com/over-1-8-million-stents-implanted-per-year-in-the-u-s/.

[7] (2011). *The 11 Most Implanted Medical Devices in America* [Online]. Available: https://www.businessinsider.com/the-11-most-implanted-medical-devices-in-america-2011-7.

[8] V. Sansone, D. Pagani, and M. Melato, "The effects on bone cells of metal ions released from orthopaedic implants. A review," *Clinical cases in mineral and bone metabolism*, vol. 10, no. 1, p. 34, 2013.

[9] J. C. Middleton and A. J. Tipton, "Synthetic biodegradable polymers as orthopedic devices," *Biomaterials*, vol. 21, no. 23, pp. 2335-2346, 2000.

[10] L. E. Freed *et al.*, "Biodegradable polymer scaffolds for tissue engineering," *Bio/technology*, vol. 12, no. 7, p. 689, 1994.

[11] A. Weiler, R. F. Hoffmann, A. C. Stähelin, H.-J. Helling, and N. P. Südkamp, "Biodegradable implants in sports medicine: the biological base," *Arthroscopy: The Journal of Arthroscopic & Related Surgery*, vol. 16, no. 3, pp. 305-321, 2000.

[12] M. Ebrahimian-Hosseinabadi, F. Ashrafizadeh, M. Etemadifar, and S. S. Venkatraman, "Evaluating and modeling the mechanical properties of the prepared PLGA/nano-BCP composite scaffolds for bone tissue engineering," *Journal of Materials Science & Technology,* vol. 27, no. 12, pp. 1105-1112, 2011.

[13] M. Ebrahimian-Hosseinabadi, F. Ashrafizadeh, M. Etemadifar, and S. S. Venkatraman, "Preparation and mechanical behavior of PLGA/nano-BCP composite scaffolds during in-vitro degradation for bone tissue engineering," *Polymer Degradation and Stability,* vol. 96, no. 10, pp. 1940-1946, 2011.

[14] S. J. Kim, D. H. Jang, W. H. Park, and B.-M. Min, "Fabrication and characterization of 3-dimensional PLGA nanofiber/microfiber composite scaffolds," *Polymer,* vol. 51, no. 6, pp. 1320-1327, 2010.

[15] K. Wei *et al.*, "Emulsion Electrospinning of a Collagen-Like Protein/PLGA Fibrous Scaffold: Empirical Modeling and Preliminary Release Assessment of Encapsulated Protein," *Macromolecular Bioscience,* vol. 11, no. 11, pp. 1526-1536, 2011.

[16] J. A. Matthews, G. E. Wnek, D. G. Simpson, and G. L. Bowlin, "Electrospinning of collagen nanofibers," *Biomacromolecules,* vol. 3, no. 2, pp. 232-238, 2002.

[17] Z. Ge, X. Tian, B. C. Heng, V. Fan, J. F. Yeo, and T. Cao, "Histological evaluation of osteogenesis of 3D-printed poly-lactic-co-glycolic acid (PLGA) scaffolds in a rabbit model," *Biomedical Materials,* vol. 4, no. 2, p. 021001, 2009.

[18] E. Saito, H. Kang, J. M. Taboas, A. Diggs, C. L. Flanagan, and S. J. Hollister, "Experimental and computational characterization of designed and fabricated 50: 50 PLGA porous scaffolds for human trabecular bone applications," *Journal of Materials Science: Materials in Medicine,* vol. 21, no. 8, pp. 2371-2383, 2010.

[19] C. M. Agrawal and R. B. Ray, "Biodegradable polymeric scaffolds for musculoskeletal tissue engineering," *Journal of Biomedical Materials Research: An Official Journal of The Society for Biomaterials, The Japanese Society for Biomaterials, and The Australian Society for Biomaterials and the Korean Society for Biomaterials,* vol. 55, no. 2, pp. 141-150, 2001.

[20] X. Liu and P. X. Ma, "Polymeric scaffolds for bone tissue engineering," *Annals of Biomedical Engineering,* vol. 32, no. 3, pp. 477-486, 2004.

[21] J. K. Perron, H. E. Naguib, J. Daka, A. Chawla, and R. Wilkins, "A study on the effect of degradation media on the physical and mechanical properties of porous

PLGA 85/15 scaffolds," *Journal of Biomedical Materials Research Part B: Applied Biomaterials: An Official Journal of The Society for Biomaterials, The Japanese Society for Biomaterials, and The Australian Society for Biomaterials and the Korean Society for Biomaterials,* vol. 91, no. 2, pp. 876-886, 2009.

[22] F. Yang, W. Cui, Z. Xiong, L. Liu, J. Bei, and S. Wang, "Poly (l, l-lactide-co-glycolide)/tricalcium phosphate composite scaffold and its various changes during degradation in vitro," *Polymer Degradation and Stability,* vol. 91, no. 12, pp. 3065-3073, 2006.

[23] M. Houchin and E. Topp, "Physical properties of PLGA films during polymer degradation," *Journal of applied polymer science,* vol. 114, no. 5, pp. 2848-2854, 2009.

[24] P. Gentile, V. Chiono, I. Carmagnola, and P. Hatton, "An overview of poly (lactic-co-glycolic) acid (PLGA)-based biomaterials for bone tissue engineering," *International Journal of Molecular Sciences,* vol. 15, no. 3, pp. 3640-3659, 2014.

[25] A. S. Dunn, P. G. Campbell, and K. G. Marra, "The influence of polymer blend composition on the degradation of polymer/hydroxyapatite biomaterials," *Journal of Materials Science: Materials in Medicine,* vol. 12, no. 8, pp. 673-677, 2001.

[26] F. von Burkersroda, L. Schedl, and A. Göpferich, "Why degradable polymers undergo surface erosion or bulk erosion," *Biomaterials,* vol. 23, no. 21, pp. 4221-4231, 2002.

[27] H.-Y. Cheung, K.-T. Lau, Y.-F. Pow, Y.-Q. Zhao, and D. Hui, "Biodegradation of a silkworm silk/PLA composite," *Composites Part B: Engineering,* vol. 41, no. 3, pp. 223-228, 2010.

[28] Y. Chen, S. Zhou, and Q. Li, "Mathematical modeling of degradation for bulk-erosive polymers: applications in tissue engineering scaffolds and drug delivery systems," *Acta Biomaterialia,* vol. 7, no. 3, pp. 1140-1149, 2011.

[29] A. Göpferich, "Mechanisms of polymer degradation and erosion," *Biomaterials,* vol. 17, no. 2, pp. 103-114, 1996.

[30] T. Casalini, F. Rossi, S. Lazzari, G. Perale, and M. Masi, "Mathematical modeling of PLGA microparticles: from polymer degradation to drug release," *Molecular Pharmaceutics,* vol. 11, no. 11, pp. 4036-4048, 2014.

[31] B. Hannan. (2016). *Mesh cross-sections* 1.0.0.0, MathWorks. [Online]. Available.

[32] J. Naghipoor and T. Rabczuk, "A mechanistic model for drug release from PLGA-based drug eluting stent: A computational study," *Computers in Biology and Medicine,* vol. 90, pp. 15-22, 2017.

[33] J. K. Murphy, "Finite Element Analyses of Cyclically Loaded Linear Viscoelastic Biodegradable Stent," Master of Science, Mechanical Engineering, Texas A&M University, 2014.

APPENDIX A

MATLAB SCRIPT: THREEDIMENSIONALV6.M

```
%Three Dimensional

%Mitchell F. Shockley
clear;
U=load('burkersroda_cylinder_01mm.txt','U','-ascii');

%%  MATL/PROCESS PROPERTIES
Df=.48*10^-6*3600*1000^2; %fluid diffusivity [um2/hr]
Kf=.5*10^-6*3600; %reaction Rate [1/hr]
tau_s=100; %characteristic time [hr]
N0=10800; %molecular weight [Da]
Dm=.001*10^-5*3600*1000^2; %diffusivity constant of monomers [um2/hr]
diffvar=0.02; %Cm threshold for diffusion
erodvar=.45;  %N/N0 threshold for erosion
erodvar2=1;

del_t=1; %[hr]
del_x=100; %[um]
del_y=del_x; %[um]
del_z=del_x; %[um]

%checking for stable computational analysis
% if del_t/(del_x^2) > 0.5
%     error('ERROR: DEL_T/(DEL_X^2) > 0.5')
% end

time=24*16; %[hr]
x=15*1000; %[um]
y=15*1000; %[um]
z=3*1000; %[um]
ts=time/del_t; %steps for [time]
xs=round(x/del_x,4); %steps for [x]
ys=round(y/del_y,4); %steps for [y]
zs=round(z/del_z,4); %steps for [z]

%%  Unpack the points from discretization
initials=unpacker(U,xs,ys,zs);

%%  Define Large Matrices/Initials
svar=round((xs+1)*(ys+1)*(zs+1));
Cf=zeros(svar,ts);
Cm=zeros(svar,ts);
N=zeros(svar,ts);
d=zeros(svar,ts);
N(:,1)=(1-initials(:,1))*N0; %molecular weight
Cf(:,1)=initials(:,1);
Cm(:,1)=initials(:,2);
```

```
onecounterf=1;
zerocounterf=1;
oneboundf=[0];
zeroboundf=[0];
onecounterm=1;
zerocounterm=1;
oneboundm=[0];
zeroboundm=[0];
 for p=1:svar
    if Cf(p,1)>0.9999
        oneboundf(onecounterf,1)=p;
        onecounterf=onecounterf+1;
    end
    if Cf(p,1)<0
        zeroboundf(zerocounterf,1)=p;
        zerocounterf=zerocounterf+1;
        Cf(p,1)=0;
    end
    if initials(p,3)==1
        N(p,:)=0;
    end
    if Cm(p,1)>0.9999
        oneboundm(onecounterm,1)=p;
        onecounterm=onecounterm+1;
    end
    if Cm(p,1)<0
        zeroboundm(zerocounterm,1)=p;
        zerocounterm=zerocounterm+1;
        Cm(p,1)=0;
    end
 end
```

```
%%  EQUATION 5
A5(1:svar)=(Df*del_t)/(del_x)^2;
B5(1:svar)=(-2*Df*del_t)/(del_x)^2;
C5(1:svar)=(Df*del_t)/(del_x)^2;
D5(1:svar)=(Df*del_t)/(del_y)^2;
E5(1:svar)=(-2*Df*del_t)/(del_y)^2;
F5(1:svar)=(Df*del_t)/(del_y)^2;
G5(1:svar)=(-Kf*del_t+1);
H5(1:svar)=(Df*del_t)/(del_z)^2;
I5(1:svar)=(Df*del_t)/(del_z)^2;
J5(1:svar)=(-2*Df*del_t)/(del_z)^2;
phi5=[A5' B5' C5' D5' E5' F5' G5' H5' I5' J5'];
diag5=  [1,0,-1,xs+1,0,-(xs+1),0,(xs+1)*(ys+1),-(xs+1)*(ys+1),0];
A=spdiags(phi5,diag5,svar,svar);
```

```
for m=1:ts-1

    Cf(:,m+1)=A*Cf(:,m);
    if length(zeroboundf)==1
    else
    Cf(zeroboundf(:,1),m:ts)=0;
    end
    Cf(oneboundf(:,1),m:ts)=1;
end

fprintf('Cf Calc\n')

%%  EQUATION 6
for m=1:ts-1
            N(:,m+1)=(1-(Cf(:,m)*del_t)/(tau_s)).*N(:,m);
end


fprintf('N Calc\n')

%%  EQUATION 7
A7(1:svar)=(Dm*del_t)/(del_x)^2;
B7(1:svar)=(-2*Dm*del_t)/(del_x)^2;
C7(1:svar)=(Dm*del_t)/(del_x)^2;
D7(1:svar)=(Dm*del_t)/(del_y)^2;
E7(1:svar)=(-2*Dm*del_t)/(del_y)^2;
F7(1:svar)=(Dm*del_t)/(del_y)^2;
G7(1:svar)=(1);
H7(1:svar)=(Dm*del_t)/(del_z)^2;
I7(1:svar)=(Dm*del_t)/(del_z)^2;
J7(1:svar)=(-2*Dm*del_t)/(del_z)^2;
phi7=[A7' B7' C7' D7' E7' F7' G7' H7' I7' J7'];
diag7=  [1,0,-1,xs+1,0,-(xs+1),0,(xs+1)*(ys+1),-(xs+1)*(ys+1),0];
B=spdiags(phi7,diag7,svar,svar);



 diflist=zeros(svar,1);
 erodlist=zeros(svar,1);
 substep=floor(0.02*(ts-1));
 laststep=0;
 Cm(:,1)=(1-N(:,1)/N0).*(1-initials(:,1));
for m=1:ts-1
    if length(zeroboundm)==1
    else
    Cm(zeroboundm(:,1),m:ts)=0;
    end
    diflegm=nnz(diflist);
    erodlegm=nnz(erodlist);
    %check status of nodes
```

```
    for i=1:svar
        if Cm(i,m) >= diffvar && diflist(i,1)~=1
            diflist(i,1)=1;
        end
        if N(i,m)/N0 <= erodvar && erodlist(i,1)~=1 && diflist(i,1)==1
&& Cm(i,m) <=erodvar2
            erodlist(i,1)=1;
            oneboundf(length(oneboundf)+1,1)=i;
        end
    end

    Cm(:,m+1)=B*Cm(:,m)+(-N(:,m+1)+N(:,m))/N0;

    for i=1:svar
        if diflist(i,1)~=1 && initials(i,1)~=1
            Cm(i,m+1)=(1-N(i,m+1)/N0);
        end
    end

    if length(zeroboundm)==1
    else
    Cm(zeroboundm(:,1),m:ts)=0;
    end
    Cf(oneboundf(:,1),m:ts)=1;
    %end status check

    %begin recalc

    if erodlegm < nnz(erodlist)
        if ((ts-1)-m)>substep
            for n=m:m+substep
                Cf(:,n+1)=A*Cf(:,n);
                Cf(oneboundf(:,1),m:ts)=1;
                N(:,n+1)=(1-(Cf(:,n)*del_t)/(tau_s)).*N(:,n);
            end
            laststep=m+substep;
        else
            for n=m:ts-1
                Cf(:,n+1)=A*Cf(:,n);
                Cf(oneboundf(:,1),m:ts)=1;
                N(:,n+1)=(1-(Cf(:,n)*del_t)/(tau_s)).*N(:,n);
            end
        end
    end

    if laststep>0
        if m==laststep
            if (ts-1)-m > substep
                for n=m:m+substep
                    Cf(:,n+1)=A*Cf(:,n);
                    Cf(oneboundf(:,1),m:ts)=1;
                    N(:,n+1)=(1-(Cf(:,n)*del_t)/(tau_s)).*N(:,n);
```

```
                end
                laststep=m+substep;
            else
                for n=m:ts-1
                    Cf(:,n+1)=A*Cf(:,n);
                    Cf(oneboundf(:,1),m:ts)=1;
                    N(:,n+1)=(1-(Cf(:,n)*del_t)/(tau_s)).*N(:,n);
                end
            end
        end
    end


end
fprintf('Cm Calc\n')
maxCf=max(max(Cf))
maxCm=max(max(Cm))
minN=min(min(N))
beep
```

APPENDIX B

MATLAB SCRIPT: THREEDIMENSIONALPLOTTOOL.M

```
tplot=50; %[hr]
tplot=round(tplot/del_t,3);
Item=N(:,tplot);
Nhold=N;
figure
x=15; %[mm]
y=15; %[mm]
z=3; %[mm]
%DO NOT CHANGE THINGS PAST HERE
if Item==Cf(:,tplot)
    tit=1;
elseif Item==Cm(:,tplot)
    tit=2;
elseif Item==N(:,tplot)
    tit=3;
elseif Item==d(:,tplot)
    tit=4;
end

P=U;
leg=length(P);

if length(P)~=length(Item)
    error('rerun solver')
end
Phold=nan(length(P),1);
for q=1:leg
    if isnan(P(q,1))
        Item(q)=NaN;
        Phold(q,1)=q;
    end
%     if tit==1
%         if Item(q) > 0.99 && ~isnan(Item(q))
%             Item(q)=NaN;
%             Phold(q,1)=q;
%         end
%     end
    if tit==3
        if Nhold(q,tplot)/N0 < 0.25 && ~isnan(Item(q))
            Item(q)=NaN;
            Phold(q,1)=q;
        end
    end
end


Phold(isnan(Phold))=[];
```

```
P(Phold,:)=[];
Item(Phold,:)=[]; %something strange about colon operators.....
k=boundary(P,1);
col=zeros(length(P),3);
patch('Vertices',P,'Faces',k,'FaceVertexCData',Item(:),'FaceColor','int
erp')
axis image
shading flat
hold on
scatter3(P(:,1),P(:,2),P(:,3),25,Item(:,1),'.')
h=colorbar;
view(90,0)
if tit==1
    title({['t=',num2str(del_t*tplot),'hr'];'Cross Section: Fluid
Concentration of PLA_2_5GA_5_08h';' '})
elseif tit==2
    title({['t=',num2str(del_t*tplot),'hr'];'Cross Section: Monomer
Concentration of PLA_2_5GA_5_08h';' '})
elseif tit==3
    title({['t=',num2str(del_t*tplot),'hr'];'Cross Section: Molecular
Weight of PLA_2_5GA_5_08h';' '})
elseif tit==4
    title({['t=',num2str(del_t*tplot),'hr'];'Degree of
Monomerization';' '})
end
xlabel('X [mm]')
ylabel('Y [mm]')
zlabel('Z [mm]')
ylim([0,y+1]);
xlim([0,7.25]);
zlim([0,z+1]);
if tit==1 || tit==2 || tit==4
    caxis([0 1])
else
    caxis([0 N0])
end
if tit==3
title(h,'M_w [Da]')
else
    title(h,' ')
end
```

APPENDIX C

MATLAB SCRIPT: MODELDISCRETIZER.M

```
%Model Discretizer
%Take 3D models and make into array of points to analyze
clc; clear all; close all;


x=5; %[mm]
y=5; %[mm]
z=5; %[mm]
del_x=100/1000; %[mm]
del_y=del_x; %[mm]
del_z=del_x; %[mm]
xs=round(x/del_x,4); %steps for [x]
ys=round(y/del_y,4); %steps for [y]
zs=round(z/del_z,4); %steps for [z]
svar=round((xs+1)*(ys+1)*(zs+1));

%Extract Data
[F,V,N]=stlread('3d body-solidworks/cube_indent.stl');
P=F.Points;
C=F.ConnectivityList;

%Scale
% maxx=max(P(:,1));
% maxy=max(P(:,2));
% maxz=max(P(:,3));
% maxman=max([maxx,maxy,maxz]);
% scale=maxman/max([x,y,z]);
% P=P/scale;
P(:,3)=P(:,3)*1.01;

%Shift Into Realm
minx=min(P(:,1));
miny=min(P(:,2));
minz=min(P(:,3));
if minx <= 0
    P(:,1)=P(:,1)+abs(minx);
end
if miny <= 0
    P(:,2)=P(:,2)+abs(miny);
end
if minz <= 0
    P(:,3)=P(:,3)+abs(minz)+(z/2-1);
end
if minx > 0
    P(:,1)=P(:,1)-abs(minx);
end
if miny > 0
    P(:,2)=P(:,2)-abs(miny);
```

```
end
if minz > 0
    P(:,3)=P(:,3)-abs(minz)+(z/2-1);
end
P=P+1;

%Plotter
pmaxx=max(P(:,1));
pmaxy=max(P(:,2));
pmaxz=max(P(:,3));
pminx=min(P(:,1));
pminy=min(P(:,2));
pminz=min(P(:,3));
scatter3(P(:,1),P(:,2),P(:,3),'.')
hold on
trisurf(C,P(:,1),P(:,2),P(:,3),'Facecolor','white','FaceAlpha',0.05)
camlight('headlight');material('dull'); axis('image');
scaler=0.01;
maxdim=max([pmaxy*(1+scaler),pmaxx*(1+scaler),pmaxz*(1+scaler)]);
mindim=min([pminx-maxdim*scaler,pminy-maxdim*scaler,pminz-
maxdim*scaler]);
ylim([mindim,maxdim]);
xlim([mindim,maxdim]);
zlim([mindim,maxdim]);
xlabel('X [mm]')
ylabel('Y [mm]')
zlabel('Z [mm]')
title('Discretized Body of: cube\_indent.stl')
hold on

%Throwing the Discretized Grid Into the Object
for k=1:zs+1
    for j=1:ys+1
        for i=1:xs+1
            X(i+(xs+1)*(j-1)+(ys+1)*(xs+1)*(k-1))=i*del_x+(1-del_x);
            Y(i+(xs+1)*(j-1)+(ys+1)*(xs+1)*(k-1))=j*del_y+(1-del_y);
            Z(i+(xs+1)*(j-1)+(ys+1)*(xs+1)*(k-1))=k*del_z+(1-del_z);
        end
    end
end
U=[X; Y; Z]';

r=1;
for i=1:zs+1
    slicePlane=[0 0 i*del_z+0.0001+(1-del_z),1 0 0,0 1 0];

    if i==round(zs+1,3)
        slicePlane=[0 0 i*del_z-0.0001+(1-del_z),1 0 0,0 1 0];
    end

    polyl=xsecmesh(slicePlane,P,C);
```

```
    if isempty(cellfun(@isempty,polyl)) ~= 1

    polygonCell(r,1:numel(polyl(1,:)))=xsecmesh(slicePlane,P,C);
    r=r+1;
    end
end


in=zeros(svar,1);
on=zeros(svar,1);
[xsize,ysize]=size(polygonCell);
for k=1:zs+1
    holder=[];
    for q=1:xsize
        if round(polygonCell{q,1}(1,3),3) == round((k*del_z+1-del_z),3)
            holder=polygonCell(q,:);
            k=round(round(polygonCell{q,1}(1,3)-0.0001-1,3)/del_z +
1,3);
        end
    end
    clearvars xv yv
        xv=[];
        yv=[];
        if ~isempty(holder)
            for u=1:nnz(~cellfun(@isempty,holder(1,:)))
                legx=length(xv);
                legy=length(yv);
            if u==1
                if ispolycw(holder{1,u}(:,1),holder{1,u}(:,2))

[holder{1,u}(:,1),holder{1,u}(:,2)]=poly2ccw(holder{1,u}(:,1),holder{1,
u}(:,2));

xv(legx+1:legx+length(holder{1,u}(:,1)),1)=holder{1,u}(:,1);
                    xv(legx+length(holder{1,u}(:,1))+1,1)=NaN;

yv(legy+1:legy+length(holder{1,u}(:,2)),1)=holder{1,u}(:,2);
                    yv(legy+length(holder{1,u}(:,2))+1,1)=NaN;
                else

xv(legx+1:legx+length(holder{1,u}(:,1)),1)=holder{1,u}(:,1);
                    xv(legx+length(holder{1,u}(:,1))+1,1)=NaN;

yv(legy+1:legy+length(holder{1,u}(:,2)),1)=holder{1,u}(:,2);
                    yv(legy+length(holder{1,u}(:,2))+1,1)=NaN;
                end
            end
            if u>1
                if ispolycw(holder{1,u}(:,1),holder{1,u}(:,2))

xv(legx+1:legx+length(holder{1,u}(:,1)),1)=holder{1,u}(:,1);
                    xv(legx+length(holder{1,u}(:,1))+1,1)=NaN;
```

```
yv(legy+1:legy+length(holder{1,u}(:,2)),1)=holder{1,u}(:,2);
                    yv(legy+length(holder{1,u}(:,2))+1,1)=NaN;
                else

[holder{1,u}(:,1),holder{1,u}(:,2)]=poly2cw(holder{1,u}(:,1),holder{1,u
}(:,2));

xv(legx+1:legx+length(holder{1,u}(:,1)),1)=holder{1,u}(:,1);
                    xv(legx+length(holder{1,u}(:,1))+1,1)=NaN;

yv(legy+1:legy+length(holder{1,u}(:,2)),1)=holder{1,u}(:,2);
                    yv(legy+length(holder{1,u}(:,2))+1,1)=NaN;
                end

            end
            xv(xv==0)=[];
            yv(yv==0)=[];
            end
            for j=1:ys+1
                for i=1:xs+1
                    [in(i+(xs+1)*(j-1)+(ys+1)*(xs+1)*(k-
1),1),on(i+(xs+1)*(j-1)+(ys+1)*(xs+1)*(k-
1),1)]=inpolygon(U(i+(xs+1)*(j-1)+(ys+1)*(xs+1)*(k-
1),1)',U(i+(xs+1)*(j-1)+(ys+1)*(xs+1)*(k-1),2),xv,yv);
                end
            end
        else
            for j=1:ys+1
                for i=1:xs+1
                    in(i+(xs+1)*(j-1)+(ys+1)*(xs+1)*(k-1),1)=0;
                    on(i+(xs+1)*(j-1)+(ys+1)*(xs+1)*(k-1),1)=0;
                end
            end
        end
end

for i=1:length(in)
    if in(i,1) == 0
        U(i,:)=NaN;
    end
end
W=U;
for i=1:length(on)
    if on(i,1) == 1
        W(i,:)=U(i,:);
    else
        W(i,:)=NaN;
    end
end
scatter3(U(:,1),U(:,2),U(:,3),'.');
hold on
% scatter3(W(:,1),W(:,2),W(:,3),'x','b');
```

APPENDIX D

MATLAB SCRIPT: UNPACKER.M AND SAVER.M

D.1. Unpacker

```
function [points] = unpacker(U,xs,ys,zs)
%unpacker
%unpacking points from discretized model for simple gaussian elim
pointhold=zeros(length(U),3); %Cf, Cm, Body
zstep=round(zs+1,4);
ystep=round(ys+1,4);
xstep=round(xs+1,4);
for k=1:zstep
    for j=1:ystep
        for i=1:xstep
            if isnan(U(i+(xstep)*(j-1)+(ystep)*(xstep)*(k-1),1))
                pointhold(i+(xstep)*(j-1)+(ystep)*(xstep)*(k-1),1)=1;
                pointhold(i+(xstep)*(j-1)+(ystep)*(xstep)*(k-1),2)=-1;
                pointhold(i+(xstep)*(j-1)+(ystep)*(xstep)*(k-1),3)=1;
            end
        end
    end
end
points=pointhold;
end
```

D.2. Saver

```
clc;
name='burkersroda_cylinder_01mm.txt';
save(name,'U','-ascii')
```